UNIVERSITY
OF OSLO

Jie Hou

Experimental Sensor Systems for Assessment of Tissue Viability

Monitoring the effects of ischemia-reperfusion injury

Thesis submitted for the degree of Philosophiae Doctor

Department of Physics
Faculty of Mathematics and Natural Sciences

Department of Clinical and Biomedical Engineering
Oslo University Hospital

2023

Preface

This thesis is submitted in partial fulfillment of the requirements for the degree of *Philosophiae Doctor* at the University of Oslo. The research presented here was conducted at the Oslo University Hospital, under the supervision of Dr. Jan Olav Høgetveit (main supervisor) and professor Ørjan Grøttem Martinsen, professor Tor Inge Tønnessen, Dr. Runar Strand-Amundsen, and Dr. Christian Tronstad (co-supervisors). This work was supported by the Norwegian Research Council through the grant BioAlert (ID 296599), and the grant LifeScience 3DR and South-Eastern Norway Regional Health Authority (ID 2020117).

The Ph.D. dissertation is a collection of five papers, presented in chronological order of writing, and a synopsis. The dissertation begins with an introductory chapter that relates the papers to each other and provides background information and motivation for the work. The papers were written and published between February 2021 and November 2022 at the Department of Clinical and Biomedical Engineering, Oslo University Hospital, and the Department of Physics, Faculty of Mathematics and Natural Sciences, University of Oslo, where I was a full-time Ph.D. student. All the content in this dissertation reflects solely my views and those of the co-authors in the five papers, not necessarily those of the affiliated organizations. I declare no conflicts of interest.

Jie Hou
Oslo, April 2023

Acknowledgements

First of all, I would like to thank my supervisors **Dr. Jan Olav Høgetveit**, **Dr. Runar Strand-Amundsen**, **Prof. Ørjan Grøttem Martinsen**, **Prof. Tor Inge Tønnessen** and **Dr. Christian Tronstad**.

My main supervisor Jan Olav Høgetveit is a very inspirational mentor, he is always supportive and helpful. He is very solution-oriented and always provides me with assistance no matter what the problem is.

Runar Strand-Amundsen is always positive and energetic. He is a very inspirational person both at work and in life, he is someone I can always rely on and talk to. I feel very lucky to have him on this journey. His support has made this work possible.

Ørjan Grøttem Martinsen has not only been a supervisor but also a friend to me for the past years. I am forever grateful for his knowledge, guidance, and encouragement. His attitude and honesty made it always easy to talk to him openly.

Tor Inge Tønnessen has been a very inspirational and resourceful mentor during the past three years. His work, skills, and capacity have been a driving force for me.

Christian Tronstad has been very resourceful, I am inspired by his range of skills, he always has ideas and solutions to every question I have asked. His help and support have been invaluable.

I want to thank Håvard Kalvøy, the leader of the Department of Clinical and Biomedical Engineering at the Oslo university hospital who kindly took me under the wings of his department. It is always easy to talk to him and he is always ready to help.

I want to thank my colleagues, Ole Elvebakk, Fred-Johan Pettersen, Tormod Martinsen, Rune Veddegjerde for your kind support and friendship.

I would like to thank my friend and colleague Sisay Mebre Abie, he is always willing to help and has been very supportive throughout the years. Thank you for all discussions we have had.

I would like to give a special thanks to my former leader and colleagues Jon Tschudi and Marion O'Farrell at SINTEF AS for their inspiration and ideas for the past years.

I want to thank the medical staff at the Institute for surgical research and the Intervention Center at the Oslo University Hospital, for their assistance during the animal experiments. Their help made it possible to conduct long-duration experiments.

I am very grateful to my family, my parents made a very hard decision by supporting me in moving from China to study aboard after high school. Their constant support and encouragement have made this work possible. Finally, I want to express my gratitude to my partner Steffen Brask, for your constant support and your patience. Thank you for always standing by my side.

List of Papers

Paper I

J. Hou, R. Strand-Amundsen, C. Tronstad, T. I. Tønnessen, J. O. Høgetveit, and Ø. G. Martinsen "Small intestinal viability assessment using dielectric relaxation spectroscopy and deep learning". In: *Scientific Reports*. Vol. 12, no. 1 3279, (2022), DOI: 10.1038/s41598-022-07140-4.

Paper II

J. Hou, R. Strand-Amundsen, C. Tronstad, J. O. Høgetveit, Ø. G. Martinsen, and T. I. Tønnessen "Automatic Prediction of Ischemia-Reperfusion Injury of Small Intestine Using Convolutional Neural Networks: A Pilot Study". In: *Sensors*. Vol. 21, No. 19, 6691, (2021), DOI: 10.3390/s21196691.

Paper III

J. Hou, R. Strand-Amundsen, S. Hødnebø, T. I. Tønnessen, and J. O. Høgetveit "Assessing ischemic injury in human intestine ex vivo with electrical impedance spectroscopy". In *Journal of Electrical Bioimpedance*. Vol. 12, No. 1, 82-88, (2021), DOI: 10.2478/joeb-2021-0011

Paper IV

J. Hou, O. M. I. Liavåg, I. H. Færden, Ø. G. Martinsen, T. I. Tønnessen, P-D Line, M. Hagness, J. O. Høgetveit, S. E. Pischke, and R. Strand-Amundsen "Utilization of dielectric properties for assessment of liver ischemia-reperfusion injury in vivo and during machine perfusion".

In *Scientific Reports*. Vol. 12, No. 1, 11183, 1-13, (2022), DOI: 10.1038/s41598-022-14817-3

Paper V

J. Hou, S. S. Ness, J. Tschudi, M. O'Farrell, R. Veddegjerde, Ø. G. Martinsen, T. I. Tønnessen, and R. Strand-Amundsen "Assessment of intestinal ischemia-reperfusion injury using diffuse VIS-NIR spectroscopy and histology".

In: *Sensors*. Vol. 22, No. 23, 9111, (2022), DOI: 10.3390/s22239111.

Contents

List of Abbreviations

AI	Artificial Intelligence
ANOVA	Analysis of Variance
AHEP	Artery Hepatic
ANN	Artificial Neural Network
ATP	Adenosine Triphosphate
AMI	Acute Mesenteric Ischemia
BER	Basal Electrical Rhythm
BNN	Bayesian Neural Network
CMI	Chronic Mesenteric Ischemia
COR	Controlled Oxygenated Rewarming
CI	Confidence Interval
CT	Computerized Tomography
CNN	Convolutional Neural Network
DHOPE	Dual Hypothermic Oxygenated Machine Perfusion
DAK	Dielectric Assessment Kit
DRS	Dielectric Relaxation Spectroscopy
DR probe	Diffuse Reflectance probe
ECG	Electrocardiogram
EEG	Electroencephalography
EIS	Electrical Impedance Spectroscopy
IRI	Ischemia-Reperfusion Injury
LSTM	Long Short-Term Memory
LDF	Laser Doppler Flowmetry
NMP	Normothermic Machine Perfusion
OCP	Open-ended Coaxial Probe
ML	Machine Learning
PCA	Principal Component Analysis
PPG	Photoplethysmogram

List of Abbreviations

PLS-DA	Partial Least Squares-Discriminant Analysis
ROS	Reactive Oxygen Species
RNN	Recurrent Neural Network
VNA	Vector Network Analyzer
VIS-NIR	Visible-Near Infrared
SG	Savitzky-Golay
SMA	Superior Mesenteric Artery
SMO	Segmental Mesenteric Occlusion
SCS	Static Cold Storage
SNV	Standard Normal Variate
SHAP	SHapley Additive exPlanations
XAI	Explainable Artificial Intelligence

List of Figures

List of Tables

Chapter 1

Introduction

This thesis is focused on new methods for assessing the viability of the small intestine and the liver. With the aim of improving the accuracy and the precision of intraoperative assessment of intestinal viability and liver graft during machine perfusion, we investigated the following modalities; dielectric parameters measured using dielectric relaxation spectroscopy (DRS), passive electrical properties measured using electrical impedance spectroscopy (EIS), microscopic images acquired from the surface of small intestine with a digital microscope and reflectance measured using visible and near-infrared (VIS-NIR) spectroscopy. Table 1.1 shows an overview of the methods investigated in this thesis and the corresponding subjects, data parameters, and papers. This thesis also describes how different machine learning (ML) models can be used to achieve a more accurate and automated classification of intestinal viability.

Table 1.1: An overview of the methods investigated in this thesis.

Method	Subject	Data	Paper
Dielectric relaxation spectroscopy (DRS)	Porcine small intestine and liver	Permittivity	I and IV
Electrical impedance spectroscopy (EIS)	Human small intestine	Impedance	III
Digital microscopic camera	Porcine small intestine	Image	II
VIS-NIR spectroscopy	Porcine small intestine	Reflectance	V

1.1 Background and motivation

1.1.1 The small intestine

The small intestine is a part of the gastrointestinal tract, between the stomach and the large intestine. It has three distinct regions: duodenum, jejunum, and ileum. The adult human intestine is about 6-7 meters [59], and the surface area is approximately 30 m^2. The main functions of the small intestine include but are not limited to digesting food from the stomach, absorbing nutrients, and extracting water.

The wall of the small intestine is composed of four main layers: serosa, muscularis propria, submucosa, and mucosa (Figure 1.1). The serosa is made of mesothelial cells. The muscularis propria consists of two layers of muscle cells, i.e., an inner circular layer, and an outer longitudinal layer. The submucosa is a flexible layer of connective tissue and the mucosa is layered by a heterogeneous epithelial cell layer [125]. Further, the mucosa can be divided into plica, villi, and crypts. Finger-like villi extend into the intestine lumen and are highly specialized for digestion and absorption [125]. The small intestine receives blood flow mainly from the superior mesenteric artery (SMA).
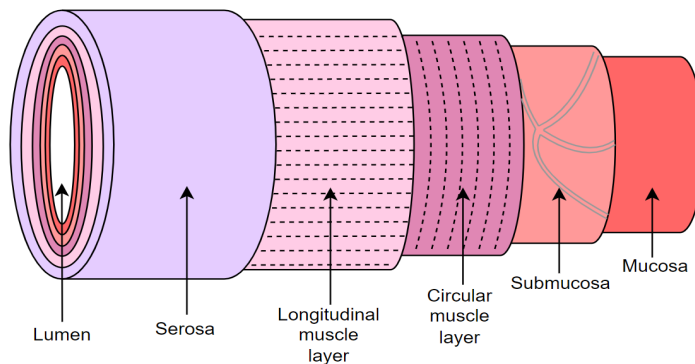
Figure 1.1: A simplified overview of the layers of the small intestine.

1.1.2 The liver

The liver is an organ of the digestive system located in the right upper quadrant of the abdomen in humans. It is a complex organ with multiple functions, including regulation of the metabolism of nutrients, detoxification of endogenous substances and drugs, and bile production [42]. An important function of the liver is the production of bile, which is a fluid containing cholesterol and bile acid that is used to digest fat. The liver receives blood from the portal vein and the hepatic artery, where the portal vein delivers around 75% (of the total amount of blood that the liver receives) of nutrient-rich blood to the liver and the hepatic artery delivers around 25% of oxygen-rich blood. The biliary tree receives blood supply only from the hepatic arteries. Occlusion of the hepatic artery will result in ischemic necrosis of the biliary tree while the parenchymal cells will survive due to the blood supply from the portal vein.

The liver consists of parenchymal hepatocytes (70–85%), and sinusoid walls contain endothelial cells, smooth muscle cells, and fibrous tissue. Parenchymal hepatocyte cells play vital roles in metabolic functions, detoxification, and protein synthesis [146]. Kupffer cells are located in the sinusoid and play an important role in liver regeneration and protect the liver from bacterial infections [42]. Figure 1.2 shows the liver structure and cell types. Different cell types undergo a range of pathophysiological changes during IRI.

1.1.3 Ischemia-Reperfusion injury

Ischemic injury is caused by the restriction of blood supply, resulting in a shortage of oxygen and nutrient deliveries required for cellular metabolism and inadequate disposal of metabolic wastes. The main mechanism of ischemic injury is tissue hypoxia, which reduces ATP production and disrupts cell volume regulatory mechanisms [65]. Anaerobic metabolism results in the production of lactic acid which acidifies the cell with protons. ATP degradation also produces protons (H^+), and the sodium-proton exchanger extrudes accumulating protons
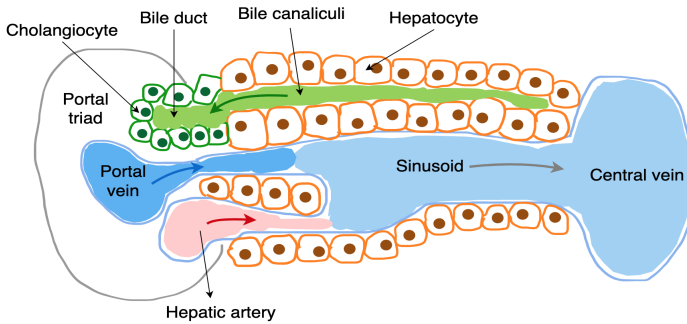
Figure 1.2: Liver structure and cell types. The liver is structured with lobules and within each lobule are a number of sinusoids, which are discontinuous vessels built from specialized fenestrated endothelial cells. Bile ducts are exclusively perfused by arterial blood from the hepatic artery, rendering them very vulnerable to ischemia if the arterial flow is reduced by for instance thrombosis. The figure is reproduced from Figure 1B in reference [42] with permission from the author.

in exchange for sodium ions causing sodium influx [65]. This rise in intracellular sodium will by osmosis force interstitial water to enter the cell resulting in swelling (edema). Subsequently intracellular and mitochondrial calcium levels will increase. During hypoxia, resident polymorphonuclear leukocytes (white blood cells) also migrate from the intravascular space to the interstitium, which may contribute to tissue injury during reperfusion [31]. During reperfusion, more polymorphonuclear leukocytes migrate to the interstitium and contribute to the development of tissue reperfusion injury. The endothelial barrier may be disrupted due to the polymorphonuclear leukocyte mobilization, potentially leading to extravascular fluid leakage and edema formation [31].

Ischemia-reperfusion injury (IRI) is caused by a series of immune system responses triggered by the return of blood supply after a period of ischemia. This means that the body in essence is harming itself by some of its own protective mechanisms. There are several mechanisms occurring during IRI, some of which work in cascades, triggering each other. At the early stage of reperfusion, reactive oxygen species (ROS) are generated from accumulated hypoxanthine. As extracellular pH returns to normal (pH $\sim$ 7.4) upon reperfusion, the intracellular protons are extruded, which returns the intracellular pH to normal [92]. Accumulation of ROS in the reperfused tissue is an important cause of tissue injury and also a trigger for subsequent inflammation.

IRI can induce apoptotic or necrotic cell death, potentially leading to tissue destruction if the IRI is extensive. Oxidative stress and the production of ROS induce apoptosis, which plays a fundamental role in cellular damage during IRI [23]. The leakage of cytoplasm and mitochondrial DNA from dying cells amplifies the inflammatory response [47]. Overall, IRI is a multifactorial response and a highly complex series of interwoven pro-inflammatory and pathological events, where there still is ongoing research to understand the mechanisms and

how these various events interchange [23, 114, 138].

1.1.4   Assessment of intestinal viability

Mesenteric ischemia typically begins with occlusive or non-occlusive obstruction in or close to the mesenteric vessels of the small intestine. The obstruction can occur either on the arterial or the venous side [43]. There are two types of mesenteric ischemia; acute mesenteric ischemia (AMI) and chronic mesenteric ischemia (CMI). AMI is caused by a severe decrease in blood flow (sudden onset of intestinal hypoperfusion caused by a thrombus or embolus in the superior mesenteric artery tree) and accounts for 1-2 of 1000 acute surgical admissions [4]. CMI is caused by plaque building up inside the wall of the mesenteric arteries, thus slowly blocking the blood flow through the artery (causing intermittent intestinal hypoperfusion). The incident rate of CMI is low, accounting for less than 1 in 1000 hospital admissions for abdominal pain [100].

Mesenteric ischemia usually results in diffuse symptoms, making it challenging to be diagnosed. The standard diagnostic methods are mesenteric angiography and multidetector computed tomography (CT) angiography [51, 88], combined with patient history and physical examination. Once diagnosed, surgery will be initiated either in the form of endovascular treatment[1], laparoscopy[2] or explorative laparotomy[3] [6]. Visual inspection of intestinal movement and return of color is performed once the abdominal cavity is accessed, and perfusion is then restored to the ischemic tissue [12, 13, 52, 98, 107, 126]. Assessment of intestinal viability relies heavily on clinical experience and is typically not very specific and often unreliable [130]. Once the decision of resection is made, more challenges appear. For instance, the surgeons need to select the resection margins in order to preserve the viable intestinal segments as much as possible while removing the non-viable ones. If the resection is performed too excessively, the patient can suffer from short bowel syndrome, with an impaired ability to absorb nutrients and remove liquid. If a segment of an irreversibly injured intestine remains in the patient, complications like intestinal malfunction, and leakage of intestinal fluid through necrosis in the intestinal wall cause severe peritonitis that may cause sepsis and multiple organ failure. At a later stage, stricture may occur.

Acute intestinal ischemia has a high mortality rate, often ranging between 60–80% even with a surgical intervention [27]. Those who have large parts of the intestines removed during one or repeated surgeries are left with a risk of short bowel syndrome. The gold standard to determine intestinal viability is a second-look operation (within 72 hours), in order to reinspect the segments in question [142]. Identifying non-viable segments during the first laparotomy is reported to be challenging [106]. The overall accuracy in assessing intestinal tissue viability is increased [13, 106] when a second-look laparotomy is performed. Developing new techniques to assess intestinal viability more accurately, in an

---

[1]Minimally invasive procedures that are done inside the blood vessels.
[2]Minimally invasive surgical procedure that allows a surgeon to access the inside of the abdominal cavity.
[3]Large surgical incision that allows a surgeon to access a large part of the abdominal cavity.

objective and reproducible way, has the potential of improving the outcomes of this patient group.

Over the past decades, different approaches have been investigated by researchers, aiming to develop reliable methods to increase the accuracy of intraoperative assessment of intestinal viability. Table 1.2 shows an overview of methods related to the assessment of intestinal viability.

Table 1.2: An overview of previous experimental approaches in the assessment of intestinal viability.

Methods investigated	Related work
Doppler ultrasound	[13], [21], [54], [111]
Laser Doppler flowmetry (LDF)	[61]
Pulse oximetry	[29], [32], [78]
Fluorescence methods	[10], [56], [63], [48]
Hydrogen gas clearance	[89], [97]
Infrared imaging	[11], [90]
Light spectroscopy	[8], [69], [73], [115]
Impedance spectroscopy	[85], [119, 120, 121, 122]
Microdialysis	[28], [118]

Assessment of the small intestinal IRI condition using EIS has been studied quite extensively by Strand-Amundsen et al. [119, 120, 121, 122] during the past years. They studied the trans-intestinal electric properties using a 2-electrode setup and reported that the time development of the electrical properties differ between the perfused and the ischemic intestinal tissue, in porcine models with segmental mesenteric occlusion (SMO).

In this work, we extended the study of using EIS to monitor passive electrical properties during ischemia in the human intestine. Furthermore, we investigated the differences in the electric properties between the porcine intestine and the human intestine, to evaluate the translation value of the results from the porcine models.

Dielectric relaxation spectroscopy (DRS)[4] has been reported to be useful in evaluating the viability of tissue after ischemic injury [141]. However, to the best of our knowledge, dielectric properties in the GHz region have not been investigated on the small intestine during IRI in vivo. In this work, we use DRS to assess the dielectric properties of the small intestine during the ischemia and reperfusion phase, in a porcine model.

Various imaging techniques have been investigated to assess the small intestinal IRI condition. While visual inspection by the surgeon is used for standard clinical assessment, so far no one has investigated whether microscopic images of the surface of the intestine contain information that can be used to predict intestinal viability. We utilized deep learning methods together with

---

[4]A subcategory of impedance spectroscopy.

microscopic images to process and analyze the image data, to be able to evaluate the intestinal IRI condition.

Light spectroscopy has been used to assess the IRI condition of the small intestine. Sowa et al. [115] used near-infrared spectroscopy to detect intestinal ischemia in a porcine model, and Karakas et al. [69] used diffuse reflectance spectroscopy to investigate the viability of the intestine in a rat model. Both works reported measurements on a small area with dimensions in the order of a few square millimeters. Due to the heterogeneity of the small intestine in the square millimeter range, "single point" measurements can easily introduce measurement errors and cause low reproducibility of data. In this work, we intended to investigate whether measurements of larger areas (centimeters range) of the intestinal tissue could provide more accurate data and thus more precise prediction of viability.

1.1.5   Assessment of liver viability

The waiting list for liver transplantation is increasing over time. The discard rate of livers from donors is 26.6% (donation after circulatory death) and 7.1% (donation after brain death) [76]. IRI is the main challenge in organ transplantation due to its complex nature and nonmanifest appearances, which leads to short- and long-term transplanted graft failure. With respect to liver IRI, several mechanisms can compromise the viability of the liver graft.

In vivo ischemia decreases ATP production in mitochondria and induces anaerobic metabolism. Dysfunction of the sodium-potassium pump causes gradual cellular swelling. During the cold storage phase, the liver is ischemic, but the tissue metabolism is slowed due to the temperature drop, which delays tissue injury. However, if the cold storage phase is prolonged, the sinusoidal endothelial cells become susceptible to apoptosis and coagulative necrosis, and the activation of Kupffer cells increases[5]. These mechanisms correlate with low liver viability upon reperfusion [72].

The current evaluation methods in deciding whether a donated liver is transplantable or not are based on visual inspection together with an evaluation of patient history and blood parameters related to liver function. The low accuracy of the current liver viability evaluation methods leads to potentially functional livers being discarded. It is better to discard a liver that one is unsure about than to transplant it and later discover that it does not function in the recipient. Therefore, robust objective evaluation methods are needed to enable clear differentiation between functional and non-functional livers.

Studies have shown that up to 20% of marginal livers[6] can have restored functionality when perfused on an ex vivo perfusion machine and can thus be available for transplantation [93]. Perfusion machines enable both treatment and evaluation of the donated livers prior to transplantation. Some of the ischemia

---

[5]Which stimulates other immune cells, leading to increased ROS and cytokine production.
[6]Livers that have a high risk for non-function after transplantation.

and reperfusion injuries that the liver has experienced can be reversed by the state-of-the-art machine perfusion approach [93, 105].

Reperfusion of the liver involves warm blood from the recipient entering the transplanted liver, which carries a risk of liver injury. This is due to the activation of immune cells, the production of oxidant stress in hypoxic tissue, and the abrupt transition from cold perfusion solution to warm blood. The normothermic perfusion phase (NMP) provides valuable observation time for the surgeon to evaluate the IRI condition of the liver.

Based on the current challenges in transplantation, several approaches have been investigated to assess liver graft viability (Table 1.3).

Table 1.3: An overview of previous experimental approaches in the assessment of liver viability.

Methods investigated	Related work
Impedance spectroscopy	[1], [24], [123]
Microdialysis	[35], [67, 68], [113], [128, 129], [136, 137]
pH, pCO_2 and pO_2 sensors	[127], [102]
Imaging techniques (including Ultrasound and fluorescence)	[22], [17], [49], [112], [140], [139]
Intravital microscopy and spectroscopy	[96]

Impedance spectroscopy has been used to study the electrical properties of the liver. O'Rourke et al. [94] and Peyman et al. [101] investigated how different pathological changes affect the dielectric properties of the liver. Farrugia et al. [36] reported the dielectric properties of rat liver in vivo in the frequency range of 500 MHz to 40 GHz and pointed out some differences between in vivo and ex vivo data. In this work, we have used DRS to assess the dielectric properties of a porcine liver, both in vivo and during machine perfusion.

1.2 Aim and Objectives

The overall aim of this work is to explore new methods for more accurate and objective intraoperative assessment of the viability of the small intestine and the liver. Accurate early diagnosis may reduce the need for second or third-look operations of the intestine and excessive removal of the viable intestine, and avoid discarding livers that can potentially be transplanted. This work is motivated by the high mortality and morbidity rates associated with intestinal ischemia and the high discard rate of potentially viable livers [93].

To achieve the overall aim, we have defined the following objectives:

1. Investigate the feasibility of measuring dielectric parameters of the porcine small intestine in vivo, using DRS.

2. Study how the dielectric parameters of the porcine intestine in vivo are influenced by ischemia and reperfusion.

3. Investigate whether microscopic images taken from the small intestine surface in vivo, combined with machine learning, can be used to assess the viability of the intestine.

4. Study how the passive electrical properties of the human small intestine are influenced by ischemia ex vivo.

5. Investigate whether bioimpedance measurements can provide an indication of the viability limit of the human intestine ex vivo, compared to the available viability limit provided by histological analysis.

6. Investigate the usability of measuring dielectric parameters of porcine liver both in vivo and during NMP, and how changes in dielectric parameters are associated with IRI.

7. Investigate the time needed on NMP before a reliable assessment of liver viability can be made.

Paper I investigates the feasibility of using DRS to study how the dielectric properties of the porcine small intestine are affected by IRI. Machine learning models were built to automatically classify viable and non-viable intestinal segments based on permittivity data.

Paper II investigates whether microscopic images from the surface of the small intestine, combined with machine learning, can be used to automatically detect different levels of intestinal IRI, in a porcine model.

Paper III investigates how the passive electrical properties of the human intestine ex vivo are influenced by ischemia, and compares the viability limit estimated from bioimpedance measurements with the available references provided by histological analysis.

Paper IV investigates using dielectric parameters in the assessment of liver graft viability during partial warm ischemia and full cold ischemia, both in vivo and during machine perfusion.

Paper V investigates the use of diffuse VIS-NIR spectroscopy with partial least squares-discriminant analysis (PLS-DA) and histopathological analysis, to assess the degree of intestinal perfusion.

Chapter 2

Methodological Considerations

2.1 Models of tissue ischemia

We have used models to investigate the pathophysiology of ischemia and ischemia-reperfusion, while measuring selected parameters, in the organs of interest. For the in vivo experiments on the small intestine, we used a segmental mesenteric occlusion (SMO) model in pigs (Papers I, II and V); For the ex vivo human small intestinal ischemia we used a resection model, where the resected intestine segments were kept in a controlled environment during the experiments (Paper III); For the liver experiments, we used a hepatic artery occlusion model in vivo in pigs and an ex vivo normothermic machine perfusion (NMP) model (Paper IV).

2.1.1 Ethical approval

The porcine experiments were approved by the Norwegian Food Safety Authority (NFSA) with FOTS ID 12695, 24454 and conducted in accordance with national animal welfare guidelines (FOR-2015-06-18-761) and EU directive (2010/63/EU). All experiments with the small intestine (both human and porcine) were funded through The Research Council of Norway, BioAlert project (ID 296599). Funding for the experiments involving livers was provided by the University of Oslo, LifeScience 3DR, and South-Eastern Norway Regional Health Authority (grant 2020117). The approval for the experiments involving samples of human intestine ex vivo was given by the Regional Committees for Medical and Health Research Ethics[1] (2018/1630 REK sør-øst D).

2.1.2 Study population

Table 2.1 shows an overview of the study population in the experiments conducted for this thesis.

Table 2.1: An overview of the study population.

	Paper I	Paper II	Paper III	Paper IV	Paper V
Subject	Pig	Pig	Human	Pig	Pig
Type of experiment	In vivo	In vivo	Ex vivo	In- and ex vivo	In vivo
Number of subjects	8	10	8	21	10
Sex [F/M]	5/3	5/5	N/A	10/11	3/7
Weight [kg]	50–66	50–66	N/A	54–66	48–54

---

[1] Regionale komiteer for medisinsk og helsefaglig forskningsetikk (REK).

Three pilot experiments were conducted to test the instrumental setup for each of the studies and the results are unpublished and not included in this thesis.

2.1.3 Segmental mesenteric occlusion model in pigs (Papers I, II and V)

Research on animal models has extensively expanded our knowledge and possibilities for investigating IRI. Porcine models have been advocated for translational studies due to their important anatomical and physiological similarities to humans [30, 41, 116, 147]. The segmental mesenteric occlusion model (SMO) was selected as it provides a well-defined area of ischemic injury in the occluded segment [40, 143]. The SMO model was induced by atraumatic clamping (causing strangulation-obstruction) (Figure 2.1) of the arteries and veins of the intestinal mesentery, leading to ischemic injury [40]. After a defined period with obstruction (1–8 hours, Papers I, II and V), reperfusion was initialized by releasing the clamps and gently massaging the mesenteric blood vessels if needed, to ensure the return of blood in the individual arteries and veins.
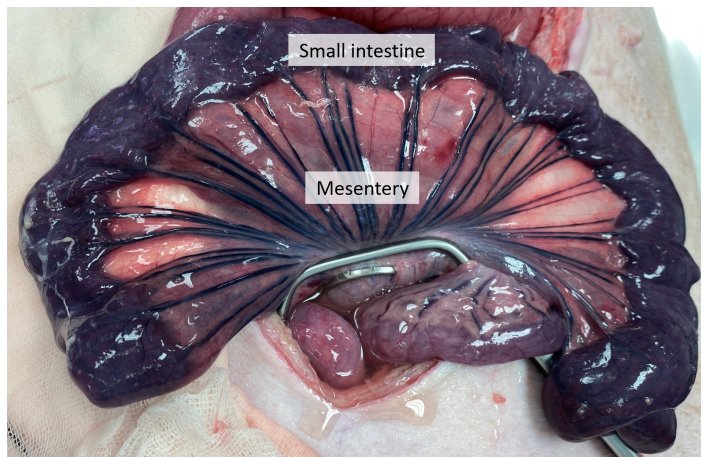
Figure 2.1: Segmental mesenteric occlusion model applied on the porcine intestine.

The length of the porcine small intestine is between 15–20 meters [86], allowing for several parallel SMO models to be created in each of the porcine subjects. We selected the jejunum for the model, as it is a large and available intestinal structure. We maintained a distance of at least 20–30 cm between each occluded segment to avoid interference. Some studies report that late reperfusion intervals can give unwanted systematic responses such as increased heart rate and decreased blood pressure, which may be related to the release of harmful substances following late reperfusion [15, 118, 135]. A study using light- and transmission-electron microscopy together with microdialysis and histological

grading systems, reported that undesirable effects from parallel SMO models are unlikely to have any confounding effects on the outcome of the experiments [118].

2.1.4 Ex vivo model with human intestine (Paper III)

Over the years, several studies have reported bioimpedance measurements in animal models. To the best of our knowledge, evaluation of intestinal viability has not been reported using bioimpedance measurements and the P_y parameter[2] on the human small intestine. In this work, we used resected human small intestinal segments from 8 patients who underwent standard pancreaticoduodenectomy[3]. The resection of the small intestine did not involve any extra surgical procedures for the patients. The small intestinal segments (length range 10–15 cm) were received immediately after the resection and placed inside a container with a Ringer-solution with 4% Albumin. The container was kept in a water bath with a constant temperature of 37°C.

2.1.5 The liver machine perfusion model (Paper IV)

Machine perfusion is a new approach that aims to increase transplantation rates by decreasing liver injury during preservation and restoring liver functionality prior to transplantation [105]. The Liver Assist perfusion machine (XVIVO-Abdominal, Groningen, The Netherlands) was used for all the liver experiments (Figure 2.2). The perfusion machine is equipped with two perfusion lines, providing oxygenated pulsatile perfusion to the hepatic artery and continuous flow through the portal vein. There are two hollow fiber membrane oxygenators for gas exchange, and the integrated heater/cooler unit enables perfusion with flexible temperature [60, 108].

After procurement, the livers were placed on the back table with cannulation of the hepatic artery, portal vein, and biliary duct. In this work, three models were established for the different liver groups:

- Control (CON) (N = 7): 4 hours in vivo monitoring followed by a short period (1–2 hours) of static cold storage before machine perfusion after procurement.

- Biliary injury (AHEP) (N = 7): 4 hours of partial warm ischemia with hepatic artery occlusion (where the hepatic artery was fully occluded, while the portal venous flow was intact) prior to liver procurement followed by a short period (1–2 hours) of static cold storage before machine perfusion.

- Global hepatic injury (SCS) (N = 7): 4 hours in vivo monitoring followed by static cold storage for 18–20 hours (in order to establish a liver with serious hepatic injury) prior to machine perfusion.

---

[2]The P_y parameter reflects the integrity of the cell membranes [103] and it is introduced in section 2.2.5.3 in detail.

[3]Whipple procedure, where the surgeon removes the head of the pancreas and a part of the small intestine.
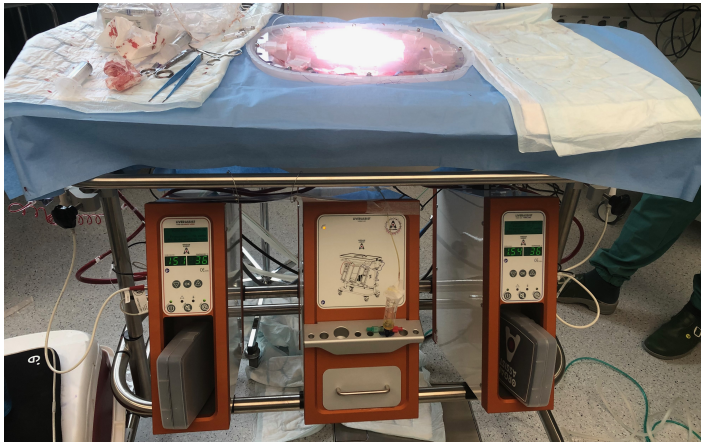
Figure 2.2: The Liver Assist perfusion machine.

Ex vivo reperfusion was performed using NMP with autologous blood, with gradually increasing temperature up to 37.5°C within one hour.

During both in vivo and ex vivo monitoring, the liver functionality was evaluated by bile production (in ml), blood flow, mitochondrial function, tissue CO_2 level with CO_2 sensors, concentrations of lactate, glucose, pyruvate and glycerol by microdialysis, in addition to measurements of dielectric properties using DRS.

2.2 Electrical impedance spectroscopy

Electrical impedance spectroscopy (EIS) is a well-established technique that has been used to characterize the electrical properties of materials. Electrical bioimpedance is commonly used in the field of biology [46], due to its non-destructive and non-invasive nature, and it is considered a promising method for early diagnosis in the medical field [87, 144]. The bioimpedance technique is also one of the approaches suggested for the assessment of tissue ischemia and viability [74, 75, 130].

Bioimpedance measurements can be used to assess the passive electrical properties of biological tissue. When a voltage is applied to a tissue, it creates a current that is dependent on the impedance of the tissue. The equation of impedance (Z) can be derived from Ohm's law (Equation (2.1)):

$$Z = \frac{U}{I} \quad [\Omega] \tag{2.1}$$

where U is the applied voltage in volts and I is the current in amperes.

$$\mathbf{Z} = R + jX \quad [\Omega] \tag{2.2}$$

$\mathbf{Z}$ is the impedance (Equation (2.2)), consisting of two components, resistance (R) and reactance (X). Where R represents the ability of the material to dissipate

energy when placed in an electromagnetic field, and X is the ability to store energy. In biological materials, energy storage is predominantly in the form of capacitive properties. The modulus of the impedance is shown in Equation (2.3).

$$|Z| = \sqrt{(R^2 + X^2)} \quad [\Omega] \tag{2.3}$$

$$\varphi = \arctan\left[\frac{\text{Im}(Z)}{\text{Re}(Z)}\right] = \arctan\left(\frac{X}{R}\right) \quad [\text{rad}] \tag{2.4}$$

Phase angle φ (Equation (2.4)) is the phase shift between current and voltage of the measured impedance, which is the arc tangent of the imaginary part of the complex impedance ($\text{Im}(Z)$) divided by the real part of the complex impedance ($\text{Re}(Z)$) [46].

2.2.1   The complex dielectric nature of tissue

Biological tissue is neither a perfect conductor nor an ideal insulator but carries properties of both. A material's electrical properties are a direct consequence of its composition and structure. A dielectric material can be considered an electrical insulator that can be polarised by an externally applied electric field. Biological tissue has dielectric properties. When biological material is subjected to an electric field, the applied electric field can distort the charge distribution of the ions and molecules by rotation, stretching, and vibration. Each molecule inside the material has its own dielectric property, which describes the electric polarizability of the molecule.

Permittivity is one of the fundamental material properties, which describes the interaction between a material and an externally applied electric field. Permittivity is a measure of the material's ability to be polarized in an external electric field.

$$\epsilon_r^*(\omega) = \frac{\epsilon^*(\omega)}{\epsilon_0} = \epsilon_r'(\omega) - j\epsilon_r''(\omega) = \epsilon_r'(\omega) - j\frac{\sigma(\omega)}{\omega\epsilon_0} \tag{2.5}$$

Complex permittivity (Equation (2.5)) is defined as a function of the angular frequency ω, which is rated relative to the permittivity in the vacuum, ϵ_0. ϵ_r' is the dielectric constant or relative permittivity, which describes the interaction between a material and an externally applied electric field. The dielectric constant expresses the ability of a biological material to store energy when an electric field is applied. In addition, the complex relative permittivity ϵ_r^* contains an ohmic loss term ϵ_r'' which is the dielectric loss that influences the energy absorption or attenuation of the material, reflecting the dissipative nature of the material. The movements of dipoles due to the alternating electric field causes interactions, collisions, and friction which is partially dissipated into heat [77]. Furthermore, the ohmic loss arises from the steady-state migration of the ions under the influence of the electric field. It is also characterized by the conductivity σ as a function of the angular frequency which is described by the dielectric loss [77].

There are mainly four different polarization mechanisms that contribute to the permittivity of a material. At the frequency range of 1 kHz to 100 GHz, permittivity is dominated by ionic and dipolar polarization. When the frequency exceeds 100 GHz, atomic and electronic polarization becomes prevalent (Figure 2.3).
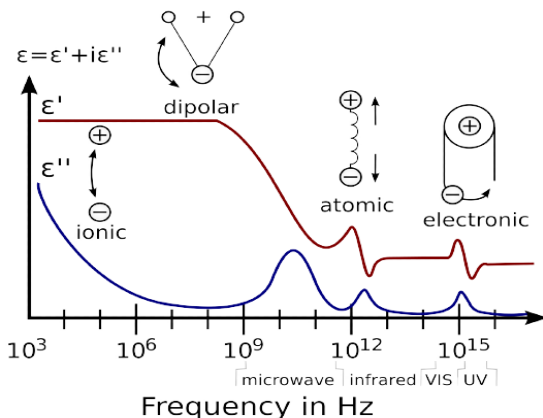
Figure 2.3: An ideal representation of the dielectric mechanisms as a function of frequency. From reference [134], licensed under a Creative Commons Attribution 4.0 International License (CC BY 4.0).

1. Ionic polarization: Occurs due to the displacement of the positive ions relative to the negative ions. Ionic materials have internal dipoles which exactly cancel each other and are unable to rotate in their resting state. When an electric field is applied to an ionic material, the cations and anions re-position themselves giving rise to a net dipole moment.

2. Dipolar polarization: Occurs for polar molecules with permanent dipoles. Using the water molecule as an example, it has a skewed charge distribution where the positively charged side is separated from the negatively charged side, and this separation forms a permanent dipole [46]. When a polar molecule is subjected to an electric field, it will reorient itself according to the polarity of the externally applied electric field. The orientational polarization depends on temperature, pressure, and chemical surroundings.

3. Atomic polarization: Occurs when there is a relative change in the position of the atomic nuclei which causes a change in dipole moment within the molecules. Atomic polarization is faster than dipolar polarization, which occurs in the picosecond range.

4. Electronic polarization: Occurs when the negatively charged electron clouds of individual atoms are displaced with respect to their positively charged nucleus, in an externally applied electric field. They are called induced dipoles which align in the same direction as the electric field. Electronic polarization is considered the fastest polarization mechanism and happens in the femtoseconds range.

The rotational movements of dipoles follow the polarity of the applied electric field. The dipoles will rotate to follow the direction of the electric field and finally reach a final state of polarization. Once the alternating electric field changes its direction, the process is reversed. With increasing frequency, the dipoles will not be able to follow the rapidly alternating electric field and instead start vibrating, which leads to an increased energy loss (dielectric loss). This energy loss is proportional to the relaxation frequency (f_r), which is when the dipoles are unable to follow the alternating electric field. The relaxation frequency is reversely proportional to the relaxation time $(\tau)^4$, which is a measure of the mobility of the dipoles in a material. Above the relaxation frequency, both the dielectric constant and the dielectric loss decrease. This is due to the polarity of the electric field changing so fast that it can no longer influence the dipoles, thus dipole polarization disappears.

2.2.2 Relaxation and dispersion mechanisms

Permittivity dependency as a function of frequency is called dispersion. Different mechanisms give rise to dielectric dispersions. The dielectric permittivity of a biological material typically decreases with increasing frequency in four major steps [83] (Figure 2.4).
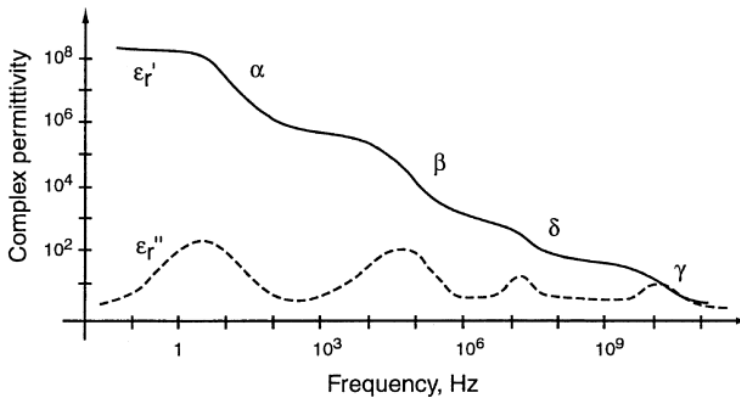
Figure 2.4: An ideal representation of complex permittivity as a function of frequency according to the relaxation mechanisms. From Figure 1 in reference [83] with permission from the author.

α-**dispersion** occurs in the lower hertz to the 10 kHz range, characterized by very high permittivity values and large dielectric decrements [5]. In tissue, it mainly accounts for counter-ion effects near the cell membrane, active cell membrane effects, ionic diffusion, and dielectric losses.

β-**dispersion** occurs in the intermediate frequency range which extends 3 to 4 frequency decades (10 kHz–10 MHz), which is known as interfacial polarization

---

[4]$\tau = \frac{1}{2\pi f_c}$

or the Maxwell-Wagner effect [5]. In tissue, it originates mostly from passive cell membrane capacitance associated with the ability of the cell membrane to filter out low-frequency current. It allows high-frequency current to pass through as the membranes are electrically shorted at high frequencies.

δ-**dispersion** is likely produced by the dipolar relaxation of the bound water in a material, the relaxation of small dipolar segments or side chains of larger molecules. It has a bimodal structure associated with both tightly bound and loosely bound water [14]. Hydration water is attributed to the dipole moment of larger molecules. This dispersion is much weaker than the γ-dispersion. Therefore, it is often difficult to isolate and interpret compared to the other dispersion mechanisms.

γ-**dispersion** is a dipolar mechanism in polar media like water. At frequencies of the high megahertz and low gigahertz region, where the response of water is the dominating mechanism, the complex permittivity can be expressed by a Cole-Cole model in addition to a conductive term, to simulate the dipolar dispersion of water together with the contribution of the electrolytes.

2.2.3   Electrical properties of tissue

Impedance spectroscopy has been utilized to investigate how the electrical properties change with respect to IRI in various tissues [3, 38, 62, 74, 110]. Both ischemia and reperfusion injury leads to physical alternations on several levels in the affected tissue, which in turn result in changes in the electrical properties. There are several mechanisms that connect the alternations in electrical properties to the physical changes in the tissue undergoing IRI.

At low frequencies (low Hz–few kHz), the closing of gap junctions and the narrowing of extracellular pathways due to cell swelling contributes to increased resistance [3, 37, 46]. Later on, reduced membrane resistance due to the opening of ion channels and increased membrane permeability is caused by prolonged ischemic exposure [46, 110]. At frequencies in the kHz and low MHz region, the β-dispersion (associated with cell membrane integrity) starts to disappear as the cell membranes lose integrity due to prolonged ischemic injury [101, 103]. Formation of extracellular edema and later, cell necrosis, will lead to a decrease in the overall impedance throughout the frequency spectrum [84].

As frequency exceeds the GHz region, we no longer measure contributions from cell membranes. Instead, the dipolar molecules start to dominate, where changes in the concentration of dipolar molecules are reflected in the measured frequency-dependent spectrum.

2.2.4   Instrumentation setups

2.2.4.1   Bioimpedance measurements (Paper III)

Impedance measurements were performed with a Solartron 1260 Impedance/gain-phase analyzer (Solartron Analytical, UK) with a 1294A interface. A two-electrode setup with Ag/AgCl electrocardiography disc electrodes (intrinsic R

= 0.18 Ω, X = 0 Ω) with 9 mm in diameter (Quickels System AB, Sweden) was used for impedance measurements. The selection of electrode setup was based on earlier work conducted by Strand-Amundsen et al. [117], where they found that the two-electrode setup (Ag/AgCl) is most suitable for measurements on the small intestine. Compared to the two-electrode setup, the sensitivity of the three-electrode setup remains near the surface due to the well-conducting wet serosa surface, and the subserous layer (a layer of connective tissue) with higher resistivity [117]. A four-electrode setup is more vulnerable to erroneous measurements [45]. Since the wet surface of the small intestine is well-conducting, the current can shunt across the pick-up electrodes, leading to the potential of the pick-up electrodes being near the potential of the current-carrying electrodes. This can typically lead to an overestimation of the transfer impedance [117]. 9 mm diameter electrodes were chosen based on the observation of the physical structure of the small intestine, where the small structures on the intestine surface vary with a repetitive pattern on the 2-3 mm scale. By using electrodes that cover several repetitions, we estimate to measure the average effect in the tissue over a volume of the intestinal wall [117]. Both the electrode material Au and Ag/AgCl performed well on tissue measurements, the Ag/AgCl electrodes were chosen based on availability.

Figure 2.5: Experimental setup for bioimpedance measurements on the human small intestine.

Measurements on the small intestine were performed once an hour. A 50 mV AC signal was applied across the electrodes, while 41 steps in the frequency range of 100 Hz–1 MHz were swept. The resulting current was measured and

calculated into complex impedance in the ZPlot software (Scribner Associates, USA). For experiments on the human intestine, the samples were removed from the storage container and were gently placed between the two electrodes during measurements (Figure 2.5).

2.2.4.2 Microwave dielectric measurements (Papers I and IV)

Dielectric relaxation spectroscopy (DRS) is a subcategory of EIS and measures the dielectric properties of a medium as a function of frequency. DRS was performed with a vector network analyzer (VNA) and an open-ended coaxial probe (OCP) [44].

A vector network analyzer measures the transmission and reflection of an applied signal. A network analyzer consists of a source, a signal separation device, and a detector. When using a VNA to analyze a material, a sinusoidal signal is generated to stimulate the material under test. In practice, a sample is placed at the end of the OCP, and a sinusoidal signal passes through the sample. Moreover, the measuring of the complex reflection coefficient Γ^* will take place at the end of the OCP. The reflection coefficient is the ratio of the reflected signal voltage to the incident signal voltage. The magnitude of the reflection coefficient varies from 0 which means no reflection to 1 which means total reflection. From Γ^*, the dielectric properties can be determined [9, 79].

An open-ended coaxial probe is a coaxial line that is a cut-off section of a transmission line. Figure 2.6 shows the top and the side cross-sections of an OCP. Measurements with an OCP rely on analysis of the reflection of the electric field from the boundary between the probe and the material under test. There are several methods to measure the dielectric properties of biological materials when using VNA, including the transmission line, cavity, multi-electrode probe, and OCP techniques. Amongst these methods, the coaxial probe technique is the most commonly used [77]. This is due to the operational simplicity and the non-destructive sample handling of the coaxial cable as well as the possibility of measuring over a broad frequency range.
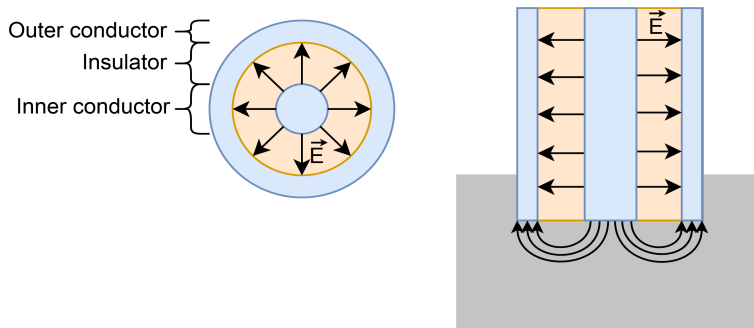
Figure 2.6: Top and side cross-sections of an OCP, with electric field orientation indicated. The grey area is the material under test.

The electric wave propagates along the coaxial line toward the material under test, and when there is an impedance mismatch between the probe and the sample, a reflection will occur. The reflected signal is returned to the VNA to be converted into complex permittivity values.

The DAK 3.5 (200 MHz–20 GHz) probe (Schmid & Partner Engineering AG, Switzerland) and the R140 (85 MHz–14 GHz) VNA (Copper Mountain Technologies) were used in this thesis. Combining the frequency limitations of the OCP and the VNA, the frequency range for our experimental setup was 200 MHz–14 GHz, and 167 frequency points were acquired from each measurement.

The R140 VNA has a frequency resolution of 25 Hz and it uses 200 μs to measure one frequency point, resulting in 33.4 ms to complete one frequency sweep. The internal impedance is 50 Ω and the input power applied during the measurement is 0 dBm (1 milliwatt). The inner and outer conductor dimensions of the DAK 3.5 probe were $a = 0.93$ mm and $b = 3.5$ mm, respectively. The dielectric bead material of the probe is Eccostock (a low-loss plastic stock with a well-defined dielectric constant at $\epsilon' = 2.538$). It is frequency independent over the entire frequency range of the probe.

Prior to the measurements, the system was kept in calibration mode, which includes three independent standards: Open circuit (performed in the air after rinsing with ethanol), Short circuit (short-circuiting using a copper strip), and Load circuit (measurement with deionized water). The quality of the calibration was then validated using a reference liquid with known permittivity. For all experiments, 500 ml of 0.05 Molar saline solution was used as a validation liquid. During the validation process, the measured permittivity spectrum of the saline sample was compared with the target reference data for 0.05 M saline. Calibration was qualified when the difference between the measured saline data and the target saline data was lower than $\pm 2\%$.

Measurement errors related to the use of a VNA can be divided into; random errors and systematic errors. Random errors have no pattern and are by definition unpredictable. By averaging several measurements, we tried to keep the random errors as low as possible. We tried to minimize the systematic error by keeping the measurement condition as close to the calibration condition as possible. We handled this by maintaining the same ambient temperature for both calibration and measurement, and by performing the measurements as soon as the system was calibrated. We ensured that the probe temperature was the same as the sample temperature by waiting for a minute after placing the probe in contact with the tissue, to make sure that the probe has reached the same temperature as the tissue. For the in vivo pig experiments, the small intestinal segments under test were placed inside the abdomen between the hourly measurements in order to maintain a stable temperature and humidity.

During measurements, a metal stand that holds both the VNA and the probe and a 3D-printed clip that fits the tip of the coaxial probe were used, to ensure that the same pressure was applied to the tissue (Figure 2.7). The small intestinal tissue (Figure 2.7a) and the liver tissue (Figure 2.7b) were slightly clamped between the clip and the probe surface to ensure good contact (avoiding partial contact and air bubbles). Erroneous measurements resulting from probe
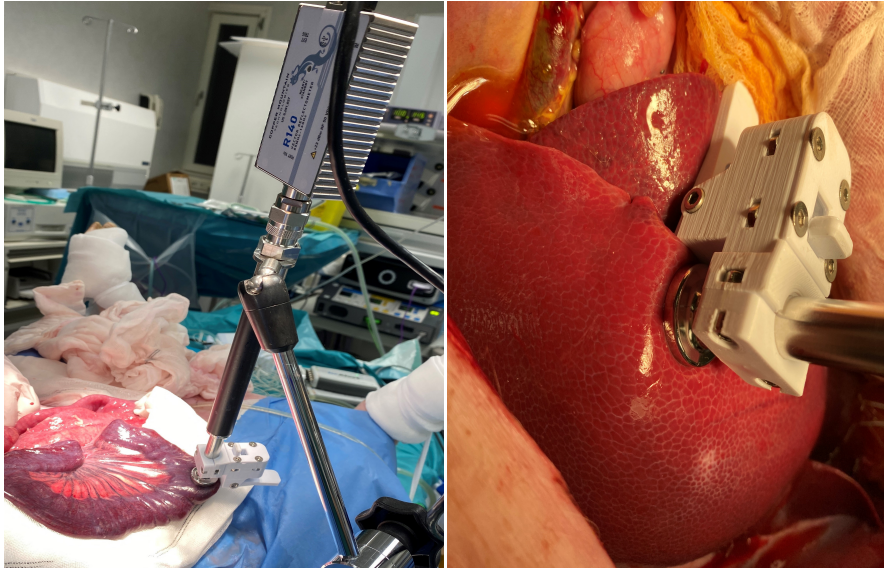
(a) Measurements on the intestine.　　(b) Measurements on the liver.

Figure 2.7: Experimental setup for permittivity measurements on the small intestine and the liver in a pig model in vivo.

movements were efficiently minimized with the rigid support of the stand. Prior to each measurement, both the probe tip and the tissue were gently wiped with a sterile cloth to avoid body fluid oozing under the probe contact area and any possible contamination.

2.2.5　Data modelling and analysis

A successful application of the bioimpedance technique does not only rely on accurate measurements but also correct and effective analysis methods to provide us with interpretable information about the biological material under investigation. Bioimpedance data modelling can reduce the amount of data to interpret, and can help us to understand the underlying mechanisms, leading to a simpler characterization of tissue properties and interpretation of data. In addition, by estimating the model parameters, we can more easily perform statistical and mathematical analysis compared with analysing the whole impedance spectra.

2.2.5.1　Cole model (Paper III)

In 1940, Cole [20] introduced an empirical mathematical model that can be used to fit experimentally obtained electrical impedance data. The Cole model

(Equation (2.6)) is based on four parameters R_0, R_∞, α and τ:

$$Z(\omega) = R_\infty + \frac{R_0 - R_\infty}{1 + (j\omega\tau)^\alpha} \qquad (2.6)$$

where R_0 and R_∞ are the impedance at very low and very high frequencies, respectively. τ is the time constant and α is a dimensionless shape parameter that accounts for non-ideal capacitor behavior, which takes values between 0 and 1. If $\alpha = 0$, the model can be realized by an ideal resistor. If $\alpha = 1$, the model can be realized by two ideal resistors and one ideal capacitor [46]. The advantage of this parameter is that it does not depend on the geometry of the tissue sample (as long as the measured volume is constant over the measured frequency range) [46]. It can be interpreted as a measure of the distribution of relaxation times. There are also other possible interpretations of this parameter as described in [46]. This Cole model is a relaxation model for the typical dispersion regions found in biological tissue.

Further, the Cole equation can be parameterized into its real (resistance (R)) (Equation (2.7)) and imaginary (reactance (X)) (Equation (2.8)) component as a function of the angular frequency $\omega = 2\pi f$ by using the relationship $j^\alpha = \cos(\frac{\alpha\pi}{2}) + j\sin(\frac{\alpha\pi}{2})$.

$$R(\omega) = R_\infty + \frac{(R_0 - R_\infty)(1 + (\omega\tau)^\alpha \cos(\frac{\alpha\pi}{2}))}{1 + 2(\omega\tau)^\alpha \cos(\frac{\alpha\pi}{2}) + (\omega\tau)^{2\alpha}} \qquad (2.7)$$

$$X(\omega) = -j\frac{(R_0 - R_\infty)(\omega\tau)^\alpha \sin(\frac{\alpha\pi}{2})}{1 + 2(\omega\tau)^\alpha \cos(\frac{\alpha\pi}{2}) + (\omega\tau)^{2\alpha}} \qquad (2.8)$$

The Cole equation is a complex non-linear function of frequency that can be represented in the complex plane, with resistance (R) on the x-axis and reactance ($-X$) on the y-axis. The Cole plot is a semi-circular ark with the center depressed under the x-axis. The most common practice when fitting the measured impedance to a Cole equation is to use both real and imaginary parts simultaneously [144].

However, calculating the parameters of the best-fit model to the measured impedance spectrum is often a non-trivial problem due to several factors. The measured impedance always includes noise which can be random from one measurement to another. Measurement techniques, ranges, and electrodes used in various studies are often different with varying accuracy, current density distribution, and signal-to-noise ratio. The parameter estimation process is a non-linear frequency-dependent problem which makes the fitting procedure more challenging [75].

In 1999, Kun et al. [75] proposed an iterative least-square algorithm to estimate the Cole parameters based on the a priori knowledge that the impedance data represents a locus in the complex plane. The locus is determined by the Cole parameters. As the measured impedance data points should lie on the locus, approximating the data points with a minor arc of a circle with center (x_0, y_0) and radius r_0 enables us to calculate the parameters. It is possible to estimate the value of the center and radius of that circle using Equation (2.9).

$$F(x_0, y_0, r_0) = \sum_{i=1}^{N} \left[\sqrt{(x_i - x_0)^2 + (y_i - y_0)^2} - r_0 \right]^2 \tag{2.9}$$

$F(x_0, y_0, r_0)$ is an error function of parameters x_0, y_0, and r_0. The parameters are determined by minimizing the square error iteratively, such that the error function (Equation (2.9)) converges to the absolute minimum. N is the number of data points, x_i is the current point value of resistance and y_i is the current point value of reactance. Thereafter, the parameters R_0 (Equation (2.10)), R_∞ (Equation (2.11)) and α (Equation (2.12)) can be calculated analytically by:

$$R_0 = x_0 + \sqrt{r_0^2 - y_0^2} \tag{2.10}$$

$$R_\infty = x_0 - \sqrt{r_0^2 - y_0^2} \tag{2.11}$$

$$\alpha = 1 - \frac{2}{\pi} \arcsin \left(\frac{|y_0|}{r_0} \right) \tag{2.12}$$

2.2.5.2 Cole-Cole model (Papers I and IV)

In 1941, the Cole brothers introduced a model which is known as the Cole-Cole model [20]. This is a generalization to the Debye relaxation model, which accounts for the distribution of dielectric relaxation times, especially for the polar dielectric substance under measurement. The empirical fitting parameter is called α [26], and permittivity is the dependent variable [46]. The Cole-Cole equation can be expressed as Equation (2.13):

$$\epsilon^*(\omega) = \epsilon_\infty + \frac{\Delta\epsilon}{1 + (j\omega\tau)^{1-\alpha}} = \epsilon_\infty + \frac{\epsilon_s - \epsilon_\infty}{1 + (j\omega\tau)^{1-\alpha}} \tag{2.13}$$

where $\epsilon^*(\omega)$ is the complex permittivity as a function of angular frequency (ω) and $\Delta\epsilon$ is the relaxation strength. The relaxation strength is proportional to the area under the dielectric loss peak. The empirical exponent parameter α has the effect of broadening the dispersion, allowing the model to describe different spectral shapes. The α parameter range is between 0 and 1.

The permittivity data acquired from the measurements made on the small intestine and the liver were fitted to a double Cole-Cole equation (Equation (2.14)), to take account of two different relaxation processes. One part of the equation was used to model the contribution from molecules that are larger than the water molecules (process 1), and the other was used to model the contribution from the water molecules (process 2).

$$\epsilon^*(\omega) = \epsilon_\infty + \frac{\Delta\epsilon_1}{1 + (j\omega\tau_1)^{1-\alpha_1}} + \frac{\Delta\epsilon_2}{1 + (j\omega\tau_2)^{1-\alpha_2}} \tag{2.14}$$

Where $\Delta\epsilon_1 = \epsilon_s - \epsilon_1$ and $\Delta\epsilon_2 = \epsilon_1 - \epsilon_\infty$ is the relaxation strength for process 1 and 2, respectively.

As with the Cole equation, the double Cole-Cole equation can also be decomposed into its real (dielectric constant (ϵ')) and imaginary (dielectric loss (ϵ'')) component as a function of the angular frequency ω by using the relationship $j^{(1-\alpha)} = \sin(\frac{\alpha\pi}{2}) + j\cos(\frac{\alpha\pi}{2})$.

$$
\begin{aligned}
\epsilon'(\omega) =& \epsilon_\infty + \frac{\Delta\epsilon_1[1 + (\omega\tau_1)^{1-\alpha_1}\sin(\frac{\alpha_1\tau_1}{2})]}{1 + 2(\omega\tau_1)^{1-\alpha_1}\sin(\frac{\alpha_1\tau_1}{2}) + (\omega\tau_1)^{2(1-\alpha_1)}} \\
&+ \frac{\Delta\epsilon_2[1 + (\omega\tau_2^{1-\alpha_2}\sin(\frac{\alpha_2\tau_2}{2})]}{1 + 2(\omega\tau_2)^{1-\alpha_2}\sin(\frac{\alpha_2\tau_2}{2}) + (\omega\tau_2)^{2(1-\alpha_2)}}
\end{aligned}
\tag{2.15}
$$

$$
\begin{aligned}
\epsilon''(\omega) =& \frac{\Delta\epsilon_1(\omega\tau_1)^{1-\alpha_1}\cos(\frac{\alpha_1\tau_1}{2})}{1 + 2(\omega\tau_1)^{1-\alpha_1}\sin(\frac{\alpha_1\tau_1}{2}) + (\omega\tau_1)^{2(1-\alpha_1)}} \\
&+ \frac{\Delta\epsilon_2(\omega\tau_2)^{1-\alpha_2}\cos(\frac{\alpha_2\tau_2}{2})}{1 + 2(\omega\tau_2)^{1-\alpha_2}\sin(\frac{\alpha_2\tau_2}{2}) + (\omega\tau_2)^{2(1-\alpha_2)}}
\end{aligned}
\tag{2.16}
$$

In this thesis, the dielectric constant and dielectric loss data were fitted separately to the parameterized double Cole-Cole equation (Equation (2.15) and (2.16)) using the non-linear least-square curve fitting method in Python.

2.2.5.3 The P_y value (Paper III)

Cole parameters can be estimated by fitting the experimental data to the Cole Equation (2.6). The acquired Cole parameters can further be used to calculate the P_y value, which can be linked to the cell membrane behavior (β-dispersion) and is sensitive to membrane integrity. According to Pliquett et al. [103], the P_y value can be calculated using Equation (2.17):

$$
P_y = \frac{R_0 - R_\infty}{R_0} \times 100\%
\tag{2.17}
$$

R_0 and R_∞ are estimated by fitting the measured data to the Cole equation (Equation (2.6)). The R_0 is related to the extracellular water since the low-frequency current is not able to pass through the cell membrane. The R_∞ can be used to estimate the intracellular water as high-frequency current passes through the cell membranes [46]. The P_y value is chosen due to its link with cell membrane behavior, which is an important parameter in the assessment of tissue viability. It provides us with the relative extent of a dispersion and can equally well be used for the dispersion of other parameters such as permittivity.

2.3 Visible and near-infrared diffuse reflectance spectroscopy measurements (Paper V)

Visible and Near-Infrared (VIS-NIR) diffuse reflectance spectroscopy uses light to determine the reflectance properties of the material under investigation. Different types of molecules react to visible and near-infrared light differently, so when measuring on tissue, it is possible to investigate changes both in the

micro-structure/composition as well as changes in the concentration of different molecules.

2.3.1 Instrumentation setup

The VIS-NIR measurements were performed using a handheld USB 2000+VIS-NIR (USB2+H00178) spectrometer from Ocean Insight (Orlando, FL, USA). It operates in reflectance mode in the wavelength range 475–1100 nm, with a 25 μm slit for an optical resolution of 1.5 nm (full width at half maximum). The spectrometer was connected to a QP600-2-VIS-NIR fiber (Ocean Insight, Orlando, FL, USA) with a wavelength range of 400–2100 nm and a TC-DR probe (Ocean Optics, USA), which is a 45° diffuse reflectance probe with an integrated tungsten halogen light source (6 watts). The TC-DR probe has a 40 mm stand-off block ensuring consistent focal length.
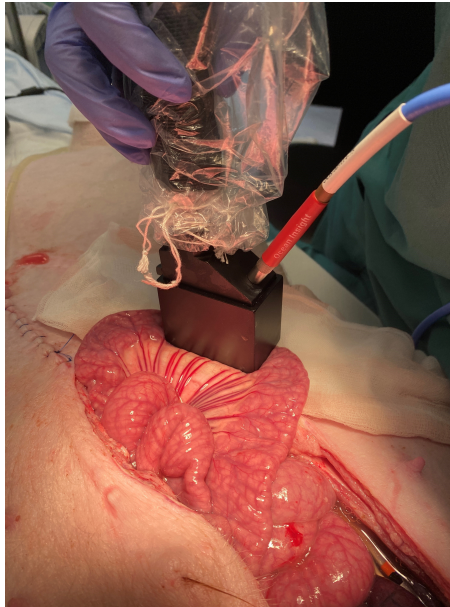
Figure 2.8: Experimental setup for VIS-NIR measurements on the porcine small intestine.

During the experiment, three measurements were taken at three different locations (chosen randomly) on each segment and the data from these measurements were averaged. This was performed in order to reduce the error in the measured value and obtain representative spectra. As this method utilizes light, it is important to have a controlled light source and eliminate ambient room light. Therefore, a diffuse reflectance probe (DR probe) with a measurement site area of 24 mm × 47 mm was used. This probe also ensures that only one light source is used (light from the surrounding environment is blocked

from the measurement site). This allows for high reproducibility of data. The experimental setup is shown in Figure 2.8.

2.3.2 Spectroscopy data analysis

Standard normal variate (SNV), Equation (2.18), was applied to all measured VIS-NIR spectroscopic data to minimize variations in the diffuse reflectance spectra induced by light scattering and the varying position of each measurement.

$$Z = \frac{X - \mu}{\sigma} \tag{2.18}$$

where Z is the standardized data, μ is the mean and σ is the standard deviation. After standardization, where we subtract the mean value and then divide it with the standard deviation, we have $\mu = 0$ and $\sigma = 1$.

A first-order derivative was applied (using Savitzky-Golay (SG) polynomial derivative filters) on the SNV-transformed data to remove the baselines. Partial least squares-discriminant analysis (PLS-DA) was chosen to classify the measured diffuse reflectance spectra from the small intestine. This algorithm is particularly suited for spectroscopic data, even when the number of wavelengths exceeds the number of samples, and where co-linearity usually exists among the predictive variables. 10-fold cross-validation was used, where each fold contained data from one pig. The data were divided according to the individual subjects, to avoid data leakage between model training and testing. This procedure supports the development of a more generalized model.

2.4 Histopathology analysis (Paper V)

To investigate the borderline between the viable and non-viable intestinal segments, we collected full-thickness biopsies for histopathological analysis. Specimens from the intestines were fixed overnight in buffered 10% formalin, dehydrated in a graded series of ethanol, and embedded in paraffin. 4-μm-thick sections were cut and then stained with haematoxylin and eosin (H&E). Stained sections were examined by two pathologists using light microscopy.

There is no standard histological classification method for IRI in the small intestine [104]. There have been several proposed approaches, for instance, the Swerdlow [124] and Chiu/Park [19, 99] grading systems. We chose the Swerdlow approach in this thesis, as its grading has a higher resolution for pathological changes in the intestinal wall, while Chiu/Park focuses mainly on the mucosa.

2.5 Image acquisition and analysis (Paper II)

Images of the small intestine were acquired using a handheld digital camera (AM7013MZT from Dino-lite), integrated with a controlled light source (8 white LED). Image resolution is 2592×1944 pixels and the camera has a magnification

power of 10-200×, allowing for a flexible zoom function. The built-in adjustable polarizer can significantly reduce glare from the wet intestinal surface.

Image analysis is the process of extracting useful information from images, including detecting shapes, counting objects, removing noise, and calculating statistics. Descriptive statistics can be used to investigate different image properties. Among various image descriptive parameters, entropy and contrast were chosen to describe the statistical changes during ischemia and reperfusion as a function of time.

2.6 Machine learning

For the past decade, Machine learning (ML) has emerged in both daily life and the academic world as an application. ML refers to algorithms that are designed to investigate associations and patterns from a large dataset to make decisions without explicit instructions. There are different types of ML, generally divided into supervised learning, unsupervised learning, semi-supervised learning, and reinforcement learning algorithms. Supervised learning will be focused on in this thesis. In supervised learning, the algorithms can be divided into two types, one is regression tasks and another is classification tasks. We performed classification where the output variables were organized into two or more groups, as our objective was to classify both viable and non-viable conditions and different injury levels of the small intestine. The classification algorithm aims to analyse patterns using input data and output labels. After the model is trained then the patterns learnt from the input data are used to predict the correct class. The following subsections will describe the different models used in this thesis.

2.6.1 Long short-term memory artificial recurrent neural network (Paper I)

Repeated permittivity measurements produce a series of datasets consisting of different dielectric parameters as a function of frequency. ML is a powerful tool to learn the patterns of associations between the parameters and between the frequencies, from large sets of complex non-linearly dependent permittivity data.

An artificial neural network (ANN) is a subset of supervised learning which is designed based on the animal brain. ANN consists of layers with connected nodes. The nodes, which are called artificial neurons, are connected to each other like the neurons in the brain, which are connected through synapses to transmit signals to each other. In this way, information can be passed layer by layer and processed. The first and simplest type of ANN is a feed-forward neural network, where the information moves only forward (Figure 2.9).

With respect to permittivity data, recurrent neural networks (RNN) are of interest, due to their ability to learn temporal patterns and non-linear dependencies in multivariate frequency-series data. An RNN is a class of ANN, which can learn temporal dynamic patterns in sequential data. They allow information from prior inputs to have an effect on the current input and output,
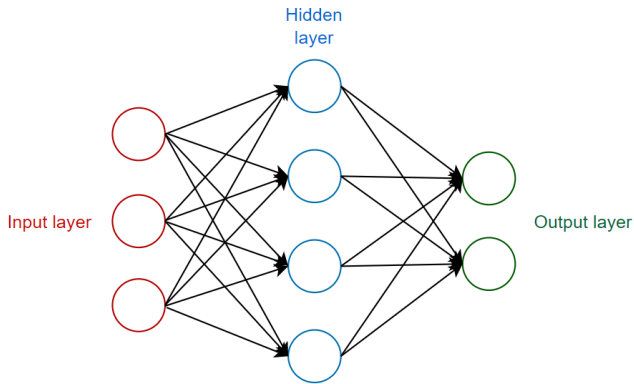
Figure 2.9: Feed-forward neural network architecture.
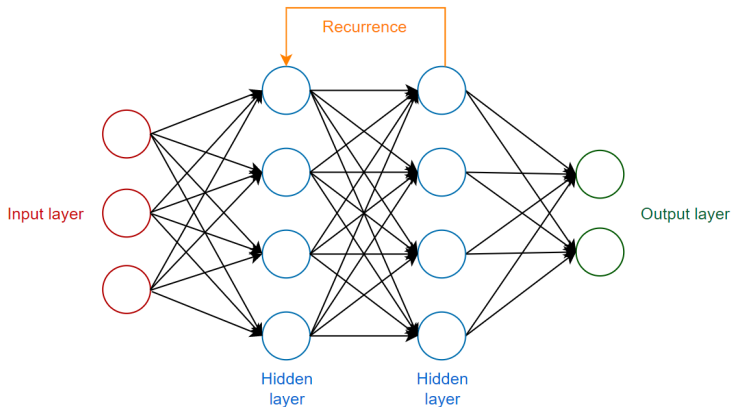
Figure 2.10: Recurrent neural network architecture.

thus providing a memory capability. However, the basic RNN network suffers from the vanishing gradients problem [70]. The gradient of the loss function during training of the network can quickly become smaller and smaller[5]. It can become negligibly small for longer input sequences (vanishing gradient) so it struggles to learn possible dependencies in longer sequences. An illustration of an RNN architecture is shown in Figure 2.10. In order to deal with this problem, Sepp Hochreiter [55] introduced a new type of RNN which is called the "long short-term memory networks (LSTMs)". Compared to the traditional RNN, the LSTM network architecture is equipped with "gates", which are internal mechanisms that regulate the flow of information to better handle the longer sequences dependence (Figure 2.11). The "gates" keep important information and disregard unimportant information. In this way, the network not only

---

[5]Due to the multiplication of derivatives, depending on the activation function.
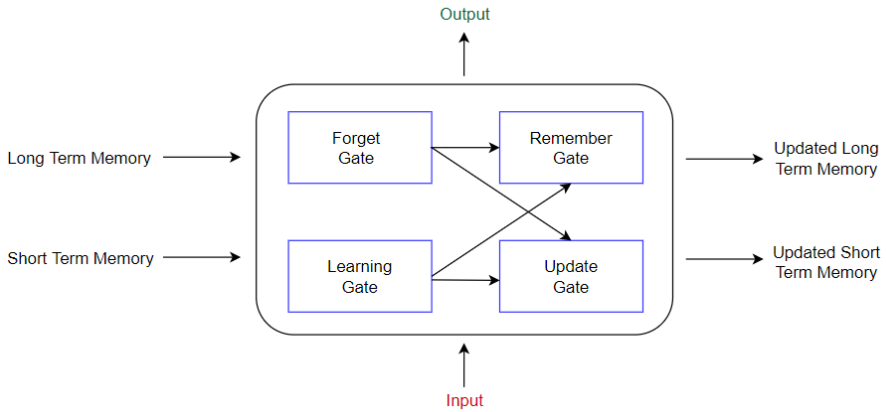
Figure 2.11: A simplified architecture of an LSTM cell. The Learning gate takes the current input and the previous short-term memory and keeps only relevant information. The forget gate takes the previous long-term memory and decides which information should be forgotten. The remember gate combines the previous short-term memory and the current input to produce an output. The update gate combines information from the previous long-term memory and the previous short-term memory to create an updated short-term memory and an output.

resolves the vanishing gradient problem but is also capable to use only the relevant information to make more accurate predictions. Conventionally, LSTM is used on time-series data. In this thesis, we have explored the idea of using LSTM to learn frequency-dependent patterns in spectroscopic data, in particular dielectric/bioimpedance spectroscopy, using three different LSTM networks; traditional LSTM, bidirectional LSTM, and residual LSTM. Details of model architectures can be found in Paper I.

2.6.2 Convolutional neural network (Paper II)

A convolutional neural network (CNN) is a class of ANN, which is inspired by and resembles some of the structures of the animal visual cortex. CNNs have been widely applied to images, as they are specifically designed to process pixel data. The learning process of a CNN can be compared to the way a child learns to understand the world. When a child sees a dog for the first time, the child does not know what a dog is. After a few times when the parents have told the child that the specific animal that the child is seeing is called a dog, the child would relate an image of a dog to the word "dog". In the same way, CNN learns how to recognize an object that it is presented with as input. The difference is that there exist only numbers in a computer's world and every image is represented by pixel numbers. Each image has three dimensions; height, width, and color channels, presented with numerical numbers. Two important
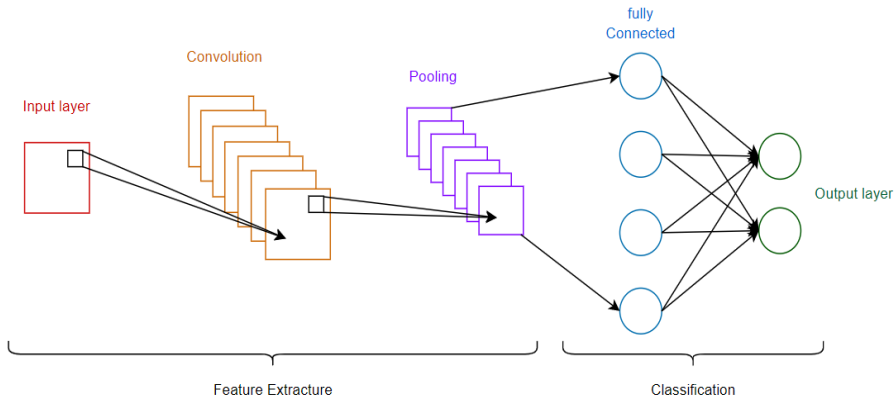
Figure 2.12: CNN architecture.

components of a CNN model are hidden layers and fully connected layers. The hidden layers are convolutional layers that consist of a filter and a kernel size, where the filter defines the size of the output and the kernel size decides the dimension of the convolution window. A convolution window is typically a window of pixels, where mathematical operations are performed on the numbers representing pixels of a part of an image. When an image enters a CNN network, the convolutional layers first extract important features and generate a feature map. The pooling layer summarises the features present in the feature maps (to reduce the dimensions of the feature maps). The output is then passed to the fully connected layers, to perform the classification by assigning a probability for the object in the image being a certain class. An illustration of a CNN architecture is shown in Figure 2.12. Further details regarding the CNN model architecture can be found in the method section of Paper II.

2.6.3 Transfer learning (Paper II)

Transfer learning is a technique where the knowledge obtained from a task is reused as the starting point for a different but similar task. A popular approach with transfer learning is to use a pre-trained model as a base model for a new task, as training a network from scratch requires vast data, time, and computational resources. The pre-trained model learns general features from large datasets, which can be tailored to another different dataset with some similarities but for a different problem. In this way, a lot of time and resources can be saved related to data collection and training time. There is a large amount of publicly available pre-trained models that have been trained on large and challenging datasets, that can be utilized as a starting point for a new task we seek to solve. The base model needs to be tuned to suit the new dataset, and the tuning may involve including a part of the pre-trained model and some additional layers to make the model more suitable for the new task. A common practice involves using the general features learnt in the pre-trained model and then learning

specific features of the new dataset. Additional layers can be added, combined with fine-tuning, to make the model more task-specific.

Transfer learning is a potential shortcut for getting better performance while saving resources. There are generally three possible benefits with the use of transfer learning; model performance is higher initially during training, higher rate of improvement during training, and higher converged performance [95]. With a limited and time-consuming collection of data, which often is the case with medical data collected from patients or animals, transfer learning can be an advantage in developing high-performance models. The pre-trained model ResNet50 [50] was chosen in this thesis due to its outstanding ability to extract features from images and the ability to generalize itself based on the dataset given.

2.6.4 Bayesian neural network (Paper II)

A Bayesian neural network (BNN) is a type of probabilistic model that refers to extending the standard neural networks with a posterior inference. BNNs are built from probability distributions and use the laws of probability in their prediction. A BNN architecture is known to be robust to over-fitting, by accounting for all possible explanations of the data (all configurations of the parameters) when making predictions, instead of only accounting for one set of parameters like classical neural networks. Bayes' rule tells us the conditional probability of a hypothesis, given the observations in our data, and helps us to analyse the model prediction uncertainty [39]. Compared to traditional neural networks, the weights and biases in the network have a probability distribution attached, instead of a single deterministic value representing the weight and bias.

BNN should be used in cases where uncertainty is important, for example with decision-making systems in clinical use. When performing classification tasks on images, several predictions are made on each of the images, instead of only once. The average model prediction will give the relative probability of each class, which is considered a measure of uncertainty [64]. For low-quality, noisy images or images that are completely different from the rest, the output will have a more "uniform-like" distribution. This is interpreted as high uncertainty as the model classifies the same image to a different class each time. High-quality images combined with a well-trained model will give us the same prediction of the true class each time, as the model tends to draw the same conclusion each time from the same image. This could be interpreted as the model being able to extract the real features which contribute positively to the correct classification.

BNN provides an approach to quantify uncertainty in ML, and the predicted uncertainty is considered more consistent with the observed errors compared to traditional neural networks [64]. BNN allows us to account for both the aleatoric uncertainty[6] and epistemic uncertainty[7] [64, 71]. BNNs allow us to distinguish between the two uncertainties and thus be able to identify which uncertainties

---

[6]Statistical uncertainty due to randomness in observations.
[7]Systematic uncertainty due to a lack of knowledge or data.

have the potential of being reduced. Further details regarding the BNN model can be found in the method section of Paper II.

2.6.5 Explainable artificial intelligence (Papers I and II)

Explainable artificial intelligence (XAI) aims to explain the prediction results from an ML model by associating output with features in the input. The results of ML can be difficult to explain, even for the designers of the ML algorithms. It is not easy to explain how the ML models derive from their input data to the output decision. ML algorithms are becoming more and more complex. In the early models, 3-4 layers were involved, but now more than 200 layers can be involved in one single model [91]. There has been an exponential growth in the number of parameters used in deep learning models, from 94 million parameters in 2018 to 1.6 trillion parameters in 2021 [2]. The results are "black-box" models where the interpretations of the relation between different variables are not very explainable [57]. This technical challenge of explaining machine learning decisions is sometimes known as the interpretability problem [131]. XAI is a method of making some of the associations between input and output visible, to make it easier to understand what is happening inside a model and thus ensure that the system is working as expected.

2.6.5.1 SHapley Additive exPlanations (SHAP) (Papers I and II)

There are several different approaches in XAI. The SHapley Additive exPlanations (SHAP) [81] is one approach that can be used to explain the output of an ML model (how the predictions are made). Shapley values from cooperative game theory are utilized in the SHAP method, where an importance value "Shapley value" is assigned to each feature (input variable) for a particular prediction. For image classification, a Shapley value is assigned to each of the pixels. The values explain the change in the expected model prediction conditioned on a given feature [81]. A positive Shapley value indicates a positive contribution to the correct classification, and a negative Shapley value indicates a negative contribution to the correct classification. From the distribution of Shapley values, we can obtain an understanding of how different frequencies of dielectric measurements or different areas of an image contributes to the classification result. The SHAP method was applied to both LSTM and CNN models in Papers I and II.

Chapter 3

Summary of Papers

3.1 Paper I (Small intestinal viability assessment using dielectric relaxation spectroscopy and deep learning)

In this study, permittivity data from the porcine intestine was used to analyze the characteristics of various degrees of IRI. LSTM-RNNs were used to classify viable and non-viable segments based on frequency-dependent dielectric properties of the intestinal tissue. The main results are:

1. Permittivity measurements with the VNA and the OCP are sensitive to IRI-related changes in the small intestine in vivo.

2. The overall dielectric constant and conductivity are higher for data from the reperfusion phase compared to the control phase and the ischemic phase.

3. There are statistically significant changes in the dielectric constant parameter of the intestine between tissue states, at 6.25 GHz.

4. The relative changes in the dielectric constant and conductivity may be associated with IRI-related changes in the concentration of some biomarkers (lactate, glycerol, etc.).

5. Employing LSTM-RNN and CNN models on repeated permittivity measurements during both ischemic and reperfusion phases may allow for better prediction of intestinal viability. Using only half of the frequency spectra in the ML model while keeping good prediction performance enables us to simplify the instrumental requirements for further pre-clinical studies.

6. LSTM-RNN is a promising tool for the classification of non-linearly dependent frequency series of sequential spectroscopic data.

7. Utilizing the SHAP method allows us to explore the important frequencies in the dielectric properties for the detection of IRI-related changes.

3.2 Paper II (Automatic Prediction of Ischemia-Reperfusion Injury of Small Intestine Using Convolutional Neural Networks: A Pilot Study)

In this pilot study, we explored the feasibility of using ML models on images of the intestine with a digital microscope camera, to assess small intestinal viability. The main results are:

1. Microscopic images taken from the small intestinal surface hold information related to IRI.

2. The statistical parameters entropy and contrast showed differences between the various tissue conditions, allowing for rough separation between the cases.

3. ML can be used as a semi-automatic method to predict the tissue IRI condition based on microscopic images of the tissue.

4. BNN provides uncertainty measurements of the model predictions, where we gain information about how likely the model is, given the data that have been used to train the model.

5. The SHAP method can be used to explore which areas/pixels on an image the model considers as important features and contributes positively to the correct prediction. This may enable us to discover new associations and causalities for observations in the future.

3.3 Paper III (Assessing ischemic injury in human intestine ex vivo with electrical impedance spectroscopy)

In this study, electrical impedance measurements were performed to investigate the changes induced by ischemia in the human intestine. The main results are:

1. The two-electrode setup with trans-intestinal measurements can detect changes related to ischemic injury in the human small intestine.

2. The impedance value first decreased after one hour of ischemia, then increased for the following two hours, before decreasing irreversibly.

3. The P_y parameter could be used to assess human small intestinal viability. The time development of the P_y parameter measured on ex vivo human intestine associated with the histological results.

4. The human small intestinal tissue is most likely viable until the maximum P_y value is reached.

3.4 Paper IV (Utilization of dielectric properties for assessment of liver ischemia-reperfusion injury in vivo and during machine perfusion)

In this study, the dielectric properties of the porcine liver were measured, both during in vivo and machine perfusion phases. The main results are:

1. Dielectric relaxation spectroscopy can be used as an objective method to evaluate levels of IRI in livers, both in vivo and during machine perfusion. The dielectric conductivity parameter can be used to differentiate between

healthy livers, biliary injured livers, and hepatic injured livers, during machine perfusion.

2. During the in vivo monitoring phase, statistically significant changes in the conductivity parameter were found between the healthy liver and the liver where the hepatic artery was occluded, while no apparent visual changes could be observed on the liver surface.

3. Following the first hour of NMP, the conductivity spectrum as a function of frequency was similar for the healthy livers (CON), biliary (AHEP), and hepatic injured (SCS) livers. Following three hours of NMP, the conductivity of the most injured liver group (SCS) stands out compared to the other two groups. After four hours of NMP, there were clear separations in the spectral conductivity between the three groups.

4. The proposed non-destructive water content quantification method based on dielectric properties may enable us to gain information regarding edematous changes in the livers.

3.5 Paper V (Assessment of intestinal ischemia-reperfusion injury using diffuse VIS-NIR spectroscopy and histology)

In this study, we investigated the feasibility of using VIS-NIR spectroscopy to assess various degrees of IRI in the porcine small intestine. PLS-DA models were used on the reflectance data to more accurately differentiate both the different perfusion phases as well as the viability of the small intestine. The main results are:

1. Accurate prediction of porcine small intestinal tissue viability can be made using diffuse VIS-NIR spectroscopy together with PLS-DA modelling.

2. The borderline between viable and non-viable small intestinal tissue appears between 2–3 hours of ischemic time based on histological analysis. The possible upper limit for viability in a porcine SMO model is ≤ 2 hours of ischemia.

3. The most important wavelength region for investigating IRI is between 500–600 nm due to contributions from oxyhemoglobin and deoxyhemoglobin.

4. The PLS-DA models were able to distinguish between normal, ischemic, and reperfused segments with an average accuracy of 99.2%, and classification between viable and non-viable segments achieved an average accuracy of 96.0% using 10-fold cross-validation.

Chapter 4

Discussion

This chapter provides a general discussion of the techniques and main findings presented in this thesis. The first two sections "Validity and advantages" and "Limitations" are structured based on the different methods used, where the instruments, the experimental setups, and the results are discussed. The last section "Implications of the work" puts the work from the respective papers into a wider context and addresses the significance of the work related to applications.

4.1 Validity and advantages

4.1.1 Bioimpedance and permittivity measurements

By using bioimpedance and permittivity measurements, we can achieve a higher prediction accuracy than existing standard clinical methods. Performing a single measurement and analyzing the frequency-dependent spectrum with the corresponding impedance data or dielectric parameters (dielectric constant, dielectric loss, or conductivity), during either ischemia or reperfusion phase, gives us an objective estimation of tissue condition. Both the EIS and DRS methods are non-destructive, but they require tissue contact. The potential benefits are more accurate decisions on resection margins and a reduction in the need for second-look surgeries. This can contribute to fewer complications and less surgical stress for the patients.

Classification of permittivity data is a complex task, as the raw data overlap and have similar characteristics at certain frequencies among control, ischemia, and reperfusion phases. The relative changes of the dielectric parameters due to IRI appeared to be large and allowed for easy discrimination of the control cases from the ischemia or the reperfusion cases. However, distinguishing the viable intestinal segments from the non-viable ones was nevertheless challenging, as these data overlapped and had periods of similar characteristics. Therefore, we utilized LSTM and CNN models to classify viable and non-viable segments. LSTM is powerful in capturing temporal associations that are difficult to be detected with traditional analysis methods. This feature of LSTM is important because the relationship between the biological process and the dielectric change is often non-linear, and the captured associations between the frequency-corresponding permittivity data helped to discriminate the viability of the small intestine.

With respect to the interpretability of the permittivity data, we mainly measure the dipolar molecules in the intestinal tissue. Lactate, glycerol, glucose, and pyruvate, measurable by microdialysis, are dipole molecules found in the small intestine that changes in concentration as a function of ischemic exposure. Lactate and glycerol were reported to be the most relevant to IRI [118]. Intraluminal concentrations of lactate and glycerol were measured

by Strand-Amundsen et al. during ischemia-reperfusion in an SMO model in pigs [118]. Intraluminal measurements are more stable compared to the superficial placement of the microdialysis catheter and were therefore chosen. They reported that during the first hours after the initiation of ischemia, intraluminal lactate increases significantly (due to the death of the intestinal villus resulting in lactate leakage to the lumen). Intraluminal lactate in the ischemic intestine peaks around 6-8 hours of ischemia, while a decreasing trend was observed during reperfusion. The glycerol levels in the lumen first increased during ischemia and then decreased upon the onset of reperfusion, ending at a similar glycerol level as the control intestine after 6-7 hours following reperfusion. In order to be able to link the permittivity data to the specific molecules, we need to perform separate measurements on the individual molecules with different concentrations in a known medium, to study the changes in the permittivity spectra.

With respect to bioimpedance measurements, there are several advantages compared with permittivity measurements. Bioimpedance measurements are simpler to perform and do not require a complex and time-consuming calibration as with the permittivity measurements. Bioimpedance technology is low-cost and has the possibility to be facilitated with a small handheld probe, allowing for usage during laparoscopy where minimally invasive procedures are preferred. Regarding the permittivity measurement setup, the OCP is small in size and the VNA has the possibility to be miniaturized. However, the OCP requires specialized dielectric bead materials (such as Eccostock), while bioimpedance measurements do not require such materials. Moreover, with a miniaturized VNA, controlling the high-frequency permittivity measurement signals without cross-talk and noise can be challenging. With respect to measurement time, bioimpedance measurement takes a few seconds, and permittivity measurement takes around a second. Depending on the available clinical time frame, several measurements can be performed intraoperatively without substantially increasing the duration of the surgery, as both methods are fast.

Using trans-intestinal measurements to assess intestinal viability has been investigated by Strand-Amundsen et al. [117, 119, 120, 122] using a 2-electrode setup. The passive electrical properties of the small intestine differ between perfused and ischemic segments, indicating that trans-intestinal bioimpedance measurement is likely useful for monitoring the small intestinal condition. To evaluate the translational value of the results from Strand-Amundsen et al. [120], we studied the electrical properties of the human small intestine ex vivo in Paper III. The time development of the impedance was found to be different for the first two hours following the onset of ischemia/resection in the human intestinal segment, compared with the ex vivo experiment using porcine small intestine by Strand-Amundsen et al. [120]. The observed differences could be attributed to the temperature variations as well as small physical differences between the human and the porcine intestines. The temperature was lower during the first measurement compared to the rest of the measurements. As the intestinal sample was exposed to air for several minutes after the resection before we performed our first measurement. Moreover, the human jejunum samples were a bit thicker, with some more mesenteric fat than the samples

from the 50-kg porcine model. Fat tissues have different current conducting abilities compared with muscle tissues, which may have partially contributed to the observed differences [66, 145].

The evaluation of marginal liver grafts relies on a comprehensive assessment of liver functions. However, the standard methods of evaluation heavily depend on unreliable visual inspection and donor history. With the aim of improving the accuracy of liver evaluation, we are the first to report the use of DRS to monitor changes in dielectric properties during machine perfusion. The dielectric conductivity in all three groups changed significantly (compared to the in vivo control data) after one hour of NMP, possibly because of the initial reaction from the altered perfusion phase. Clear separations in dielectric conductivity were observed among the three groups after four hours of NMP, indicating that IRI-related pathological changes can be reflected in the dielectric parameters.

The intervention groups[1] were established with the aim of evaluating distinct models with different levels of liver injury. The hepatic artery occlusion model was used to create isolated arterial ischemia. This condition is hardly present in livers considered for transplantation. However, the hepatic artery model is relevant to create injury similar to that caused by thrombosis[2] of the hepatic artery, a serious complication following liver transplantation. Thus, we utilized a model with a reproducible extent of biliary ischemic injury using the hepatic artery occlusion model. The global hepatic injury model was selected to simulate a generally injured liver, as static cold storage preservation leads to liver graft injury which is difficult to achieve by other methods.

Although the three-phase sequence of DHOPE-COR-NMP with gradual rewarming has rarely been performed in clinical practice, the DHOPE-COR-NMP protocol of machine perfusion is an established approach to NMP developed by the Groningen group [80, 132, 133]. Porte R. et al. have stated that the COR phase links DHOPE and NMP together, which helps to avoid sudden temperature shifts that may cause additional injuries to an already compromised donor liver. The perfusion machine[3] enabled us to run all three phases. Based on the mentioned earlier studies, this protocol was used with the aim to reduce IRI at the start of NMP.

4.1.2 Diffuse reflectance measurements and PLS-DA model

Diffuse reflectance spectroscopy is a non-invasive and easy-to-use method. It is based on the fact that different substances reflect light differently. When the composition of substances in the tissue changes during IRI, the reflection of light at certain wavelengths also changes accordingly.

As a strength compared to the previous studies, two approaches were utilized to obtain more representative and trustworthy spectra from the VIS-NIR spectrometer. Firstly, our probe was designed for an area scan instead of

---

[1]Hepatic artery occlusion model with biliary injury (AHEP) and global hepatic injury model (SCS).

[2]Blood clots block veins or arteries, which block the blood supply.

[3]Liver Assist perfusion machine (XVIVO-Abdominal, Groningen, The Netherlands).

a "single point" measurement. This allowed us to cover a large area (11.28 cm^2) on the three different locations of each intestinal segment, and the data from the three measurements were averaged to avoid the potential errors and typically large variations in "single point" measurement. Secondly, we ensured that only one light source was used[4] by using the diffuse reflectance probe (TC-DR probe). The combination of these approaches resulted in more accurate and repeatable spectra compared with "single point" measurements in ambient light. This also avoided the effects caused by the heterogeneities of the small intestine itself and IRI.

Comparable investigations have been reported by Sowa et al. [115], where they employed diffuse reflectance spectroscopy in a porcine model in the wavelength range of 500–1100 nm with "single point" measurements. They reported the reflectance spectra of control, ischemic, and reperfused intestinal segments. Furthermore, they developed a PLS-DA model to differentiate the control from the ischemic segments and reported an accuracy of 89.3%. They used the same model to classify ischemic from reperfused segments and an accuracy of 92.5% was reported. With our data, using diffuse reflectance spectra in the wavelength range of 500–1000 nm, we classified the normal, ischemic, and reperfused segments and achieved an average accuracy of 99.2%. When distinguishing between viable and non-viable segments we achieved an average accuracy of 96.0%.

More recently, Karakas et al. [69] investigated the use of diffuse reflectance spectroscopy in a rat model and reported the absorption spectra in the wavelength range of 450–750 nm. They compared the ratio of the absorption between wavelengths at 560 nm and 577 nm to the histopathological grading with an 8-point Park/Chiu score. We were not able to reproduce the associations between the ratio value and the histopathological grading. The reason may be that they have used an optical fiber probe where the probe ferrule diameter is approximately 6 mm, covering a considerably smaller area compared with the probe used in our work. Regarding the measurement setup, the ambient room light was blocked from entering the measurement site in this work, while they performed the measurements with ambient room lighting. In addition, a rat model was used in their study, while we performed our measurements in a porcine model.

4.1.3 Microscopic images and CNN models

Using CNN models combined with microscopic images acquired from the small intestinal surface, we were able to achieve high accuracy in the prediction of different injury conditions. This method is non-invasive and fast, and performing the measurements does not require specialized training. During microscopic imaging, visible light penetrates the semi-transparent intestinal layers, revealing information not only about the surface but also from the deeper layers, such as subserosa, muscularis, and blood vessels. Detailed micro information from the small intestine can be challenging for the human eyes to perceive and for the brain to interpret and remember.

---

[4]Light from the surrounding environment was blocked from the measurement site.

Using CNN models, we were able to classify different degrees of IRI in the small intestine. The SHAP method, within the XAI category, revealed both the positive and the negative contributions to the classification. This helps us to understand which areas of the small intestine the model has used to make its classification. For example, one could speculate that blood vessels narrowing/widening and small blood spots appearing in different layers of the small intestine could be indications of different injury conditions. Thus, areas that the XAI method highlights could enable further investigation of the possible important features and changes which are not yet known.

4.1.4 Histology

Histological analysis has been extensively used to study IRI. However, the lack of consensus on the grading system has long been a challenge related to the use of histology in the assessment of IRI in the small intestine. As a consequence, it is difficult to compare the histological results across different studies [104]. Most published works have used their own systems and reported their observations as histological grading scores and/or as morphological observations [104], but there are only a few that explicitly state the viability of the small intestine.

Irreversible ischemia-reperfusion injury of the jejunum has been reported to occur after 6.5 hours of ischemia followed by reperfusion (once the crypts had been damaged completely) [16]. Later, Chen et al. [18] concluded that ileum segments can tolerate ischemia for less than 2 hours, based on a previous study that reported 2 hours as a viability limit. Beltran et al. [7] reported that intestinal segments subjected to reperfusion after 2 hours of ischemia did not fully recover in porcine models, with superior mesenteric artery occlusion evaluated by bioimpedance measurements. Most recently, Strand-Amundsen et al. [118] reported that the intestinal tissue is probably irreversibly injured when exposed to warm ischemia for ≥ 4 hours and then reperfused. They reported a total loss of crypt epithelium and an extensive shrinkage/loss of myocytes in the outer layer of the muscularis propria in the irreversibly injured intestinal segments. Three hours of ischemia was reported to be the apparent time limit for intestinal viability in porcine SMO models. Our work suggests that the time threshold for non-viable intestine tissue appears to be ≤ 2 hours of ischemia followed by reperfusion in porcine SMO models. We observed total mucosal necrosis and loss of the basal parts of glands after 3 hours of ischemia and 5 hours of reperfusion, and this was histopathologically determined non-viable by two independent pathologists (Paper V). The P_y value from the bioimpedance measurements on human intestinal tissue reached its maximum between 2–4 hours, which is consistent with the viability limit observed for the porcine intestines.

4.2 Limitations

A common limitation related to all the sensor techniques investigated in this thesis is the present lack of in-depth clinical validation, requiring further approval

of the clinical aspects of the sensors. Limitations regarding each technique used are discussed in the following subsections.

4.2.1 Permittivity measurements on the small intestine and the liver

We have investigated changes during ischemia and reperfusion phases in the porcine small intestine using an SMO model. Although similarities have been reported between pigs and humans, it remains unclear whether the results from a porcine model can be applied to an in vivo human model. Moreover, the SMO model investigated is only one of several ischemia-reperfusion models. SMA occlusion models or non-occlusive ischemia models etc. have not been studied in this work. Considering these models mimic slightly different ischemia mechanisms, we speculate that they will lead to differences in the measured dielectric properties during ischemia-reperfusion phases.

As we created multiple parallel ischemia-reperfusion segments in the same pig, there could be some confounding effects among different intervention segments. The adjacent segments may have been influenced by the reperfusion mechanism in the nearby segments, potentially influencing the measured permittivity data.

Regarding the measurement technique, a 3D-printed clip was used for both measurements on the small intestine and on the liver. It was used to ensure near-constant pressure between the coaxial probe and the tissue, but small variations might have occurred and thus influenced the measured permittivity data. A study conducted by Maenhout et al. [82] investigated the effect of probe-to-tissue contact pressure on dielectric measurements and observed relative changes in the real and imaginary part of the complex permittivity to be -0.31% and -0.32% per kPa based on measurements on the fresh bovine liver.

There might have been slight variations in the temperature during both experiments on the small intestine and the liver. We tried to keep a constant temperature during each measurement and ensure that the temperature was the same from one experiment to another, but we could not exclude temperature fluctuations (typically from when the tissue was exposed to air) to be a potential source of variations in the permittivity measurements. The orientation of dipolar groups is affected by thermal agitation and their dielectric properties are dependent on temperature [34]. This temperature dependence is governed by individual polarization mechanisms [33]. Generally, the permittivity measurements are affected by approximately -0.5% per degree Celsius [46]. As the temperature variations are believed to be small, we could not conclude the exact influence on the permittivity measurements from our experiments.

To the best of our knowledge, DRS has not previously been used on livers during machine perfusion. The changes in dielectric conductivity that we reported in Paper IV have not been fully understood or associated with all the biological/pathological changes in the liver tissue. Microdialysis, blood flow, bile production, and histological analysis were performed during the experiment by other researchers, the results are not yet available for comparison with our results. Therefore, we are not yet able to predict possible clinical benefits

compared with the "standard liver viability assessment" as published in the literature.

During the experiments, we noticed that the rate and degree of discoloring of the liver during NMP differed between and within different liver lobes. This could originate from variations in the physical positioning of the liver lobes on the perfusion machine, leading to variations in the degree of perfusion in different parts of the liver, which may have influenced the measured permittivity data. Moreover, the probe was placed at different positions on the livers to capture as much of the variation as possible, but we were not able to capture all the variations to represent the whole liver.

4.2.2 Bioimpedance measurements in a human intestinal model

The measured bioimpedance data from each individual intestinal segment might have been influenced by inter-patient variations, like age, weight, and medical history. With the comparable porcine models, we had full control over weight and age, but not so with the patients.

During the bioimpedance measurements, we noticed some small variations in mechanical pressure between the two electrodes. When exposed to ischemia for more than 3–4 hours, the intestinal wall gradually became thinner and softer due to dysfunction of the muscle cells. This leads to a narrower distance between the electrodes, which possibly changes the current path through the intestine and thus influences the measured bioimpedance data. Studies conducted by Ruiz-Vargas et al. [109] suggested that large variability is avoided when the exerted pressure is limited to below 20 kPa based on bioimpedance measurements on human colon tissue. As the variation of the pressure is believed to be significantly lower than 20 kPa during our experiments, the influence on the measured bioimpedance could be considered small with respect to the variations due to the altered tissue condition. Moreover, the measurement site where the electrodes were placed on the tissue might not represent the ischemic injury of the whole intestinal tissue sample as tissue injury appeared to be heterogeneous.

4.2.3 Diffuse reflectance measurements on the small intestine

VIS-NIR diffuse reflectance spectrometry measures the reflected light from the tissue. The measurement depth is only a few millimeters depending on the transparency of the small intestine at the measurement time point. Thus, we were not able to measure IRI-related pathological changes in the deeper layers of the intestine.

During the measurements, we noticed that the surface area of reperfused intestinal segments sometimes became narrower as a consequence of spasms, making it harder to cover the entire opening of the probe with the intestine.

4.2.4 Machine learning

One limitation related to the use of machine learning in this work and probably true for all machine learning works is that a finer grid with more hyperparameter choices to find the best parameters during the tuning of the models could be used. However, we had to make a compromise between the grid size and the training time needed.

In both Papers I and II, a relatively small number of porcine subjects were used considering the deep learning models employed, which may lead to limited generalization of the models. It would probably be better to divide the training dataset and the test dataset by individuals, where the test dataset contained only measurements performed on pigs other than those in the training dataset to avoid data leakage and the subsequent overestimation of model performance. This means that it can be more uncertain how the accuracy measures represent predictions on new data. It is not conclusive whether the models are transferable to the human small intestine as this is an early-stage pilot study. A larger dataset is needed, preferably from the human small intestine, to determine the clinical relevance.

The term "black box" is often associated with machine learning due to the complexity of the models. It is difficult to understand what the model does and on what basis the model makes a certain prediction. We have utilized the SHAP method within the XAI category in this work, which gave us some understanding of what foundation/information the model considers important (Papers I and II). However, we have not fully understood the relations between biological/pathological changes during IRI and the frequency-corresponding permittivity data that the model picks up (Paper I). The same applies to the CNN model used for the microscopic images of the small intestine. We have not yet sufficiently characterized the highlighted areas on the SHAP plot (Paper II).

4.2.5 Histology

There is no consensus on the viability limit of the IRI in the small intestine. Generally, histological analysis of the small intestine is challenging as the intestine sample can be hard to fixate and the injury can be heterogeneous [25, 53]. It is difficult to determine whether injuries observed on a part of the sample can represent the entire sample since the different types and degrees of injuries can be found within the same intestinal sample.

The histological procedures are empirical and to some extent subjective. Limitations of histology are not just the sample size and the sample type. There are potential artifacts for instance from the coloring process, and all stains present on a biopsy sample can become artifacts that cause obstacles for further analysis [53]. During the histological handling procedures, changes like arrested metabolism[5] and tissue shrinkage[6] occur, which alters the structure and

---

[5]Due to tissue fixation.
[6]Due to dehydration.

possibly chemistry of the processed tissue, resulting in variations in histological interpretations [53].

Nevertheless, histology is a useful tool for revealing pathological changes in the tissue, which are otherwise difficult to be identified with any other methods. In this work, we would suggest that it is safer to set a shorter ischemia time as the upper limit of irreversible injury in the intestinal tissue considering the uncertainties and limitations of the histological analysis.

4.3   Implications of the work

In this work, we explored various sensor techniques for the assessment of tissue viability and found that each technique has its own advantages and disadvantages. Overall, our studies have implications for both clinicians and researchers. For clinicians, these techniques could potentially lead to earlier detection of pathology and improve diagnostic accuracy. With earlier detection patient burden and costs can be reduced. With an improved accuracy for determining resection margins (for intestine) and transplantation possibilities (for livers), the need for reoperative surgeries and the risk for later complications could be reduced. For researchers, our results support the further development and refinement of instruments and enable the evaluation of techniques in a more clinical setting, as well as potential applications in other areas of gastrointestinal disease.

DRS has been shown to be sensitive to the changes occurring in the small intestine and liver during ischemia and reperfusion. This technique can provide valuable information about the severity and duration of the ischemic event and can be used to predict tissue viability. By selecting specific frequencies that are correlated with tissue changes during IRI, it may be possible to develop a simplified instrument that specifically detects the degree of IRI, which would be beneficial to clinicians. Our results on the small intestines show that dielectric property characterization combined with machine learning has a strong potential for the accurate assessment of tissue condition. To the best of our knowledge, this is the first work to report the use of LSTM and CNN models on permittivity data in the GHz region to classify intestinal IRI. Following liver resection[7], the DRS technique can potentially be utilized to intraoperatively monitor the IRI condition of the liver.

The EIS used in this study could be helpful for clinicians to evaluate the extent of IRI in the small intestine. Our results show that the P_y value correlates with the results of the histological analysis. This suggests that the P_y value could potentially serve as a score for evaluating the degree of injury, which would be much faster and more cost-effective than histological analysis. The device can be designed to be a small clip similar to photoplethysmogram sensors, which surgeons can easily apply to the intestinal segment in question and measure the impedance spectrum during surgery. The measured data can be transferred to a computer with a program that automatically analyses the impedance data and calculates the P_y value.

---

[7]Which is widely used to treat liver tumors, bile duct stones, and other liver diseases.

Both DRS and EIS require direct contact between the electrode and the tissue, highlighting the importance and need for biocompatibility of the materials, and applicable sterility procedures for the instruments. In order for these methods to be applied in clinical use, the whole design with electrodes and casing should be easy to sterilize by standard sterilization methods.

The small intestine has been imaged using a digital microscopic camera, and the image data has been combined with machine learning for the first time to evaluate IRI. This method does not require direct contact with the tissue in the same way as with the DRS and EIS techniques, facilitating its design as a medical instrument in terms of biocompatibility and sterility. Preliminary results suggest that this method has the potential to predict the duration of IRI in a porcine SMO model. By applying BNN and XAI, we were able to gain insights into the uncertainty of the model and understand how it makes predictions compared with traditional machine learning models. This method has several potential applications such as integration into present laparoscopic surgical systems to receive live evaluations during the exploration, or by using a specifically designed hand-held camera to scan the areas of interest on the small intestine during laparotomy. By transferring the acquired images or videos to a program with embedded machine learning algorithms, surgeons could be provided with real-time feedback during the examination. There may also be situations where it is appropriate for the surgeons to utilize solutions that do not provide a fully automated output, but rather use machine learning to identify relevant information in the images. This approach would provide decision support for the surgeons, potentially improving the accuracy and efficiency of their actions, while leaving the overall control of the situation and the decisions to the surgeons themselves.

Our study using VIS-NIR spectroscopy demonstrates that this technique can be used as a non-invasive and rapid tool to monitor the IRI of the small intestine. Our results indicate that wavelengths between 500-600 nm are particularly important for evaluating IRI in the porcine SMO model. This wavelength region could be further investigated to determine whether a simplified instrument with only a few diodes instead of a complex VIS spectrometer could be sufficient. Additionally, interactance measurement[8] allows for better optical sampling in the depth direction. A probe could be mounted on the operation bed over the tissue to allow for non-contact monitoring of relative changes during surgery and provide near real-time feedback to the surgeon.

Machine learning can be integrated into all the sensor techniques used in this work to automate the data analysis process and simultaneously provide a higher prediction accuracy. With an integrated machine learning algorithm, the software could process the measured data and give a prediction to the surgeon in nearly real time. This would facilitate more accurate diagnosis as well as timely and appropriate treatment adjustments. Overall, machine learning-enhanced sensor systems have a strong potential for improving the quality of care for patients.

---

[8]Where the light is transmitted into the tissue and then backscattered to the surface.

Chapter 5

Conclusions

This thesis describes the viability assessment of the small intestine and the liver following IRI, using multiple sensor systems including EIS, DRS, microscopic imaging, and VIS-NIR diffuse reflectance spectroscopy, aided by machine learning algorithms. Although these methods have shown promising results, the investigation and validation are far from finished with respect to providing the surgeon with a fast and accurate tool for decision-making during surgery. To summarize the conclusions from this thesis:

1. DRS technique can differentiate between various IRI conditions. Dielectric properties can be used to distinguish between healthy, ischemic, and reperfused small intestinal tissue.

2. ML has the potential to better identify viable and non-viable small intestinal segments than the standard clinical methods and could make the decision-making process more automatic. XAI helps to analyze the contributions of different frequencies in a classifier, making it easier both to understand what the ML model considers as important features and to enable improvement of the measurement techniques.

3. Microscopic images of the intestinal surface contain information that is likely useful for distinguishing between different degrees of IRI. ML methods can be trained with these images to classify intestinal tissue viability and injury levels.

4. The bioimpedance parameter P_y can be a useful indicator for the assessment of the viability of the small intestine. The tissue is estimated to be viable until the maximum P_y is reached, consistent with the results from the histological analysis.

5. Dielectric measurements over time on livers with different degrees of IRI show that the optimal time to evaluate the tissue condition is four hours after NMP. The dielectric conductivity parameter provides a more objective evaluation compared to the existing clinical methods.

6. The estimated upper time limit for intestinal viability in the porcine SMO model is ≤ 2 hours of ischemia based on histopathological analysis.

7. Diffuse reflectance spectroscopic measurements combined with PLS-DA modelling can be used to achieve high accuracies in the prediction of IRI in the small intestine. The findings apply not only to the differentiation between control, ischemic, and reperfused intestinal segments but also between viable and non-viable segments.

Chapter 6

Future work and perspectives

6.1 Future work

1. Investigate the passive electrical properties of the human intestine.

   - We have studied the passive electrical properties of the human intestine ex vivo with a relatively small number of samples, more experiments are needed to compare the electrical properties of the porcine and the human intestines.
   - We are in a process of testing the electrode configurations and the probe holding cases to make the device more suitable for human intestines, as they are generally larger and more cylinder-like compared to the porcine intestine.

2. Investigate different sterilization methods for the different sensor types to be used in human subjects.

   - In order to conduct experiments on humans in vivo, all sensors need to fulfill sterile requirements. Suitable sterilization methods must be investigated and tested before applying the sensors to a human subject.
   - We are investigating whether hydrogen peroxide can be used to sterilize the probe tip itself and use a sterile camera drape around most of the coaxial probe, the VNA and the communication wire, and the hand-held digital camera.

3. Investigate how machine learning models perform on the human intestine images.

   - We plan to use images of the intestine surface captured manually during open surgery to evaluate this method and the machine learning models.
   - Explore the usage of laparoscopic videos taken from patients undergoing laparoscopic surgery, to assess intestinal viability.

4. Investigate the dielectric properties of the human liver with different degrees of IRI.

   - We are currently conducting dielectric measurements on human livers that were previously deemed to have a high risk of being non-functional if transplanted and therefore donated for research purposes.

- It would be helpful to compare the dielectric properties of porcine livers with human livers to see whether the findings from the porcine studies are also applicable to humans.

- Based on predetermined viability criteria, we can investigate whether dielectric properties are useful for the assessment of the viability of the donated liver with both shorter and longer times of NMP.

- It would be insightful to correlate the dielectric data with standard perfusion parameters of liver injury and function.

5. Interactance measurements on the small intestine and the liver.

- Interactence measurements allow for better optical sampling in the depth direction and thus help capture the pathological changes in the deeper layers of the tissue.

- Test different instrumental setups for non-contact measurements. For example, a probe could be mounted over the organ to monitor the relative changes in the reflectance spectra throughout the surgery and during NMP.

6. Look into biomarkers and conduct more histological analyses both on the small intestine and the liver.

- Compare microdialysis results (concentration levels of lactate, glycerol, pyruvate, and glucose) with the changes in the dielectric parameters to gain a better understanding of the contributions of bio-molecules to the dielectric spectrum. More specifically, perform measurements on the individual bio-molecules with different concentrations in a known medium (for example water), to study the changes in the permittivity spectra with respect to frequency.

- Refine the experimental protocol based on the histological analysis. The borderline between the viable and non-viable intestines needs to be verified with more samples and with different histological grading scores as well as different pathologists.

7. Clinical studies to evaluate the experimental sensor techniques.

- Perform measurements on human small intestine during surgery. Collect data from healthy intestinal segments, segments that the surgeon believes to be irreversibly injured, and segments that the surgeon is unsure about. Compare the results with the standard clinical methods that the surgeon uses, both during the initial surgery and during the second-look surgery.

6.2 Future perspectives

An ideal viability test should satisfy the following requirements according to Horgan and Gorey [58]: 1) it must have ready availability for operating rooms;

2) the instrument must not be cumbersome or require trained personnel; 3) the method must be accurate; 4) the technique must be objective and reproducible; and 5) the method must be cost-effective.

With these requirements in mind, the work is still far from finished with respect to providing a medically certified tool for surgeons. The biggest challenge based on existing studies is that it is still not conclusive whether the investigated techniques will perform well on human subjects. Therefore, clinical studies on patients must be carried out in order to determine the clinical impacts. Moreover, sterilization and biocompatibility of the instrument remain challenging from the perspective of usage in the operating room. For the surgeons to use any of the techniques presented in this thesis, the sterilization challenge must be solved first, either in the form of gas sterilization and/or with help of single-use equipment. The DRS technique needs to be simplified with respect to the calibration process so that the clinicians can perform the calibration of the instrument using minimal time and with little training. The calibration process is rather straightforward for VIS-NIR spectroscopy and EIS.

One can speculate that all the instruments used in this work can be miniaturized and made more automatic and cost-effective. Based on the evolvement of electronic technology and artificial intelligence (AI) in the past decades, this might be a plausible scenario. The calibration process can for example be integrated into the software, and the data analysis can be made automatic with help of artificial intelligence (with minimal requirement of human work). In some cases, AI could provide predictions when fully-automated approaches are desired and when false predictions are not life-threatening. In other cases, a semi-automated approach would be more appropriate, where the AI serves as an interactive bridge between the surgeons and the tools, enabling the surgeons to make informed decisions aided by the AI's ability to simplify and coarsely categorize information. In either a fully- or semi-automated way, AI could help reduce the workload and stress for clinicians. As miniaturization and automatization are achieved, the cost for both the instruments themselves and the cost for personnel to operate the instruments will be reduced accordingly.

Overall, the sensor techniques presented in this thesis can help enhance our ability to evaluate tissue viability following IRI, once these technologies have been validated by clinical studies, powered by the strengths of AI, and improved by the evolution of electronic technology.

Bibliography

[1] Ahn, H. et al. "Measurement of bioimpedance and cell viability during ischemia-reperfusion in the rat liver". In: *2005 IEEE Engineering in Medicine and Biology 27th Annual Conference*. ISSN: 1558-4615. Jan. 2005, pp. 1945–1947.

[2] Anonymous. *An Overview of State of the Art (SOTA) Deep Neural Networks (DNNs)*. Available from: https://deci.ai/blog/sota-dnns-overview/[Online; accessed 10-January-2023]. Apr. 2022.

[3] Asami, K. "Dielectric properties of biological tissues in which cells are connected by communicating junctions". In: *Journal of Physics. D, Applied Physics* vol. 40, no. 12 (2007), pp. 3718–3727.

[4] Bala, M. et al. "Acute mesenteric ischemia: guidelines of the World Society of Emergency Surgery". In: *World Journal of Emergency Surgery* vol. 12, no. 1 (Aug. 2017), p. 38.

[5] Batyuk, L. and Kizilova, N. *Modeling of dielectric permittivity of the erythrocytes membrane as a three-layer model*. Publisher:Baltija Publishing. http://repo.knmu.edu.ua/handle/123456789/20145. Jan. 2018.

[6] Beaulieu, R. J. et al. "Comparison of open and endovascular treatment of acute mesenteric ischemia". In: *Journal of Vascular Surgery* vol. 59, no. 1 (Jan. 2014), pp. 159–164.

[7] Beltran, N. E. and Sacristan, E. "Gastrointestinal ischemia monitoring through impedance spectroscopy as a tool for the management of the critically ill". In: *Experimental Biology and Medicine* vol. 240, no. 7 (July 2015). Publisher: SAGE Publications, pp. 835–845.

[8] Benaron, D. A. et al. "Continuous, Noninvasive, and Localized Microvascular Tissue Oximetry Using Visible Light Spectroscopy". In: *Anesthesiology* vol. 100, no. 6 (June 2004), pp. 1469–1475.

[9] Bobowski, J. S. and Johnson, T. "Permittivity measurements of biological samples by an open-ended coaxial line". In: *Progress In Electromagnetics Research B* vol. 40 (2012), pp. 159–183.

[10] Boni, L. et al. "Indocyanine green-enhanced fluorescence to assess bowel perfusion during laparoscopic colorectal resection". In: *Surgical Endoscopy* vol. 30, no. 7 (July 2016), pp. 2736–2742.

[11] Brooks, J. P. et al. "Thermal imaging in the detection of bowel ischemia". In: *Diseases of the Colon and Rectum* vol. 43, no. 9 (Sept. 2000), pp. 1319–1321.

[12] Bryski, M. G. et al. "Techniques for intraoperative evaluation of bowel viability in mesenteric ischemia: A review". In: *The American Journal of Surgery* vol. 220, no. 2 (Aug. 2020), pp. 309–315.

[13] Bulkley, G. B. et al. "Intraoperative determination of small intestinal viability following ischemic injury: a prospective, controlled trial of two adjuvant methods (Doppler and fluorescein) compared with standard clinical judgment." In: *Annals of Surgery* vol. 193, no. 5 (May 1981), pp. 628–637.

[14] Cametti, C. et al. "Dielectric Relaxation Spectroscopy of Lysozyme Aqueous Solutions: Analysis of the δ-Dispersion and the Contribution of the Hydration Water". In: *The Journal of Physical Chemistry B* vol. 115, no. 21 (June 2011), pp. 7144–7153.

[15] Carden, D. L. and Granger, D. N. "Pathophysiology of ischaemia-reperfusion injury". In: *The Journal of Pathology* vol. 190, no. 3 (Feb. 2000), pp. 255–266.

[16] Chan, K. L., Chan, K. W., and Tam, P. K. "Segmental small bowel allograft–ischemic injury and regeneration". In: *Journal of Pediatric Surgery* vol. 33, no. 11 (Nov. 1998), pp. 1703–1706.

[17] Chen, J. et al. "A H2O2-activatable nanoprobe for diagnosing interstitial cystitis and liver ischemia-reperfusion injury via multispectral optoacoustic tomography and NIR-II fluorescent imaging". In: *Nature Communications* vol. 12, no. 1 (Nov. 2021). Number: 1 Publisher: Nature Publishing Group, p. 6870.

[18] Chen, S.-H., Tang, Y.-B., and Chen, H.-C. "Survival of Transferred Ileum after Ischemia Time Longer than 1 Hour: A Clinical Result Different from Animal Studies". In: *Journal of the American College of Surgeons* vol. 217, no. 2 (Aug. 2013), pp. 300–305.

[19] Chiu, C. J. et al. "Intestinal mucosal lesion in low-flow states. I. A morphological, hemodynamic, and metabolic reappraisal". In: *Archives of Surgery* vol. 101, no. 4 (Oct. 1970), pp. 478–483.

[20] Cole, K. S. and Cole, R. H. "Dispersion and Absorption in Dielectrics I. Alternating Current Characteristics". In: *The Journal of Chemical Physics* vol. 9, no. 4 (Apr. 1941). Publisher: American Institute of Physics, pp. 341–351.

[21] Cooperman, M. et al. "Use of Doppler ultrasound in intestinal surgery". In: *The American Journal of Surgery* vol. 138, no. 6 (Dec. 1979), pp. 856–859.

[22] Cour, M. F. l. et al. "Optical imaging for the assessment of hepatocyte metabolic state in ischemia and reperfusion injuries". In: *Biomedical Optics Express* vol. 8, no. 10 (Oct. 2017). Publisher: Optical Society of America, pp. 4419–4426.

[23] Cowled, P. and Fitridge, R. "Pathophysiology of Reperfusion Injury". In: *University of Adelaide Press* (2011). Ed. by Fitridge, R. and Thompson, M. Mechanisms of Vascular Disease: A Reference Book for Vascular Specialists. Available from: https://www.ncbi.nlm.nih.gov/books/NBK534267/.

[24] Cui, M. L. et al. "Bioelectrical impedance may predict cell viability during ischemia and reperfusion in rat liver". In: *Journal of Korean Medical Science* vol. 25, no. 4 (Apr. 2010), pp. 577–582.

[25] Dabareiner, R. M. et al. "Serosal Injury in the Equine Jejunum and Ascending Colon After Ischemia-Reperfusion or Intraluminal Distention and Decompression". In: *Veterinary Surgery* vol. 30, no. 2 (2001), pp. 114–125.

[26] Dabros, M. et al. "Cole–Cole, linear and multivariate modeling of capacitance data for on-line monitoring of biomass". In: *Bioprocess and Biosystems Engineering* vol. 32, no. 2 (June 2008), p. 161.

[27] Davarpanah, A. H. et al. "Many faces of acute bowel ischemia: overview of radiologic staging". In: *Insights into Imaging* vol. 12, no. 1 (Apr. 2021), p. 56.

[28] Deeba, S. et al. "Use of rapid sampling microdialysis for intraoperative monitoring of bowel ischemia". In: *Diseases of the Colon and Rectum* vol. 51, no. 9 (Sept. 2008), pp. 1408–1413.

[29] DeNobile, J., Guzzetta, P., and Patterson, K. "Pulse oximetry as a means of assessing bowel viability". In: *The Journal of Surgical Research* vol. 48, no. 1 (Jan. 1990), pp. 21–23.

[30] Douglas, W. R. "Of pigs and men and research". In: *Space life sciences* vol. 3, no. 3 (June 1972), pp. 226–234.

[31] Eltzschig, H. K. and Collard, C. D. "Vascular ischaemia and reperfusion injury". In: *British Medical Bulletin* vol. 70 (2004), pp. 71–86.

[32] Erikoglu, M. et al. "Intraoperative determination of intestinal viability: a comparison with transserosal pulse oximetry and histopathological examination". In: *The Journal of Surgical Research* vol. 128, no. 1 (Sept. 2005), pp. 66–69.

[33] Faktorová, D. "Microwave Characterization of Frequency and Temperature Dependences of Beef Bone Dielectric Properties Using Waveguide Measurement System". en. In: (2009).

[34] Faktorová, D. "Temperature Dependence of Biological Tissues Complex Permitivity at Microwave Frequencies". In: *Advances in Electrical and Electronic Engineering* vol. 7 (Jan. 2011).

[35] Farnebo, S. et al. "Urea clearance: a new technique based on microdialysis to assess liver blood flow studied in a pig model of ischemia/reperfusion". In: *European Surgical Research. Europaische Chirurgische Forschung. Recherches Chirurgicales Europeennes* vol. 45, no. 2 (2010), pp. 105–112.

[36]   Farrugia, L. et al. "Accurate in vivo dielectric properties of liver from 500 MHz to 40 GHz and their correlation to ex vivo measurements". In: *Electromagnetic Biology and Medicine* vol. 35, no. 4 (Oct. 2016). Publisher: Taylor & Francis, pp. 365–373.

[37]   Foster, K. and Schwan, H. "Dielectric properties of tissues and biological materials: A critical review". In: *Critical reviews in biomedical engineering* vol. 17 (Feb. 1989), pp. 25–104.

[38]   Gersing, E. "Impedance spectroscopy on living tissue for determination of the state of organs". In: *Bioelectrochemistry and Bioenergetics* vol. 45, no. 2 (May 1998), pp. 145–149.

[39]   Ghahramani, Z. "Probabilistic machine learning and artificial intelligence". In: *Nature* vol. 521 (May 2015), pp. 452–9.

[40]   Gonzalez, L. M., Moeser, A. J., and Blikslager, A. T. "Animal models of ischemia-reperfusion-induced intestinal injury: progress and promise for translational research". In: *American Journal of Physiology - Gastrointestinal and Liver Physiology* vol. 308, no. 2 (Jan. 2015), G63–G75.

[41]   Gonzalez, L. M., Moeser, A. J., and Blikslager, A. T. "Porcine models of digestive disease: the future of large animal translational research". In: *Translational research : the journal of laboratory and clinical medicine* vol. 166, no. 1 (July 2015), pp. 12–27.

[42]   Gordillo, M., Evans, T., and Gouon-Evans, V. "Orchestrating liver development". In: *Development (Cambridge, England)* vol. 142, no. 12 (June 2015), pp. 2094–2108.

[43]   Gragossian, A., Shaydakov, M. E., and Dacquel, P. "Mesenteric Artery Ischemia". In: *StatPearls*. Treasure Island (FL): StatPearls Publishing, 2022.

[44]   Gregory, A. P. and Clarke, R. N. "Dielectric metrology with coaxial sensors". In: *Measurement Science and Technology* vol. 18, no. 5 (Mar. 2007). Publisher: IOP Publishing, pp. 1372–1386.

[45]   Grimnes, S. and Martinsen, Ø. G. "Sources of error in tetrapolar impedance measurements on biomaterials and other ionic conductors". In: *Journal of Physics D: Applied Physics* vol. 40, no. 1 (Dec. 2006). Publisher: IOP Publishing, p. 9.

[46]   Grimnes, S. and Martinsen, Ø. G. *Bioimpedance and Bioelectricity Basics. 3rd Edition.* ISBN: 978-0-12-411533-0. Publisher: Academic Press Inc.

[47]   Grootjans, J. et al. "Human Intestinal Ischemia-Reperfusion–Induced Inflammation Characterized". In: *The American Journal of Pathology* vol. 176, no. 5 (May 2010), pp. 2283–2291.

[48]   Guan, Y. et al. "Intestinal ischemia-reperfusion injury: reversible and irreversible damage imaged in vivo". In: *American Journal of Physiology-Gastrointestinal and Liver Physiology* vol. 297, no. 1 (July 2009). Publisher: American Physiological Society, G187–G196.

[49] Han, X. et al. "A mitochondrial-targeting near-infrared fluorescent probe for bioimaging and evaluating endogenous superoxide anion changes during ischemia/reperfusion injury". In: *Biomaterials* vol. 156 (Feb. 2018), pp. 134–146.

[50] He, K. et al. "Deep Residual Learning for Image Recognition". In: *2016 IEEE Conference on Computer Vision and Pattern Recognition (CVPR)*. Los Alamitos, CA, USA: IEEE Computer Society, June 2016, pp. 770–778.

[51] Heijkant, T. C. van den et al. "Challenges in diagnosing mesenteric ischemia". In: *World Journal of Gastroenterology* vol. 19, no. 9 (Mar. 2013), pp. 1338–1341.

[52] Herbert, G. S. and Steele, S. R. "Acute and Chronic Mesenteric Ischemia". In: *Surgical Clinics of North America*. Vascular Surgery: vol. 87, no. 5 (Oct. 2007), pp. 1115–1134.

[53] Hillman, H. "Limitations of clinical and biological histology". In: *Medical Hypotheses* vol. 54, no. 4 (Apr. 2000), pp. 553–564.

[54] Hobson II, R. W. et al. "Determination of Intestinal Viability by Doppler Ultrasound". In: *Archives of Surgery* vol. 114, no. 2 (Feb. 1979), pp. 165–168.

[55] Hochreiter, S. and Schmidhuber, J. "Long Short-Term Memory". In: *Neural Computation* vol. 9, no. 8 (Nov. 1997), pp. 1735–1780.

[56] Holmes, N. J. et al. "Intraoperative Assessment of Bowel Viability". In: *Journal of Investigative Surgery* vol. 6, no. 2 (Jan. 1993). Publisher: Taylor & Francis, pp. 211–221.

[57] Holzinger, A. et al. "Causability and explainability of artificial intelligence in medicine". In: *WIREs Data Mining and Knowledge Discovery* vol. 9, no. 4 (2019), e1312.

[58] Horgan, P. G. and Gorey, T. F. "Operative Assessment of Intestinal Viability". In: *Surgical Clinics of North America*. Intestinal Ischemia vol. 72, no. 1 (Feb. 1992), pp. 143–155.

[59] Hounnou, G. et al. "Anatomical study of the length of the human intestine". In: *Surgical and radiologic anatomy: SRA* vol. 24, no. 5 (Dec. 2002), pp. 290–294.

[60] Hoyer, D. P. et al. "Controlled Oxygenated Rewarming of Cold Stored Livers Prior to Transplantation: First Clinical Application of a New Concept". In: *Transplantation* vol. 100, no. 1 (Jan. 2016), pp. 147–152.

[61] Humeau, A. et al. "Laser Doppler perfusion monitoring and imaging: novel approaches". In: *Medical & Biological Engineering & Computing* vol. 45, no. 5 (May 2007), pp. 421–435.

[62] Ivorra Cano, A. "Contributions to the measurement of electrical impedance for living tissue ischemia injury monitoring". Available from: http://www.tdx.cat/handle/10803/6333. Ph.D. Thesis. The Technical University of Catalonia, Feb. 2005.

[63]   Johnson, E. K. et al. "Fluorescence Angiography in Colorectal Resection". In: *Diseases of the Colon & Rectum* vol. 59, no. 1 (Jan. 2016), e1–e4.

[64]   Jospin, L. et al. "Hands-On Bayesian Neural Networks—A Tutorial for Deep Learning Users". In: *IEEE Computational Intelligence Magazine* vol. 17, no. 2 (May 2022), pp. 29–48.

[65]   Kalogeris, T. et al. "Ischemia/Reperfusion". In: *Comprehensive Physiology* vol. 7, no. 1 (Dec. 2016), pp. 113–170.

[66]   Kangasmaa, O. and Laakso, I. "Estimation method for the anisotropic electrical conductivity of in vivo human muscles and fat between 10 kHz and 1 MHz". en. In: *Physics in Medicine & Biology* vol. 67, no. 22 (Nov. 2022). Publisher: IOP Publishing, p. 225002.

[67]   Kannerup, A.-S. et al. "Metabolic Changes in the Pigliver During Warm Ischemia and Reperfusion Measured by Microdialysis". In: *Journal of Gastrointestinal Surgery* vol. 12, no. 2 (Feb. 2008), pp. 319–326.

[68]   Kannerup, A.-S. et al. "The influence of preconditioning on metabolic changes in the pig liver before, during, and after warm liver ischemia measured by microdialysis". In: *Hepatology International* vol. 3, no. 1 (Oct. 2008), p. 310.

[69]   Karakaş, B. R. et al. "Investigating viability of intestine using spectroscopy: a pilot study". In: *The Journal of Surgical Research* vol. 191, no. 1 (Sept. 2014), pp. 91–98.

[70]   Karpathy, A., Johnson, J., and Li, F.-F. "Visualizing and Understanding Recurrent Networks." In: *CoRR* (2015). abs/1506.02078.

[71]   Kiureghian, A. D. and Ditlevsen, O. "Aleatory or epistemic? Does it matter?" In: *Structural Safety*. Risk Acceptance and Risk Communication vol. 31, no. 2 (Mar. 2009), pp. 105–112.

[72]   Klune, J. R. and Tsung, A. "Molecular biology of liver ischemia/reperfusion injury: established mechanisms and recent advancements". In: *The Surgical Clinics of North America* vol. 90, no. 4 (Aug. 2010), pp. 665–677.

[73]   Kohlenberg, E. et al. "Determining intestinal viability by near infrared spectroscopy: A veterinary application". In: *Vibrational Spectroscopy* vol. 38 (July 2005), pp. 223–228.

[74]   Kun, S. and Peura, R. "Tissue ischemia detection using impedance spectroscopy". In: *Proceedings of 16th Annual International Conference of the IEEE Engineering in Medicine and Biology Society* (1994).

[75]   Kun, S. et al. "Real-time extraction of tissue impedance model parameters for electrical impedance spectrometer". In: *Medical & Biological Engineering & Computing* vol. 37, no. 4 (July 1999), pp. 428–432.

[76]   Kwong, A. J. et al. "OPTN/SRTR 2020 Annual Data Report: Liver". en. In: *American Journal of Transplantation* vol. 22, no. S2 (2022), pp. 204–309.

[77] La Gioia, A. et al. "Open-Ended Coaxial Probe Technique for Dielectric Measurement of Biological Tissues: Challenges and Common Practices". In: *Diagnostics* vol. 8, no. 2 (June 2018).

[78] La Hei, E. R. and Shun, A. "Intra-operative pulse oximetry can help determine intestinal viability". In: *Pediatric Surgery International* vol. 17, no. 2-3 (Mar. 2001), pp. 120–121.

[79] Lee, K. Y. et al. "Amplitude-Only Measurements of a Dual Open Ended Coaxial Sensor System for Determination of Complex Permittivity of Materials". In: *Progress In Electromagnetics Research M* vol. 28 (2013). Publisher: EMW Publishing, pp. 27–39.

[80] Leeuwen, O. B. van et al. "Hypothermic machine perfusion before viability testing of previously discarded human livers". In: *Nature Communications* vol. 12 (Feb. 2021), p. 1008.

[81] Lundberg, S. and Lee, S.-I. "A unified approach to interpreting model predictions." In: *CoRR* (2017). abs/1705.07874.

[82] Maenhout, G. et al. "Effect of Open-Ended Coaxial Probe-to-Tissue Contact Pressure on Dielectric Measurements". en. In: *Sensors* vol. 20, no. 7 (Jan. 2020). Number: 7 Publisher: Multidisciplinary Digital Publishing Institute, p. 2060.

[83] Martinsen, Ø. G., Grimnes, S., and Schwan, H. P. "Interface phenomena and dielectric properties of biological tissue". In: *Encyclopedia of surface and colloid science* vol. 20 (2002), pp. 2643–2653.

[84] Martinsen, Ø. G., Grimnes, S., and Mirtaheri, P. "Non-invasive measurements of post-mortem changes in dielectric properties of haddock muscle – a pilot study". In: *Journal of Food Engineering* vol. 43 (Feb. 2000), pp. 189–192.

[85] Matsuo, H. et al. "Experimental Studies to Estimate the Intestinal Viability in a Rat Strangulated Ileus Model Using a Dielectric Parameter". In: *Digestive Diseases and Sciences* vol. 49, no. 4 (Apr. 2004), pp. 633–638.

[86] McCance, R. A. "The effect of age on the weights and lengths of pigs' intestines." In: *Journal of Anatomy* vol. 117, no. Pt 3 (July 1974), pp. 475–479.

[87] Mellert, F. et al. "Detection of (Reversible) Myocardial Ischemic Injury by Means of Electrical Bioimpedance". In: *IEEE Transactions on Biomedical Engineering* vol. 58, no. 6 (June 2011). Conference Name: IEEE Transactions on Biomedical Engineering, pp. 1511–1518.

[88] Menke, J. "Diagnostic Accuracy of Multidetector CT in Acute Mesenteric Ischemia: Systematic Review and Meta-Analysis". In: *Radiology* vol. 256, no. 1 (July 2010). Publisher: Radiological Society of North America, pp. 93–101.

[89]   Mishima, Y. et al. "Measurement of local blood flow of the intestine by hydrogen clearance method; experimental study". In: *The Japanese Journal of Surgery* vol. 9, no. 1 (Mar. 1979), pp. 63–70.

[90]   Moss, A. A., Kressel, H. Y., and Brito, A. C. "Thermographic assessment of intestinal viability following ischemic damage". In: *Investigative Radiology* vol. 13, no. 1 (Feb. 1978), pp. 16–20.

[91]   Mudgal, K. S. and Das, N. "The ethical adoption of artificial intelligence in radiology". In: *BJR Open* vol. 2, no. 1 (Jan. 2020).

[92]   Murphy, E. and Steenbergen, C. "Ion Transport and Energetics During Cell Death and Protection". In: *Physiology (Bethesda, Md.)* vol. 23 (Apr. 2008), pp. 115–123.

[93]   Nasralla, D. et al. "A randomized trial of normothermic preservation in liver transplantation". In: *Nature* vol. 557, no. 7703 (May 2018), pp. 50–56.

[94]   O'Rourke, A. P. et al. "Dielectric properties of human normal, malignant and cirrhotic liver tissue: in vivo and ex vivo measurements from 0.5 to 20 GHz using a precision open-ended coaxial probe". In: *Physics in Medicine and Biology* vol. 52, no. 15 (Aug. 2007), pp. 4707–4719.

[95]   Olivas, E. S. et al. *Handbook Of Research On Machine Learning Applications and Trends: Algorithms, Methods and Techniques - 2 Volumes.* Hershey, PA: Information Science Reference - Imprint of: IGI Publishing, 2009.

[96]   Olthof, P. B. et al. "Warm ischemia time-dependent variation in liver damage, inflammation, and function in hepatic ischemia/reperfusion injury". In: *Biochimica et Biophysica Acta (BBA) - Molecular Basis of Disease* vol. 1863, no. 2 (Feb. 2017), pp. 375–385.

[97]   Oohata, Y. et al. "Comparison of blood flow assessment between laser Doppler velocimetry and the hydrogen gas clearance method in ischemic intestine in dogs". In: *American Journal of Surgery* vol. 160, no. 5 (Nov. 1990), pp. 511–514.

[98]   Orland, P. J. et al. "Determination of Small Bowel Viability Using Quantitative Myoelectric and Color Analysis". In: *Journal of Surgical Research* vol. 55, no. 6 (Dec. 1993), pp. 581–587.

[99]   Park, P. O. et al. "The sequence of development of intestinal tissue injury after strangulation ischemia and reperfusion". In: *Surgery* vol. 107, no. 5 (May 1990), pp. 574–580.

[100]   Patel, R., Waheed, A., and Costanza, M. "Chronic Mesenteric Ischemia". In: *StatPearls.* Available from http://www.ncbi.nlm.nih.gov/books/NBK430748/. Treasure Island (FL): StatPearls Publishing, 2021.

[101]   Peyman, A. et al. "Variation in dielectric properties due to pathological changes in human liver". In: *Bioelectromagnetics* vol. 36, no. 8 (2015), pp. 603–612.

[102] Pischke, S. E. et al. "Hepatic and Abdominal Carbon Dioxide Measurements Detect and Distinguish Hepatic Artery Occlusion and Portal Vein Occlusion in Pigs". In: *Liver Transplantation* vol. 18, no. 12 (2012), pp. 1485–1494.

[103] Pliquett, U. et al. "Py—a parameter for meat quality". In: *Meat Science* vol. 65, no. 4 (Dec. 2003), pp. 1429–1437.

[104] Quaedackers, J. S. et al. "An evaluation of methods for grading histologic injury following ischemia/reperfusion of the small bowel". In: *Transplantation Proceedings* vol. 32, no. 6 (Sept. 2000), pp. 1307–1310.

[105] Ravikumar, R., Leuvenink, H., and Friend, P. J. "Normothermic liver preservation: a new paradigm?" In: *Transplant International* vol. 28, no. 6 (2015), pp. 690–699.

[106] Redaelli, C. A., Schilling, M. K., and Büchler, M. W. "Intraoperative Laser Doppler Flowmetry: A Predictor of Ischemic Injury in Acute Mesenteric Infarction". In: *Digestive Surgery* vol. 15, no. 1 (1998). Publisher: Karger Publishers, pp. 55–59.

[107] Reginelli, A. et al. "Mesenteric ischemia: the importance of differential diagnosis for the surgeon". In: *BMC Surgery* vol. 13, no. 2 (Oct. 2013), S51.

[108] Rijn, R. van et al. "Dual hypothermic oxygenated machine perfusion in liver transplants donated after circulatory death". In: *The British Journal of Surgery* vol. 104, no. 7 (June 2017), pp. 907–917.

[109] Ruiz-Vargas, A., Ivorra, A., and Arkwright, J. W. "Monitoring the Effect of Contact Pressure on Bioimpedance Measurements". In: *2018 40th Annual International Conference of the IEEE Engineering in Medicine and Biology Society (EMBC)*. ISSN: 1558-4615. July 2018, pp. 4949–4952.

[110] Schäfer, M. et al. "Monitoring of damage to skeletal muscle tissues caused by ischemia". In: *Bioelectrochemistry and Bioenergetics* vol. 45, no. 2 (May 1998), pp. 151–155.

[111] Shah, S. D. and Andersen, C. A. "Prediction of small bowel viability using Doppler ultrasound. Clinical and experimental evaluation." In: *Annals of Surgery* vol. 194, no. 1 (July 1981), pp. 97–99.

[112] Shan, L. et al. "Near-infrared fluorescence imaging with indocyanine green for assessment of donor livers in a rat model of ischemia–reperfusion". In: *BMC Gastroenterology* vol. 22, no. 1 (Jan. 2022), p. 27.

[113] Silva, M. A. et al. "A Study of the Metabolites of Ischemia-Reperfusion Injury and Selected Amino Acids in the Liver Using Microdialysis during Transplantation". In: *Transplantation* vol. 79, no. 7 (Apr. 2005), pp. 828–835.

[114] Soares, R. O. S. et al. "Ischemia/Reperfusion Injury Revisited: An Overview of the Latest Pharmacological Strategies". In: *International Journal of Molecular Sciences* vol. 20, no. 20 (Jan. 2019). Number: 20 Publisher: Multidisciplinary Digital Publishing Institute, p. 5034.

[115]   Sowa, M. G. et al. "Detecting Intestinal Ischemia Using near Infrared Spectroscopy". In: *Journal of Near Infrared Spectroscopy* vol. 14, no. 1 (Feb. 2006). Publisher: SAGE Publishing, pp. 1–7.

[116]   Stieler Stewart, A. et al. "Intestinal Stem Cell Isolation and Culture in a Porcine Model of Segmental Small Intestinal Ischemia". In: *Journal of Visualized Experiments : JoVE*, no. 135 (May 2018), p. 57647.

[117]   Strand-Amundsen, R. J. et al. "In vivocharacterization of ischemic small intestine using bioimpedance measurements". In: *Physiological Measurement* vol. 37, no. 2 (Jan. 2016). Publisher: IOP Publishing, pp. 257–275.

[118]   Strand-Amundsen, R. J. et al. "Ischemia/reperfusion injury in porcine intestine - Viability assessment". In: *World Journal of Gastroenterology* vol. 24, no. 18 (May 2018), pp. 2009–2023.

[119]   Strand-Amundsen, R. J. "Assessment of small intestinal viability: A bioimpedance approach". Available from https://www.duo.uio.no/handle/10852/67667. Ph.D. Thesis. University of Oslo, 2019.

[120]   Strand-Amundsen, R. J. et al. "Ischemic small intestine—in vivoversusex vivobioimpedance measurements". In: *Physiological Measurement* vol. 38, no. 5 (Apr. 2017). Publisher: IOP Publishing, pp. 715–728.

[121]   Strand-Amundsen, R. J. et al. "Machine learning for intraoperative prediction of viability in ischemic small intestine". In: *Physiological Measurement* vol. 39, no. 10 (Oct. 2018). Publisher: IOP Publishing, p. 105011.

[122]   Strand-Amundsen, R. J. et al. "Small intestinal ischemia and reperfusion—bioimpedance measurements". In: *Physiological Measurement* vol. 39, no. 2 (Feb. 2018). Publisher: IOP Publishing, p. 025001.

[123]   Al-Surkhi, O. I. and Naser, R. Y. "Detection of Cell Morphological Changes of Ischemic Rabbit Liver Tissue Using Bioimpedance Spectroscopy". In: *IEEE transactions on nanobioscience* vol. 17, no. 4 (Oct. 2018), pp. 402–408.

[124]   Swerdlow, S. H., Antonioli, D. A., and Goldman, H. "Intestinal infarction: a new classification". In: *Archives of Pathology & Laboratory Medicine* vol. 105, no. 4 (Apr. 1981), p. 218.

[125]   Thomson, A. et al. *First principles of gastroenterology: the basis of disease and an approach to management.* Publisher: Medicine Group, Limited. ISBN: 978-0-8866-1434-8, 2005.

[126]   Tilsed, J. V. T. et al. "ESTES guidelines: acute mesenteric ischaemia". In: *European Journal of Trauma and Emergency Surgery* vol. 42, no. 2 (Apr. 2016), pp. 253–270.

[127]   Uhlmann, D. et al. "Assessment of hepatic ischemia-reperfusion injury by simultaneous measurement of tissue pO2, pCO2, and pH". In: *Microvascular Research* vol. 67, no. 1 (Jan. 2004), pp. 38–47.

[128] Ulrich, F. et al. *Microdialysis as a tool for measuring ischemia-reperfusion injury in an isolated reperfusion model of pig liver-Is it worth while?* Pages: S215. Jan. 2007.

[129] Ungerstedt, J. et al. "Microdialysis monitoring of porcine liver metabolism during warm ischemia with arterial and portal clamping". In: *Liver Transplantation* vol. 15, no. 3 (2009), pp. 280–286.

[130] Urbanavičius, L. et al. "How to assess intestinal viability during surgery: A review of techniques". In: *World Journal of Gastrointestinal Surgery* vol. 3, no. 5 (May 2011), pp. 59–69.

[131] Voosen, P. "How AI detectives are cracking open the black box of deep learning". In: *News article in Science* (2017). Available from: https://www.science.org/content/article/how-ai-detectives-are-cracking-open-black-box-deep-learning. [Online; accessed 12-January-2021].

[132] Vries, Y. de et al. "Pretransplant sequential hypo- and normothermic machine perfusion of suboptimal livers donated after circulatory death using a hemoglobin-based oxygen carrier perfusion solution". In: *American Journal of Transplantation: Official Journal of the American Society of Transplantation and the American Society of Transplant Surgeons* vol. 19, no. 4 (Apr. 2019), pp. 1202–1211.

[133] Vries, Y. de et al. "Transplantation of high-risk donor livers after resuscitation and viability assessment using a combined protocol of oxygenated hypothermic, rewarming and normothermic machine perfusion: study protocol for a prospective, single-arm study (DHOPE-COR-NMP trial)". In: *BMJ open* vol. 9, no. 8 (Aug. 2019), e028596.

[134] Wikipedia contributors. *Dielectric spectroscopy — Wikipedia, The Free Encyclopedia.* https://en.wikipedia.org/w/index.php?title=Dielectric_spectroscopy&oldid=1125106452. [Online; accessed 18-January-2022]. 2022.

[135] Willerson, J. T. "Pharmacologic Approaches to Reperfusion Injury". In: *Advances in Pharmacology.* Ed. by August, J. T. et al. Vol. 39. Academic Press, Jan. 1997, pp. 291–312.

[136] Winbladh, A. et al. "Segmental Ischemia of the Liver – Microdialysis in a Novel Porcine Model". In: *European Surgical Research* vol. 43, no. 3 (2009). Publisher: Karger Publishers, pp. 276–285.

[137] Winbladh, A. "Microdialysis in Liver Ischemia and Reperfusion injury". Available from: http://urn.kb.se/resolve?urn=urn:nbn:se:liu:diva-68651. Ph.D. Thesis. Linköping University, 2011.

[138] Wu, M.-Y. et al. "Current Mechanistic Concepts in Ischemia and Reperfusion Injury". In: *Cellular Physiology and Biochemistry* vol. 46, no. 4 (2018). Publisher: Karger Publishers, pp. 1650–1667.

[139] Xie, F. et al. "Evaluation of Liver Ischemia-Reperfusion Injury in Rabbits Using a Nanoscale Ultrasound Contrast Agent Targeting ICAM-1". In: *PLOS ONE* vol. 11, no. 4 (Apr. 2016). Publisher: Public Library of Science, e0153805.

[140] Xu, R. et al. "A near-infrared fluorescent probe for evaluating endogenous hydrogen peroxide during ischemia/reperfusion injury". In: *Analyst* vol. 144, no. 8 (2019). Publisher: Royal Society of Chemistry, pp. 2556–2564.

[141] Yamada, T. et al. "An experimental estimation of the maximum period of liver preservation using dielectric parameters". In: *Transplantation Proceedings* vol. 34, no. 4 (June 2002), pp. 1098–1104.

[142] Yanar, H. et al. "Planned second-look laparoscopy in the management of acute mesenteric ischemia". In: *World Journal of Gastroenterology : WJG* vol. 13, no. 24 (June 2007), pp. 3350–3053.

[143] Yandza, T. et al. "The pig as a preclinical model for intestinal ischemia-reperfusion and transplantation studies". In: *The Journal of Surgical Research* vol. 178, no. 2 (Dec. 2012), pp. 807–819.

[144] Yang, Y. et al. "Improved Cole parameter extraction based on the least absolute deviation method". In: *Physiological Measurement* vol. 34, no. 10 (Oct. 2013), pp. 1239–1252.

[145] Zhang, Z. et al. "A review: Application and research progress of bioimpedance in meat quality inspection". en. In: *Journal of Food Process Engineering* vol. 45, no. 11 (2022), e14153.

[146] Zhou, Z., Xu, M.-J., and Gao, B. "Hepatocytes: a key cell type for innate immunity". In: *Cellular & Molecular Immunology* vol. 13, no. 3 (May 2016). Number: 3 Publisher: Nature Publishing Group, pp. 301–315.

[147] Ziegler, A., Gonzalez, L., and Blikslager, A. "Large Animal Models: The Key to Translational Discovery in Digestive Disease Research". In: *Cellular and Molecular Gastroenterology and Hepatology* vol. 2, no. 6 (Sept. 2016), pp. 716–724.

Papers

Paper I

Small intestinal viability assessment using dielectric relaxation spectroscopy and deep learning

Jie Hou, Runar Strand-Amundsen, Christian Tronstad, Tor Inge Tønnessen, Jan Olav Høgetveit, Ørjan Grøttem Martinsen

I

scientific reports

OPEN

Small intestinal viability assessment using dielectric relaxation spectroscopy and deep learning

Jie Hou[1,2✉], Runar Strand-Amundsen[2], Christian Tronstad[2], Tor Inge Tønnessen[3,4], Jan Olav Høgetveit[1,2] & Ørjan Grøttem Martinsen[1,2]

Intestinal ischemia is a serious condition where the surgeon often has to make important but difficult decisions regarding resections and resection margins. Previous studies have shown that 3 h (hours) of warm full ischemia of the small bowel followed by reperfusion appears to be the upper limit for viability in the porcine mesenteric ischemia model. However, the critical transition between 3 to 4 h of ischemic injury can be nearly impossible to distinguish intraoperatively based on standard clinical methods. In this study, permittivity data from porcine intestine was used to analyze the characteristics of various degrees of ischemia/reperfusion injury. Our results show that dielectric relaxation spectroscopy can be used to assess intestinal viability. The dielectric constant and conductivity showed clear differences between healthy, ischemic and reperfused intestinal segments. This indicates that dielectric parameters can be used to characterize different intestinal conditions. In addition, machine learning models were employed to classify viable and non-viable segments based on frequency dependent dielectric properties of the intestinal tissue, providing a method for fast and accurate intraoperative surgical decision-making. An average classification accuracy of 98.7% was obtained using only permittivity data measured during ischemia, and 96.2% was obtained with data measured during reperfusion. The proposed approach allows the surgeon to get accurate evaluation from the trained machine learning model by performing one single measurement on an intestinal segment where the viability state is questionable.

Intestinal ischemia is a fairly uncommon but life-threatening event. Early diagnosis and intervention are of vital importance to preserve sufficient bowel function while avoiding necrosis, peritonitis, and possible death of the patient. Selection of resection areas and decisions on resection margins requires a lot of surgical experience and uncertainty can be high. Clinical judgment based on visual criteria has a reported sensitivity of 78–89%, but this includes a second look evaluation and resection of a part of the viable bowel in 46% of the cases to avoid leaving non-viable bowel in the patient[1,2]. Patients may risk short gut syndrome if resection is performed too aggressively. Due to the difficult task of assessing intestinal viability upon the first inspection, a second look-operation after 24–36 h is the standard of care in cases with high uncertainty.

Over the years, many experimental approaches have been pursued to investigate the possibility of providing better tools for the surgeon. Among these are studies investigating the association between the dielectric properties of the intestine and tissue state. A well-known study conducted by Gabriel S. et al.[3] reported the dielectric properties of several biological tissues including the intestine in the frequency range from 10 Hz to 20 GHz. In 2003, Sasaki et al.[4] developed the best fit values for parameters in the Cole-Cole model for the dielectric properties of 43 biological tissues and organs, including the small intestine. Some years later Salahuddin et al.[5] proposed a two-stage generic algorithm to optimize the dielectric properties of 54 types of human tissues. Both studies were based on the measurements done by Gabriel S. et al.[3].

To the best of our knowledge, no studies have been conducted on the dielectric properties of the small intestine during ischemia and reperfusion injury in the GHz region. The closest are those conducted by Strand-Amundsen

[1]Department of Physics, University of Oslo, Sem Sælands Vei 24, 0316 Oslo, Norway. [2]Department of Clinical and Biomedical Engineering, Oslo University Hospital, 0424 Oslo, Norway. [3]Department of Emergencies and Critical Care, Oslo University Hospital, Oslo 0424, Norway. [4]Institute of Clinical Medicine, University of Oslo, 0318 Oslo, Norway. ✉email: jieho@fys.uio.no

et al.[6,7] reporting trans-intestinal measurements of electrical parameters during ischemia and reperfusion in the 1 kHz–1 MHz range. Some studies have reported that dielectric properties are useful in evaluating viability of heart and liver after ischemia and reperfusion injury[8–11]. Knowledge about whether dielectric relaxation spectroscopy can be used to evaluate the small intestine condition and how different ischemia and reperfusion conditions affect the dielectric properties of the small intestine is still lacking.

We used permittivity measurements to investigate the dielectric properties of healthy, ischemic, and reperfused small intestine in a porcine model. The dielectric properties of biological substances reflect the tissue structures and chemical composition, and both will change during ischemia and reperfusion injury[10,12,13]. We investigated how the dielectric properties changed with different degrees of ischemia and reperfusion over time.

To make decisions on tissue resection and resection margins, it is important to determine whether the intestinal segment in question is viable or non-viable. Previous experiments have reported that small intestinal tissue undergoing ischemia followed by reperfusion, has a viability limit that occurs between 3–4 h of ischemic duration[6]. We explored the possibility of using machine learning (ML) methods together with dielectric properties to differentiate whether the small intestine has been in the ischemic phase for less than 4 h (viable) or 4 h or more (non-viable). To assess and visualize the importance of features among the frequency-dependent dielectric tissue properties as predictors in the ML classifiers, the SHapley Additive exPlanations (SHAP) method[14] in explainable artificial intelligence (AI) was implemented.

Results

In the present study, four cases were created and measured in each porcine subject as described in "Animals and experimental design" section. 10 permittivity measurements were performed on each case per hour, resulting in a total of 3020 measurements (700 control measurements, 1490 ischemic phase measurements, and 830 reperfusion phase measurements).

Permittivity analysis. The different states of perfusion in the intestinal tissue (control, ischemia and reperfusion) led to differences in the mean of the dielectric constant as a function of frequency (Fig. 1a). The dielectric constant for the ischemic intestine was lower compared to the control while the dielectric constant for the reperfusion phase was higher. There was some overlap between control and ischemic dielectric constant data, while the overlap between ischemic and reperfused intestine was minimal.

This study revealed δ-and γ-dispersions that characterize the frequency dependence of dielectric properties of the small intestine. δ-dispersion was most likely produced by the dipole relaxation of the bound-water in the intestine tissue. As the frequency increases, polarization decreases as each polarization mechanism ceases to contribute, resulting in a decrease in dielectric constant for all conditions. The ischemic intestine had the lowest overall dielectric constant, followed by the healthy intestine, while the reperfused intestine displayed the highest dielectric constant value. The same trend was observed with the dielectric conductivity of the three tissue conditions.

Figure 1b shows a violin plot of the relative change in the dielectric constant at frequency 6.25 GHz. One-way ANOVA with Sidak correction for repeated measurements was used to compare the dielectric constant data in case 3 and 4 at selected timepoints. Pairwise comparisons were performed for the two cases (case 3 and 4) with same reperfusion time. There were significant differences between the two cases in the time development of the dielectric constant during the first and fourth hour of the reperfusion phase.

Figure 1c and 1d shows the relative change in dielectric constant and dielectric conductivity of both ischemic and reperfused intestine compared to data obtained from the control intestine. Relative change in dielectric constant and dielectric conductivity were calculated as:

$$\Delta\epsilon' = \frac{\epsilon' - \epsilon'_{control}}{\epsilon'_{control}} \times 100\%. \qquad (1)$$

$$\Delta\sigma = \frac{\sigma - \sigma_{control}}{\sigma_{control}} \times 100\%. \qquad (2)$$

$\Delta\epsilon'$ of the ischemic intestine (Fig. 1c) showed one broad peak extending in the 4–10 GHz range. $\Delta\epsilon'$ of the reperfused intestine increased from 200 MHz to around 2.5 GHz then decreased for the following 2.5 GHz, followed by another peak around 10 GHz. $\Delta\sigma$ for the ischemic phase in Fig. 1d showed a higher dielectric conductivity characteristic compared to the control group up to 3 GHz, while the $\Delta\sigma$ for reperfusion phase showed a decreasing trend up to 3 GHz. The $\Delta\sigma$ showed a peak around 11 GHz for the ischemic case, whereas two peaks centered around 4 GHz and 12 GHz were seen with the reperfused case, exceeding almost 15% over the dielectric conductivity of the control case.

Table 1 shows the selected cases and the corresponding fitted Cole-Cole parameters. The R^2 value was above 0.995 during all fitting procedures and ϵ_∞ were all less than 10. For the cases during ischemia, we see a decreasing trend on $\Delta\epsilon_1$ and an increasing trend on $\Delta\epsilon_2$, whereas the relaxation time τ_1 declines as ischemic time increases. $\Delta\epsilon_1$ for 3 and 4 h ischemia followed by 1 and 3 h reperfusion exhibited an increasing trend, while $\Delta\epsilon_2$ showed the opposite behavior. τ_1 increased with longer reperfusion time. No obvious trend was observed on τ_2 throughout all cases.

Determination of intestinal viability using ML. The permittivity data was divided into two types of data describing the two main mechanisms occurring in the intestinal tissue during the experiment, namely ischemic permittivity data (from the events with full occlusion) and reperfusion permittivity data (from the
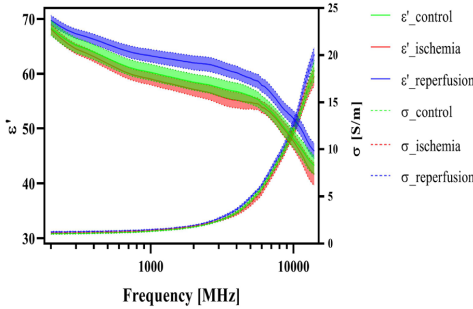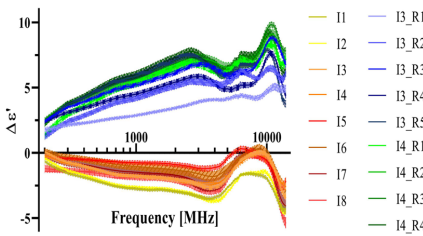
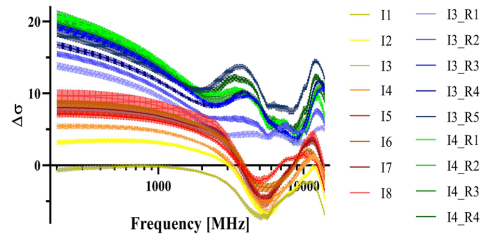(a) Dielectric constant and dielectric conductivity of control, ischemic and reperfused small intestine.
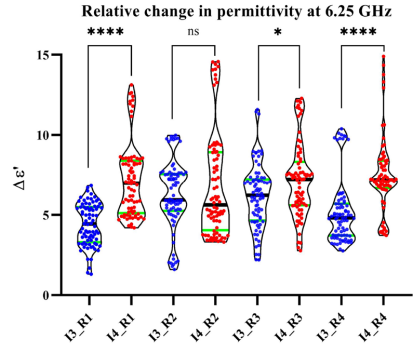
(b) Violin plot of relative change in dielectric constant at frequency 6.25 GHz. The black line in the middle indicate the median value of the relative change in the dielectric constant, whereas the lower and upper green lines show the 25th and 75th percentile, respectively.

(c) Relative change in the dielectric constant of ischemic and reperfused small intestine with one hour interval.

(d) Relative change in the dielectric conductivity of ischemic and reperfused small intestine with one hour interval.
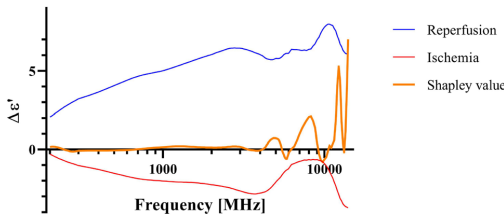
Figure 1. Dielectric constant and dielectric conductivity plots of control, ischemic and reperfusion phase of the small intestine with mean value and 95% confidence interval. "I" = Ischemia and "R" = Reperfusion, numbers are shown in hours. Significant codes: ≤ 0.0001 "$* * **$", ≤ 0.05 "$*$", Not significant, "ns". Frequency range is 200 MHz–14 GHz.

	$\Delta \epsilon_1$	$\Delta \epsilon_2$	τ_1 [ps]	τ_2 [ps]
Control	20.21	44.81	825.30	8.46
I-1h	19.48	56.49	675.20	7.06
I-4h	18.99	56.93	655.82	6.89
I-5h	15.48	57.95	574.18	6.90
I-6h	15.08	58.08	529.70	7.21
I-3h-R-1h	13.07	44.32	594.73	8.69
I-3h-R-3h	13.70	42.45	724.48	8.95
I-4h-R-1h	12.90	43.41	741.75	8.94
I-4h-R-3h	21.12	41.65	1222.23	8.95

Table 1. Extracted Cole–Cole parameter from fitting equation (4) to the experimental data. "I" = Ischemia, "R" = Reperfusion and "h" = hour(s).

71

Model performance						
Architecture	Freq.	Data	Accuracy (%)	F1 score (%)	Sensitivity (%)	Specificity (%)
LSTM	W	I	96.9 ±1.5	97.6 ±1.3	98.4 ±1.4	97.4 ±1.0
		R	92.2 ±1.0	93.0 ±1.1	89.2 ±1.1	94.6 ±1.4
	S	I	93.9 ±1.4	95.1 ±1.4	90.7 ±3.0	95.8 ±2.4
		R	93.4 ±6.5	94.2 ±6.3	89.2 ±6.1	96.7 ±5.8
Bi-LSTM	W	I	97.7 ±1.3	98.2 ±1.1	98.4 ±1.8	96.2 ±1.4
		R	95.2 ±2.7	95.6 ±2.8	93.5 ±5.4	97.3 ±2.5
	S	I	96.9 ±1.4	97.7 ±1.2	96.2 ±1.4	97.4 ±1.1
		R	92.2 ±4.2	93.1 ±3.7	98.2 ±1.2	93.4 ±5.5
Residual LSTM	W	I	98.7 ±0.2	98.8 ±0.1	97.9 ±0.3	99.6 ±0.3
		R	96.2 ±1.1	95.4 ±1.2	95.6 ±1.7	97.0 ±2.5
	S	I	93.8 ±1.3	94.2 ±1.2	92.5 ±0.3	94.9 ±1.7
		R	94.2 ±2.4	92.8 ±2.9	95.6 ±2.9	93.3 ±2.4
1D-CNN	W	I	97.8 ±0.5	98.3 ±0.4	97.7 ±0.6	97.9 ±1.2
		R	87.2 ±2.9	89.0 ±2.2	80.2 ±0.8	92.8 ±2.9
	S	I	95.9 ±0.8	96.6 ±0.8	95.2 ±1.1	96.3 ±0.9
		R	75.7 ±1.1	79.2 ±1.7	65.1 ±1.4	84.1 ±1.1

Table 2. Model performance for classifying viable and non-viable small intestine segments after different degrees of ischemic injury. Binary classification classes are divided as following for both ischemic and reperfusion data: class 1: ischemic condition for 1, 2, and 3 h, class 2: ischemic condition for 4–8 h. Both average and standard deviation from 5-fold cross validation are shown in the table. "W" = Whole, indicates that the whole frequency range was used (200 MHz–14 GHz). "S" = Selected, indicates that the selected frequency range was used (6 GHz–14 GHz). "I" = Ischemia and "R" = Reperfusion.

Figure 2. Shapley values plotted with the relative change in dielectric constant for ischemic and reperfusion phase. Where positive shapley values indicate positive contribution to the model classification performance and negative shapley values implies negative contribution to the model performance.

events where occlusion was followed by reperfusion). The two data types were again divided into subgroups of ischemic exposure for less than 4 h (1–3 h) or not (4–8 h) and also to reperfusion time following the ischemic exposure. The dividing of different groups was based on an earlier study which suggested that 3 h of full ischemia followed by reperfusion is the upper limit for viability in the porcine intestinal ischemia model[6]. Three different LSTM models and a 1D-CNN model were used to differentiate between the two groups, Table 2 shows the classification results. Figure 2 shows how features extracted by the SHAP method (frequencies with corresponding dielectric constants) contributes to the classification.

The PCA method was used additionally to select and verify the most important frequencies in distinguishing the viable and non-viable intestinal segments and to crosscheck with the frequencies that the SHAP method picked out. Two components were extracted from PCA, both for the ischemia and reperfusion dataset. For the ischemia dataset, the first principal component (dominated by 6.75 GHz) explained 30.4% of the variation while the second component (dominated by 11.25 GHz) explained 19.2% of the variation. For the reperfusion dataset, the first principal component (dominated by 13.25 GHz) explained 51.3% of the variation while the second component (6.00 GHz) explained 22.9% of the variation.

Based on the results from PCA and SHAP, we selected the frequency range 6 GHz–14 GHz to retrain the LSTM models and the 1D-CNN model to check whether we can obtain similar model performance by using fewer data points.

Table 2 shows that residual LSTM obtained an overall higher performance compared to the other three models. Bi-directional LSTM outperformed conventional LSTM in all cases except for the selected frequency range for the reperfusion case. Classification results achieved a mean accuracy of 98.7% with full frequency spectrum, and 96.2 % with the selected frequency range using residual LSTM. 1D-CNN model showed similar

performance as the LSTM models for ischemia data, while the performance was worse when reperfusion data were used. Comparing accuracy score obtained from different frequency ranges, by using only the selected frequency range, we received only a slightly lower accuracy; an average decrease of 2.6% across all models for the ischemic case, and 3.8% for the reperfusion case. With the conventional methods support vector machine (SVM) and random forest (RF) we were not able to achieve similar accuracies as the deep learning methods. With SVM, mean accuracies of 59.7% and 61.7% was obtained for the ischemia and reperfusion data when the whole frequency range was used. When using only the selected frequencies an accuracy of 60.5% and 63.9% was obtained. The RF model showed a similar performance as the SVM model, with mean accuracies of 61.1% and 55.5% for ischemia and reperfusion data respectively when the whole frequency range was used and 53.9% and 57.8% when using only the selected frequencies. Detailed results from SVM and RF models can be find in the Supplementary Information.

Discussions

We investigated the dielectric properties of the small intestine in the GHz region during ischemia and reperfusion and found that these properties can be used to discriminate intestinal tissue viability. This opens for novel intraoperative methods of assessment of intestinal tissue state and tissue resection margins, where the benefit is increased accuracy in assessment of intestinal tissue state combined with a drastic reduction in time to make the assessment. Our results indicate that there is an association between dielectric properties and the physiological condition of the small intestinal tissue.

The pig model was selected as it has important anatomical and physiological similarities to humans[15]. Especially important is the similarity in pathophysiology of ischemia/reperfusion between the pig model and humans. The pig model has previously been suggested as a reference standard in intestinal transplantation research[16]. The segmental mesenteric occlusion model that we used[17] provides a well-defined area of ischemic injury affecting the whole intestinal wall in the occluded segment[16], in contrast to the more spatially variable results that typically is reported when using superior mesenteric artery or vein occlusion.

To the best of our knowledge, the current work is the first to report the dielectric properties of ischemia/reperfusion injury of the intestinal tissue in the GHz region and to apply different LSTM models to sequences of frequencies to classify tissue conditions. There are only a few other studies that use LSTM for classification of tissue conditions. Strand-Amundsen et al.[18] used the LSTM model on low frequency bioimpedance measurements to classify small intestine status and Otto et al.[19] used LSTM in classification on optical coherence tomography data. Compared to the previous studies measuring the low frequency electrical properties of intestinal ischemia/reperfusion injury, where the ischemic and reperfusion phases showed overlap at certain points during the ischemia/reperfusion course[20], the overlap is minimal in the high frequency permittivity measurements, increasing the separability of characteristics of ischemic and reperfusion phases.

An overall lower dielectric constant was observed for the ischemic intestinal segments, and an overall higher dielectric constant was observed for reperfused intestine compared to the control case. Hahn et al.[21] suggested that a decrease in blood volume might cause a decrease in permittivity during ischemic conditions.

The relative changes in the dielectric constant ($\Delta\epsilon'$) of the ischemic phase compared to the control case showed a single peak around 10 GHz, whereas $\Delta\epsilon'$ of the reperfusion phase showed two separate peaks. The first peak in the δ-dispersion region, may be associated with proteins, cellular organelles and protein-bound water[22]. Prolonged ischemia will result in lactate accumulation, followed by dysfunctional ATP base-dependent ion transport mechanisms, gradually contributing to cell swelling and eventually necrosis[23]. Necrosis leads to the contents of the cells leaking to the interstitial fluid influencing neighboring cells and forming molecular interactions with substances in the extracellular fluid. The two peaks in the reperfusion data indicates that certain molecules are released during the reperfusion phase which were not present, or of lower concentration during the ischemic phase. With higher excitation frequencies, big polar molecules with a large dipole moment will struggle to orient with the fast alternating field, giving less polarization which in turn leads to lower permittivity. The observed increase in permittivity in the reperfusion phase compared to the control case can be attributed to increased concentration of smaller polar molecules including water molecules.

The reperfused tissue was edematous and swollen compared to both the control and the ischemic tissue. Excessive accumulation of interstitial fluid leading to increased water content may be one of the causes of increased permittivity during the reperfusion phase at the higher frequencies.

The electrical charging effects of the cell membranes decrease with increasing frequency, while the dielectric characteristics of the intestinal tissue reflect the properties of intercellular and intracellular electrolytes and water molecules[24]. Schwan and Foster[25] concluded that the dielectric properties of tissues like liver and muscle at frequencies above 1 GHz could be attributed directly to their free water and normal bulk water contents.

Microdialysis has been used in earlier studies[6] to collect metabolic markers during ischemia/reperfusion injury. Ischemia followed by reperfusion for 1–8 h resulted in an increase in lactate and glycerol concentration levels. Both lactate and glycerol are relatively small polar molecules that can be detected by DRS in the measured frequency range, and we estimate that they contribute to the increase in dielectric constant in the lower GHz range.

Overall dielectric conductivity for both the ischemia and the reperfusion cases were higher compared to the control case, indicating higher dielectric loss, which suggests that the energy loss associated with rotation of the molecules was higher. The dielectric conductivity around 1 GHz increased as the intestines were exposed to ischemic injury, possibly because of an increase in the concentration of larger molecules, leading to more energy loss as they rotate to follow the fast alternating field.

In the frequency range of 1.5 GHz to 14 GHz for the ischemia case, we observed a trough in the $\Delta\sigma$. This can be explained by a concentration reduction of polar molecules and loss of ability to follow the fast alternating

electric field for bigger molecules, leading to a decreased energy loss. For cases where ischemic injury was followed by reperfusion, the changes in measured dielectric conductivity can be explained by a concentration increase in large polar molecules (compared to water molecules), where when the frequency increases, they struggle to follow the alternating field, exhibiting a decreasing trend in energy loss. The last increase and decrease in dielectric conductivity around the 10 GHz–14 GHz region is possibly caused by an increase in water content due to edema, where water molecules dominate in this frequency range.

A double Cole-Cole equation was used to fit the permittivity data, while we tested and rejected both a single Cole-Cole equation (not adequate) and a combination of three Cole-Cole equations (the improvement of the R^2 score was minimal). The time constant τ obtained from the fitting procedure varied from picoseconds to nanoseconds, which accounts for partial orientation of molecular dipoles[26]. Most biological materials do not exhibit single relaxation behavior. Multiple relaxation processes might occur in parallel as the relaxation time of polar molecules with similar structures and dipole moment overlaps[26], thus the relaxation times obtained from the fitting procedure are means which include the contribution from several dipole molecules. The decreasing trend in τ_1 (Tab. 1) observed in ischemic phase measurements may be due to dissociation in hydrogen bonds with water as the blood flow decreases during ischemia. The increasing trend in the mean relaxation time during reperfusion might be re-connection of hydrogen bonds with increased water content.

Three LSTM models were tested, all taking spectral information into account. Comparing bidirectional LSTM with unidirectional LSTM, by feeding the model with data once from the beginning to the end and once from the end to the beginning, the bidirectional LSTM has the ability to learn sequential information in both directions, enabling improved context leaning and a possibility for improved model performance. Residual LSTM showed the overall best model performance and shortest computational time. Due to the additional spatial shortcut path from the lower layers, the model provides more efficient training of deep networks[27]. In addition, a 1D-CNN model was tested to compare with the LSTM models. The 1D-CNN model performed comparably well with the LSTM models, with slightly lower overall performance. The conventional machine learning methods SVM and RF were also tested to assess how simpler machine learning models perform for our binary classification problem. 5-fold cross validation were used for both SVM and RF models. The results show that the SVM and RF models are not well suited to classify the non-linear frequency dependent permittivity data. This indicates that deep learning methods is needed to more accurately differentiate between the two classes.

5-fold nested CV was used to prevent "leaking" of the information into the model and overfitting on the training data. Model selection without nested CV would use the same data to tune model hyperparameters and evaluate model performance which may lead to optimistically biased evaluation of the model[28].

By halving the frequency range, the amount of data was reduced, which lowers the requirement specifications for the instruments. By basing the classification on a single input spectral sweep, we provide a clinical solution for decision-making where the surgeon needs only to conduct one measurement (which takes around one second), and the model will provide the classification of the tissue sample under test. This allows for a great reduction in time consumption compared to the present standard clinical methods.

Integration of ML based algorithms during intraoperative evaluation of intestinal viability can make tissue diagnosis more automatic, robust and objective. The potential is to increase the accuracy of viability assessment and decisions on resection margins, and to reduce the need for second look surgery.

Eight pigs with 4 cases each of ischemia/reperfusion models were used in this study, with hourly measurements on all cases over a period of 8 hours. The number of pigs was relatively low compared to the number of measurements, but individual variation within each subject and each intestinal segment was minimal. Using data from the same segment for training and testing might have limited the realism of the accuracy estimates. The number of pigs was insufficient for data to be split on segments to avoid the dependence with repeated measurements. While we are at an early stage in the development of our method, our analysis demonstrates the potential to train a ML model to discriminate between tissue viability states. In the future, a larger dataset should be utilized to further develop the model to increase the generalizability and to validate the results with independent observations.

A 3D printed clip (Fig. 3) ensured that there was near-constant pressure between the probe and the intestinal tissue, but small variations may have influenced the measurements. Another potential error source could be irritation in the intestinal segments caused by our physical handling of the intestine. During the measurements, the intestine was exposed to air, leading to periods with decreased temperature, which may have influenced the dielectric properties of the tissue.

The borderline between viable and non-viable intestine tissue was based on previous work[6], and a histological follow-up study should be conducted to verify these assumptions.

Conclusion

We report the dielectric properties of the small intestine during different ischemia and reperfusion conditions. Permittivity measurements appear to be a promising method for accurate and semi-automatic differentiation between healthy, ischemic, and reperfused small intestine in a porcine model. Assisted by LSTM-RNN, we were able to identify viable and non-viable intestinal segments with a mean accuracy of 98.7% with residual LSTM, based on single frequency sweep measurement. This approach has the potential to increase the diagnostic precision and introduces a new method to evaluate the intestine viability. Our results show that dielectric property characterization of small intestine combined with ML is reliable and has a strong potential for accurate resection of non-viable intestinal segments leaving viable segments unresected. This will most probably mean a better prognosis for the patient and markedly reduce the need for second look surgery 1–3 days after the acute surgery. Evaluation of this approach on human intestine is our next target.
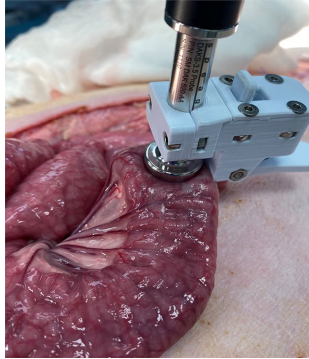
Figure 3. Experimental setup.

Methods

Animals and experimental design.   Eight Norwegian Landrace pigs were included in this study, weight range 50–66 kg and 5 were female. The pigs were normally healthy pigs and were screened by a professional pig breeder, to avoid disease. Food was withheld 12 h prior to surgery. We used the same experimental protocol as Strand-Amundsen et al.[7,29]. For each pig, we selected four random segments of jejunum for the four cases of the protocol;

- Case 1: Control—8 h of normal perfusion.
- Case 2: Ischemia—8 h of warm full ischemia.
- Case 3: 3 h of ischemia followed by 5 h of reperfusion.
- Case 4: 4 h of ischemia followed by 4 h of reperfusion.

Ischemia was performed by clamping the arteries and veins of the jejunal mesentery of the selected segments, resulting in a 30 cm central zone of warm ischemia and two surrounding edge zones of marginal tissue hypoxia[7,29]. The choice of time duration for Case 3 and Case 4 is based on the previously published work by Strand-Amundsen et al.[6] where they found that irreversible injury occurs around 3–4 h of ischemia based on histological analysis. In vivo permittivity measurements were conducted hourly over an 8 h period. All intestinal segments received the same treatment, while ischemic exposure varies dependent on the protocol. After the experiment, the animals were sacrificed by a lethal dose of potassium chloride (100 mmol). The experiment was approved by the Norwegian Food Safety Authority (NFSA) and conducted in accordance with national animal welfare guidelines. The NFSA is a national authority that since 2015 replaces all institutional review boards and ethics committees regarding animal research and welfare. All methods are reported in accordance with ARRIVE guidelines (https://arriveguidelines.org).

Surgery, anaesthesia and monitoring.   Surgery was performed under sterile conditions. Anesthesia was induced with intramuscular ketamine (Warner Lambert, Morris Plains, NJ) 15 mg/kg, azaperone (Janssen-Cilag Pharma, Austria) 1 mg/kg, and atropine (Nycomed Pharma, Asker, Norway) 0.02 mg/kg. Tracheostomy was performed initially for mechanical ventilation. Following tracheotomy, anesthesia was maintained with isoflurane (Abbott Scandinavia AB, Kista, Sweden) (1–1.5%) and a mixture of air and O_2 to obtain a FiO_2 of 30% to ensure arterial oxygen saturation >92%. Morphine (Alpharma, Oslo, Norway) 0.4–0.7 mg/kg/h was administered as a continuous intravenous infusion. Ventilation was adjusted to a pCO_2 of 5–6 kPa. A continuous infusion of Ringer acetate 10–30 ml/kg/h was administered as fluid replacement. The jejunum was made accessible through mid-line laparotomy[7,29].

Permittivity measurements.   Dielectric relaxation spectroscopy (DRS) was performed with the open-ended coaxial probe (OCP) method[30], to characterize the dielectric properties of materials. We used the OCP DAK 3.5: 200 MHz–20 GHz (Schmid & Partner Engineering AG, Switzerland) and the R140: 85 MHz - 14 GHz (Copper Mountain Technologies) vector network analyzer (VNA). Combining the limitations of the probes and the VNA, the measurement frequency range for our setup was 200 MHz to 14 GHz. A standard 3-point calibration[31,32] "Open", "Short", and "Load" were performed prior to each hourly measurement to maintain the accuracy of the analyzer. To estimate the uncertainty of the measurement we used the methodology described by Gregory and Clarke[30] that includes estimates of possible systematic errors due to design, calibration uncertainties, temperature differences between the calibration and measurements, and VNA noise. The uncertainty in the measurements was found to be within the range of errors (1.7% for the frequency range 200 MHz–5 GHz and 3.5% for 5 GHz–14 GHz) that is acceptable for the setup.

75

To ensure stable pressure and good contact between the coaxial probe and the soft intestinal tissue, we used a designated 3D printed fixation clip (Fig. 3). The intestinal sample was slightly clamped between the clip and the probe surface.

Permittivity data analysis.   When applying microwaves to biological materials, two types of processes (energy storage and energy dissipation) take place. Polar molecules in the biological sample under test polarize in response to the applied alternating electric field causing energy storage and give rise to orientation polarization, where the dipoles orientate themselves to align with the externally applied field. The orientation polarization causes dielectric relaxations which is indicated by dispersions[22] in the dielectric properties. With fast alternating fields, the polar molecules cannot align with the field instantly which causes energy dissipation. Therefore complex permittivity is used to express the dielectric properties of the material as Equation 3 shows,

$$\epsilon^* = \epsilon' - j\epsilon'' = \epsilon' - j\frac{\sigma}{\epsilon_0 2\pi f}. \tag{3}$$

where the real and imaginary part of the complex permittivity ϵ', ϵ'' are called dielectric constant (energy storage) and dielectric loss (energy dissipation). σ is the dielectric conductivity which represents the energy loss associated with the dispersion of ϵ''. ϵ_0 is the vacuum permittivity.

Typically, the main contribution of the dielectric relaxation of water molecules can be described by a Debye function[33]. There will be a broadening of the spectrum which corresponds to a distribution of relaxation times, when other polar biological substances are present and interacts with water molecules. In the intestinal tissue, protein-bound water, proteins, metabolites in addition to different ion concentrations will contribute to the dielectric relaxation in addition to the water molecules[24,34,35].

In 1941, the Cole brothers introduced the Cole-Cole model[36] which corrects the Debye model to account for the distribution of relaxation times when used to describe dielectric relaxation of different materials. We used a symmetric Cole-Cole equation (4) to model the experimental permittivity data, to estimate the dielectric parameter values. Simultaneously, the Levenberg-Marquardt algorithm based non-linear least square method was used in the fitting procedure. A Python script implementing these algorithms was used to fit the experimental data,

$$\epsilon^*(\omega) = \epsilon_\infty + \frac{\Delta\epsilon_1}{1 + (j\omega\tau_1)^{1-\alpha_1}} + \frac{\Delta\epsilon_2}{1 + (j\omega\tau_2)^{1-\alpha_2}}. \tag{4}$$

where $\Delta\epsilon_1 = \epsilon_s - \epsilon_1$ and $\Delta\epsilon_2 = \epsilon_1 - \epsilon_\infty$ are the relaxation strength which is proportional to the area under the dielectric loss peak. τ_1 and τ_2 are the relaxation times, which provides an understanding of the intermolecular and the intramolecular motions and their relations to the molecule size and shape[37]. The parameters $\epsilon_\infty, \tau_1, \tau_2, \Delta\epsilon_1, \Delta\epsilon_2, \alpha_1, \alpha_2$ were obtained by fitting the Equation (4) to the experimental permittivity data.

Machine learning.   To make the surgical decision making process more automatic, recurrent neural networks (RNN) with long short-term memory (LSTM) units were used to train classifiers from the permittivity data[38]. Although conventionally used for time-series data, the sequential structure of the spectroscopic data also allows this ML architecture to be employed in learning patterns over frequencies. Three LSTM architectures were employed and built using Tensorflow.keras in Python: Unidirectional LSTM, bidirectional LSTM and residual bidirectional LSTM, all with three LSTM layers followed by a dense layer. All models included dropout and batch normalization for predictor standardization between the LSTM layers. In addition, we compared the performance of a 1D-CNN model with two convolutional layers followed by a max pooling and a dense layer, with that of the LSTM models. As our task can be viewed as a binary classification problem, we further tested two conventional methods, support vector machine (SVM) and random forest (RF) to investigate whether they can achieve similar performance as the deep learning methods.

Bidirectional LSTM was chosen because it enables learning of patterns in both sequential directions (low-frequency to high-frequency and opposite). Residual bidirectional LSTM has a residual connection between the LSTM cells which acts as highways for the gradients that pass the underlying information directly to the upper layer[39]. The input features from the previous layers have a parallel path that can learn additional non-linear functions and allow quick unlearning.

To address overfitting concerns, dropout and a fully connected hidden layer was added with the Ridge regularization, and we used nested cross-validation (CV). The selection of hyperparameters was done within an inner 5-fold CV loop, and prediction on the hold-out test data was done in an outer 5-fold CV loop. Within the inner loop, models with a different set of hyperparameters were tested against the inner validation dataset, and based on the accuracy achieved with the validation dataset in the inner loop, the model to be used for predicting on the test dataset in the outer CV loop was selected. 5-fold CV was selected also to avoid biased evaluation of the model performance as we use different data to tune the model hyperparameters and evaluate model performance.

To translate the probabilistic nature of the model into either ischemia duration less than 4 h (viable) or equal to and more than 4 h (non-viable) categories, a Softmax activation function was applied to the output layer. There were five hyperparameters applied to the LSTM network; learning rate η, regularization parameter λ, minibatch size, number of RNN units and Dropout as shown in Table 3.

The whole dataset was split into training data, validation data, and test data using the StratifiedKFold function of the Scikit-learn library, keeping the same proportion of classes within each fold during splits. 5-fold nested CV was used to select hyperparameters, the best model configurations, and to determine the mean accuracy, F1 score, sensitivity, and specificity on the test set.

Hyperparameter	Values
Learning rate η	$[10^{-6}, 10^{-5}, 10^{-4}, 10^{-3}, 10^{-2}]$
Regularization parameter λ	$[10^{-6}, 10^{-5}, 10^{-4}, 10^{-3}]$
Minibatch size	$[8, 16, 32, 64]$
RNN units	$[8, 16, 32, 64]$
Dropout	$[0.1, 0.2, 0.3]$[40]

Table 3. List of hyperparameters tested in LSTM network models.

Frequency contribution analysis. To analyze the contribution of different frequencies in the permittivity spectrum, principal component analysis (PCA) and the SHAP method in explainable AI were used. PCA was used to eliminate redundant frequencies in the permittivity data. Permittivity data from each measurement with 167 different frequency points was used as input to the PCA, where each of the frequencies in the permittivity spectrum was considered as one variable. The largest positive association from the two first principal components were extracted. Data was standardized using the scikitLearn StandardScaler function before performing PCA.

To extract the most influential variables from the otherwise unexplainable ML models, the SHAP method[14] was applied to explain how the model made its decisions. We used the SHAP method to visualize which of the frequencies that contribute positively and negatively to the model's classification decision. SHAP assigns each feature (frequency) an importance value for a particular model decision, and shapley values are attributed to each feature, explaining how to get from the base value to the current output[14]. The frequencies extracted from the SHAP method were compared with the frequencies that contributed the most in explaining the data variation extracted from the PCA.

References

1. Bulkley, G. B. *et al.* Intraoperative determination of small intestinal viability following ischemic injury: A prospective, controlled trial of two adjuvant methods (Doppler and fluorescein) compared with standard clinical judgment. *Ann. Surg.* **193**, 628–637 (1981).
2. Oldenburg, W. A., Lau, L. L., Rodenberg, T. J., Edmonds, H. J. & Burger, C. D. Acute mesenteric ischemia: A clinical review. *Arch. Intern. Med.* **164**, 1054–1062. https://doi.org/10.1001/archinte.164.10.1054 (2004).
3. Gabriel, S., Lau, R. W. & Gabriel, C. The dielectric properties of biological tissues: III. Parametric models for the dielectric spectrum of tissues. *Phys. Med. Biol.* **41**, 2271–2293. https://doi.org/10.1088/0031-9155/41/11/003 (1996).
4. Sasaki, K., Wake, K. & Watanabe, S. Development of best fit Cole–Cole parameters for measurement data from biological tissues and organs between 1 MHz and 20 GHz. *Radio Sci.* **49**, 459–472. https://doi.org/10.1002/2013RS005345 (2014).
5. Salahuddin, S., Porter, E., Krewer, F. & O' Halloran, M. Optimised analytical models of the dielectric properties of biological tissue. *Med. Eng. Phys.* **43**, 103–111. https://doi.org/10.1016/j.medengphy.2017.01.017 (2017).
6. Strand-Amundsen, R. J. *et al.* Ischemia/reperfusion injury in porcine intestine—Viability assessment. *World J. Gastroenterol.* **24**, 2009–2023. https://doi.org/10.3748/wjg.v24.i18.2009 (2018).
7. Strand-Amundsen, R. J. *et al.* In vivocharacterization of ischemic small intestine using bioimpedance measurements. *Physiol. Meas.* **37**, 257–275. https://doi.org/10.1088/0967-3334/37/2/257 (2016).
8. Hayashi, M. *et al.* Evaluation of ischemic damage in the skeletal muscle with the use of electrical properties. *J. Surg. Res.* **80**, 266–271. https://doi.org/10.1006/jsre.1998.5477 (1998).
9. Miyauchi, T. *et al.* Predictability of dielectric properties for ischemic injury of the skeletal muscle before reperfusion. *J. Surg. Res.* **86**, 79–88. https://doi.org/10.1006/jsre.1999.5676 (1999).
10. Sasaki, E., Hirose, H., Ito, H., Bando, M. & Senga, S. Dielectric spectrogram for instantaneous evaluation of ischemic injury of the liver. [Abstract]. Journal **41** (1995). Institution: From the First Department of Surgery, Gifu University School of Medicine, Gifu, Japan.
11. Yamada, T. *et al.* An experimental estimation of the maximum period of liver preservation using dielectric parameters. *Transpl. Proc.* **34**, 1098–1104. https://doi.org/10.1016/S0041-1345(02)02785-9 (2002).
12. Foster, K. & Schwan, H. Dielectric properties of tissues and biological materials: A critical review. *Crit. Rev. Biomed. Eng.* **17**, 25–104 (1989).
13. Matsuo, H. *et al.* Experimental studies to estimate the intestinal viability in a rat strangulated ileus model using a dielectric parameter. *Dig. Dis. Sci.* **49**, 633–638. https://doi.org/10.1023/B:DDAS.0000026310.71607.4c (2004).
14. Lundberg, S. & Lee, S.-I. A unified approach to interpreting model predictions. arXiv:1705.07874 [cs, stat] (2017).
15. Douglas, W. R. Of pigs and men and research. *Space Life Sci.* **3**, 226–234. https://doi.org/10.1007/BF00928167 (1972).
16. Yandza, T. *et al.* The pig as a preclinical model for intestinal ischemia-reperfusion and transplantation studies. *J. Surg. Res.* **178**, 807–819. https://doi.org/10.1016/j.jss.2012.07.025 (2012).
17. Gonzalez, L. M., Moeser, A. J. & Blikslager, A. T. Animal models of ischemia-reperfusion-induced intestinal injury: progress and promise for translational research. Am. J. Physiol. Gastrointest. Liver Physiol. **308**, G63–G75. https://doi.org/10.1152/ajpgi.00112.2013 (2014).
18. Strand-Amundsen, R. J. *et al.* Machine learning for intraoperative prediction of viability in ischemic small intestine. Physiol. Meas. **39**, 105011. https://doi.org/10.1088/1361-6579/aae0ea (2018).
19. Otte, S. *et al.* OCT A-Scan based lung tumor tissue classification with Bidirectional Long Short Term Memory networks. In 2013 IEEE International Workshop on Machine Learning for Signal Processing (MLSP), 1–6, https://doi.org/10.1109/MLSP.2013.6661944 (2013). ISSN: 2378-928X.
20. Strand-Amundsen, R. J. *et al.* Small intestinal ischemia and reperfusion-bioimpedance measurements. *Physiol. Meas.* **39**, 025001. https://doi.org/10.1088/1361-6579/aaa576 (2018).

9

77

21. Hahn, G. M. *et al.* Some heat transfer problems associated with heating by ultrasound, microwaves, or radio frequency. *Ann. N. Y. Acad. Sci.* **335**, 327–351. https://doi.org/10.1111/j.1749-6632.1980.tb50757.x (1980).
22. Nasir, N. & Al Ahmad, M. Cells electrical Characterization: Dielectric properties, mixture, and modeling theories. *J. Eng.* **2020**, e9475490. https://doi.org/10.1155/2020/9475490 (2020).
23. Kalogeris, T., Baines, C. P., Krenz, M. & Korthuis, R. J. Cell biology of ischemia/reperfusion injury. *Int. Rev. Cell Mol. Biol.* **298**, 229–317. https://doi.org/10.1016/B978-0-12-394309-5.00006-7 (2012).
24. Pethig, R. Dielectric properties of body tissues. *Clin. Phys. Physiol. Meas.* **8**, 5–12. https://doi.org/10.1088/0143-0815/8/4A/002 (1987).
25. Schwan, H. P. & Foster, K. Microwave dielectric properties of tissue. Some comments on the rotational mobility of tissue water. *Biophys. J.* **17**, 193–197. https://doi.org/10.1016/S0006-3495(77)85637-3 (1977).
26. Polk, C. CRC Handbook of Biological Effects of Electromagnetic Fields (CRC Press, 2019). Google-Books-ID: 3TSoDwAAQBAJ.
27. Kim, J., El-Khamy, M. & Lee, J. Residual LSTM: Design of a deep recurrent architecture for distant speech recognition. arXiv:1701.03360 [cs] (2017).
28. Cawley, G. C. & Talbot, N. L. on over-fitting in model selection and subsequent selection bias in performance evaluation. *J. Mach. Learn. Res.* **11**, 2079–2107 (2010).
29. Strand-Amundsen, R. J. *et al.* Ischemic small intestine-in vivoversusex vivobioimpedance measurements. *Physiol. Meas.* **38**, 715–728. https://doi.org/10.1088/1361-6579/aa67b7 (2017).
30. Gregory, A. P. & Clarke, R. N. Dielectric metrology with coaxial sensors. *Meas. Sci. Technol.* **18**, 1372–1386. https://doi.org/10.1088/0957-0233/18/5/026 (2007).
31. Kaatze, U. Complex permittivity of water as a function of frequency and temperature. *J. Chem. Eng. Data* **34**, 371–374. https://doi.org/10.1021/je00058a001 (1989).
32. Ellison, W. J. Permittivity of pure water, at standard atmospheric pressure, over the frequency range 0–25 THz and the temperature range $0 - 100°$ C. *J. Phys. Chem. Ref. Data* **36**, 1–18. https://doi.org/10.1063/1.2360986 (2007).
33. Debye, P. J. W. Polar Molecules (New York, 1929).
34. Schwan, H. P. Electrical properties of tissues and cell suspensions: mechanisms and models. In Proceedings of 16th Annual International Conference of the IEEE Engineering in Medicine and Biology Society, vol. 1, A70–A71 vol.1, https://doi.org/10.1109/IEMBS.1994.412155 (1994).
35. Liewei Sha, Ward, E. R. & Stroy, B. A review of dielectric properties of normal and malignant breast tissue. In Proceedings IEEE SoutheastCon 2002 (Cat. No.02CH37283), 457–462, https://doi.org/10.1109/SECON.2002.995639 (2002).
36. Cole, K. S. & Cole, R. H. Dispersion and absorption in dielectrics I. Alternating current characteristics. *J. Chem. Phys.* **9**, 341–351. https://doi.org/10.1063/1.1750906 (1941).
37. Ottosson, N., Pastorczak, M., van der Post, S. T. & Bakker, H. J. Conformation of the neurotransmitter γ-aminobutyric acid in liquid water. *Phys. Chem. Chem. Phys.* **16**, 10433–10437. https://doi.org/10.1039/C4CP00671B (2014).
38. Hochreiter, S. & Schmidhuber, J. Long short-term memory. *Neural Comput.* **9**, 1735–1780. https://doi.org/10.1162/neco.1997.9.8.1735 (1997).
39. Zhao, Y., Yang, R., Chevalier, G. & Gong, M. Deep Residual Bidir-LSTM for Human Activity Recognition Using Wearable Sensors. arXiv:1708.08989 [cs] (2017).
40. Cheng, G. *et al.* An exploration of dropout with lstms. In Interspeech, 1586–1590 (2017).

Acknowledgements

Author contributions

Data collection, J.H.; formal analysis, J.H.; conceptualization, J.H., R.S.A., T.I.T; methodology, J.H., C.T., R.S.A. and Ø.G.M.; Writing the original draft, J.H.; supervision, R.S.A, C.T., T.I.T. J.O.H. and Ø.G.M. writing-review, J.H., R.S.A., C.T, T.I.T, J.O.H., and Ø.G.M.; All authors have read and agreed to the published version of the manuscript.

Competing interests

The authors declare no competing interests.

Additional information

Supplementary information is available for this paper at https://doi.org/10.1038/s41598-022-07140-4.

Correspondence and requests for materials should be addressed to J.H.

Reprints and permissions information is available at www.nature.com/reprints.

Publisher's note Springer Nature remains neutral with regard to jurisdictional claims in published maps and institutional affiliations.

Paper II

Automatic Prediction of Ischemia-Reperfusion Injury of Small Intestine Using Convolutional Neural Networks: A Pilot Study

Jie Hou, Runar Strand-Amundsen, Christian Tronstad, Jan Olav Høgetveit, Ørjan Grøttem Martinsen, Tor Inge Tønnessen

II

Article

Automatic Prediction of Ischemia-Reperfusion Injury of Small Intestine Using Convolutional Neural Networks: A Pilot Study

Jie Hou [1,2] , **Runar Strand-Amundsen** [2], **Christian Tronstad** [2], **Jan Olav Høgetveit** [1,2], **Ørjan Grøttem Martinsen** [1,2,*] **and Tor Inge Tønnessen** [3,4]

1. Department of Physics, University of Oslo, Sem Sælands vei 24, 0371 Oslo, Norway; jieho@fys.uio.no (J.H.); jhogetve@ous-hf.no (J.O.H.)
2. Department of Clinical and Biomedical Engineering, Oslo University Hospital, 0372 Oslo, Norway; runar@sensocure.no (R.S.-A.); chrton@ous-hf.no (C.T.)
3. Department of Emergencies and Critical Care, Oslo University Hospital, 0424 Oslo, Norway; t.i.tonnessen@medisin.uio.no
4. Institute of Clinical Medicine, University of Oslo, 0424 Oslo, Norway
* Correspondence: ogm@fys.uio.no

Abstract: Acute intestinal ischemia is a life-threatening condition. The current gold standard, with evaluation based on visual and tactile sensation, has low specificity. In this study, we explore the feasibility of using machine learning models on images of the intestine, to assess small intestinal viability. A digital microscope was used to acquire images of the jejunum in 10 pigs. Ischemic segments were created by local clamping (approximately 30 cm in width) of small arteries and veins in the mesentery and reperfusion was initiated by releasing the clamps. A series of images were acquired once an hour on the surface of each of the segments. The convolutional neural network (CNN) has previously been used to classify medical images, while knowledge is lacking whether CNNs have potential to classify ischemia-reperfusion injury on the small intestine. We compared how different deep learning models perform for this task. Moreover, the Shapley additive explanations (SHAP) method within explainable artificial intelligence (AI) was used to identify features that the model utilizes as important in classification of different ischemic injury degrees. To be able to assess to what extent we can trust our deep learning model decisions is critical in a clinical setting. A probabilistic model Bayesian CNN was implemented to estimate the model uncertainty which provides a confidence measure of our model decisions.

Keywords: convolutional neural networks (CNN); small intestinal viability; ischemia-reperfusion injury; explainable AI; transfer learning; probabilistic modeling; decision-level fusion

1. Introduction

Acute intestinal ischemia is a serious condition with a high mortality rate, where rapid diagnosis and treatment are of crucial importance [1,2]. With a positive diagnosis, the goal of the acute surgery is to assess the small intestine, restore blood flow, and resect segments that appear to be non-viable while leaving the intestinal segments that will ultimately survive [1]. Diagnosing intestinal ischemia intra-operatively is difficult, especially in circumstances where the bowel appears to be in the borderline between ischemic and non-ischemic [1].

The standard clinical method for evaluation of intestinal viability is still visual inspection and palpation. The estimation of tissue state can be based on color change, presence of visible peristalsis and bleeding from cut edges [1–5]. This method is non-specific and often unreliable. Viable tissue might be removed or more importantly, irreversibly injured tissue might be left in the patient, which may lead to complications and slow down the patient's recovery. For standard clinical estimation of bowel viability, reports have been made of accuracy in the range of 78% to 89% , but this typically includes resection

81

of viable bowel and second-look procedures [5,6]. Patients may risk short gut syndrome if resection is performed too aggressively. Techniques, such as anti-mesenteric Doppler interrogation and intravenous fluorescein dye, have been used experimentally. However, none of these techniques have proven to be reliable in predicting future viability of the small intestine [2]. Due to the potential inaccuracy of the early evaluation of intestinal viability following ischemia-reperfusion injury, a second-look operation, 24–48 h after the first surgery, is often required [1,2]. Prolonged or repeated surgery increases the amount of surgical stress and the risk for infection. A quick and accurate technique for intraoperative evaluation of intestinal viability could reduce the need for second-look operations and the time needed for evaluation.

CNN is a well-known deep learning model for image analysis and classification. In this study, we investigated four different CNN architectures; traditional CNN, CNN with decision-level fusion, Bayesian CNN, and transfer learning using ResNet50 [7]. Decision-level fusion CNN was chosen as fusing multiple image datasets enhances the classification confidence and reduces ambiguity and uncertainty. Moreover, since the traditional CNN architecture does not offer information about how trust-worthy the model is, i.e., uncertainty in its predictions or decisions, we further chose to apply a probabilistic model, Bayesian CNN architecture, which has the ability to quantify the model's reliability. In a clinical setting, not only does the diagnostic process by machine learning models have to be extremely accurate, but knowing to what extend we can trust our model decisions is also crucial. The chosen Bayesian CNN architecture is robust to over-fitting and at the same time offers a probabilistic interpretation of the model by inferring distributions over the model's weights [8]. We also explored the possibility of using transfer learning, where a developed model based on one task is reused as the starting point for a model with a similar dataset and task. We chose ResNet50, as this network has learned rich feature representations for a wide range of images, which can be of advantage for our task.

In addition to the machine learning models, two parameters from image analysis were also explored to quantify changes of properties in the images during ischemia and reperfusion. Namely, contrast for the red channel and entropy of the images. The results were further compared with the explainable AI Shapley additive explanations (SHAP) method, which is an approach to explain the output of any machine learning model [9]. This is demonstrated by highlighting pixels on the small intestine images to reveal which areas that contribute positively and negatively to the correct classification.

To the best of our knowledge, no previous studies have been conducted to investigate whether microscopic images taken from the surface of the intestinal tissue, combined with deep learning, can be used as a non-invasive method to evaluate the viability of the small intestine. The closest "state of the art" works, which use machine learning to assess diagnosis of gastrointestinal diseases, are multi-class image and video datasets for gastrointestinal endoscopy [10]. They demonstrated the potential benefits of AI-based computer-assisted diagnostic systems. In the same year, Yan et al. [11] used CNN and transfer learning in diagnosing gastric intestinal metaplasia with a limited number of images. In our study, we propose a fast and non-invasive method to assess small intestinal viability. We aim to investigate the use of images combined with deep learning algorithms to automatically evaluate the intestinal viability with millimeter precision during surgery.

2. Methods

2.1. Animals and Experimental Design

This study was conducted using ten Norwegian Landrace pigs, weight range 50 to 66 kg. Food was withheld 12 h prior to surgery. We used the same experimental protocol as Strand-Amundsen et al. [12]. For each pig, we created 4 segments with local ischemia on the jejunum, by clamping the arteries and veins of a segment of the jejunal mesentery. The result was a 30 cm central zone of warm ischemia and two surrounding edge zones of marginal tissue hypoxia. Images were acquired over an eight hours period. The 4 segments in each pig were used to create 4 different cases; case A: control 8 h; case B: 8 h ischemia; case C:

3 h ischemia followed by 5 h reperfusion; case D: 4 h ischemia followed by 4 h reperfusion. Images were taken once an hour. After the experiment, the animals were sacrificed by a lethal dose of potassium chloride (100 mmol).

2.2. Surgery, Anaesthesia, and Monitoring

Prior to surgery, the pigs were sedated by an intramuscular injection consisting of ketamine (40 mg/kg), atropine (0.05 mg/kg), and droperidole (0.65 mg/kg). During surgery, anesthesia was maintained with isoflurane (Abbott Scandinavia AB, Kista, Sweden) (1–1.5%) and a mixture of air and O_2 to obtain an FiO_2 of 30%. Morphine (Alpharma, Oslo, Norway) 0.4–0.7 mg/kg/h was administered as a continuous intravenous infusion. Surgery was performed under sterile conditions. The jejunum was made accessible through midline laparotomy in the abdominal cavity. A continuous infusion of Ringer acetate 10–30 mL/kg/h was administered through the jugular vein as fluid replacement [12].

2.3. Image Acquisition

A handheld Dino-lite USB digital microscope camera (model AM7013MZT from Dino-lite) with a controlled built-in light source was used to acquire images of the small intestine surface. To ensure that all images were taken under the same light conditions, a 3D printed black enclosure was used to limit external lights from influencing the area of interest. A series of images were taken at different locations of all 4 segments once an hour. Around 50 images were taken from each of the segments by moving the camera slightly after each image, resulting in 200 images per hour and 1600 images for each experiment. The total number of images acquired from 10 pigs was 17,330, divided into 18 classes based on one hour interval as shown in Figure 1.
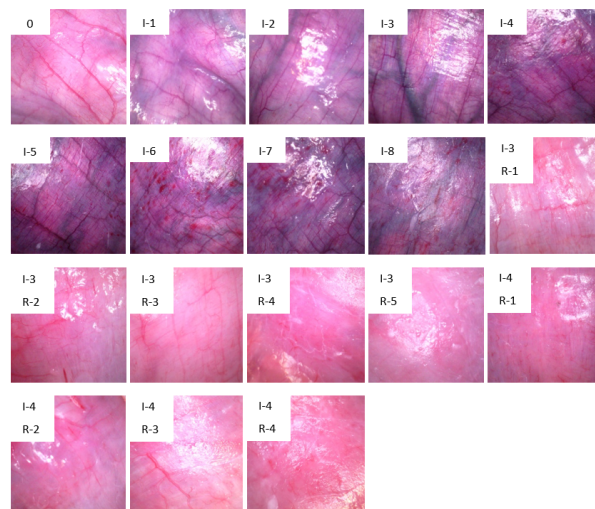
Figure 1. Images of the jejunum at selected intervals of ischemia and reperfusion. 0: healthy jejunum at the start of the experiment. "I" = Ischemia and "R" = Reperfusion, numbers are duration hours. Each of these 18 images represents distinct time duration's that we use as classes in the CNNs.

2.4. Image Preprocessing

The acquired images are of size 2592 × 1944 pixels. As a part of the image preprocessing process, the edges of the images were first cropped automatically using the function "PIL.Image.crop()" from the Python Imaging Library [13] to eliminate background noise, to a new size of 1500 × 1400 pixels. To allow the 17,330 images to be of a manageable size relative to available computer memory, the images were further downsized to an

image size of 224 × 224 pixels, while still retaining enough information, and to match the acceptable image size for the ResNet50 network.

After cropping the image edges and resizing them, the StandardScaler algorithm was implemented by:

$$z = \frac{x - \mu}{\sigma} \tag{1}$$

where μ is the mean and σ is the standard deviation. Normalizing the training data to having mean 0 and variance 1 along the features can often improve convergence during gradient descent, since it will avoid many extra iterations that are required if one or more features have much larger values than the rest.

2.5. Entropy and Contrast Analysis

In order to investigate different image properties, we derived descriptive statistics for image entropy, contrast, dissimilarity, homogeneity, energy, and correlation. Among the properties investigated, the largest changes were found for entropy and contrast, and the development in these parameters during ischemia and reperfusion are presented statistically.

Shannon entropy [14] was calculated for each of the images, which is a direct measure of the number of bits needed to store the information in a variable, as opposed to its raw data. Thus, it is a measure of "amount of information" contained in an image [15]. Entropy is also a statistical measure of randomness and uncertainty and can be used to characterize the texture of the images where more detailed images give higher entropy. Shannon entropy measured in bits is defined as:

$$H(X) = -\sum_{i=i}^{N} P(x_i)\log_2(P(x_i)) \tag{2}$$

where X is a discrete random variable, $P(x_i)$ are probability of the possible outcomes x_i, and $\log_2$ gives the unit of bits.

For image contrast analysis, we extracted the red channel from the RGB images, as red is the dominant color for the small intestinal tissue. The co-occurrence matrix [16] is needed to calculate the contrast, which is computed as a histogram of co-occurring red channel values at a given offset, representing how often pairs of pixels with a specific value and offset occur in an image. One pixel was used as pixel pair distance offset and zero radian was used for the pixel pair angles. By using the co-occurrence matrix, the contrast is computed by:

$$\text{contrast} = \sum_i \sum_j G_{i,j}(i - j)^2 \tag{3}$$

where $G_{i,j}$ is the ith row and jth column element in the co-occurrence matrix G.

2.6. CNN Architecture

CNN was chosen due to its excellent performance in image analysis, and the ability to automatically extract features, allowing for accurate differentiation between images. Through the convolutional layers, convolution is applied on the input image with kernels, making it possible to capture the spatial features of the images, resulting in feature maps. The pooling layers reduce the size of the data output so that it is easier to process further [17]. The last dense layer performs the final classification in the CNN model; in our case, there are 18 classes, "0" to "17" corresponding to "0" to "I-4, R-4", as shown in Figure 1.

Deciding which CNN architecture performs best can be difficult, as the performance depends on the input data and the problem we seek to solve. Hence, to find the best fit for our task, we explored a few possible structures; traditional sequential CNN, decision-level fusion CNN, Bayesian CNN and ResNet50 designed by He et al. [7]. All the CNN architectures were built using Keras [18] TensorFlow as a back-end, all training were

performed for 100 epochs, and Adam was used to minimize the cross-entropy loss. The traditional CNN architecture used is as follows:

Parameters used in the CNN architecture, described in Figure 2, are shown below:

- A kernel size of 3, padding "same" and l2 kernel regularizer were used for each of the convolutional layers. Hyperparemeter l2 values tested: $10^{-3}, 10^{-4}, 10^{-5}$;
- Max pooling layer of size 2 was used;
- Hyperparameter dropout values tested: 0.1, 0.2, 0.3;
- Activation function "RELU" was used for both the convolutional and the fully connected layers;
- The "Softmax" activation function was used for the last classification layer, with 18 units corresponding to the 18 classes.
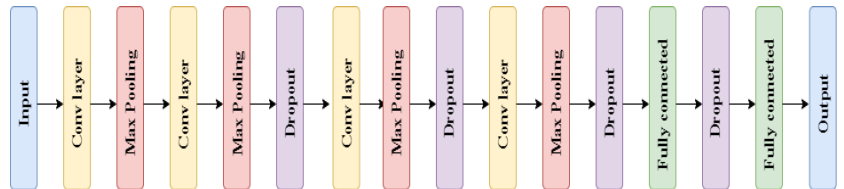
Figure 2. CNN architecture.

The number of units for the convolutional layers were multiplied by 1, 2, 3, 4 for the 4 convolutional layers, where the initial number of units tested was: 16, 32, 64, 128, respectively. During the training, batch sizes of 32, 64, 128 were evaluated and learning rate values of 0.001 and 0.0001 were tested.

In addition to the traditional CNN architecture in Figure 2, we created and tested a decision-level fusion framework for this multi-class classification task (Figure 3). Instead of having one input dataset, we created two additional datasets, namely histogram of oriented gradients (HOG) and local binary patterns (LBP).

Figure 3. Block diagrams of decision-level fusion and CNN architecture involved.

HOG has been widely used in computer vision and object detection. It counts occurrences of gradient direction in a local portion of an image. HOG computes the

gradient values, the gradients mainly appears at the edge of different tissue structures. The gradient direction may contain information ab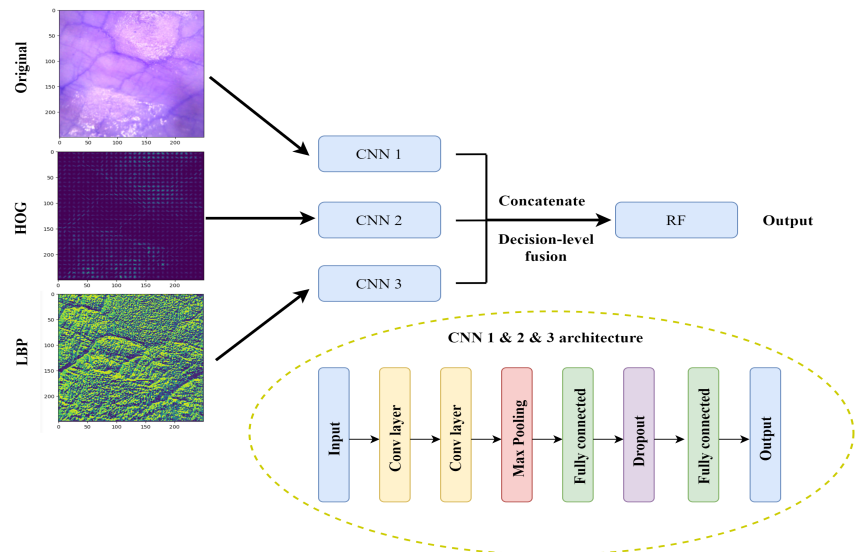out the blood vessels and surface structures on the small intestine. The decision-level fusion model supplemented the features extracted from the original RGB images and the HOG features to obtain a more accurate extraction of edge information. The extraction of HOG features are described in Algorithm 1.

Algorithm 1: HOG feature extraction.

Input: Image dataset with RGB colors.
Step 1: Compute the gradient of each pixel of the image, number of orientation bins used was 9.
Step 2: Divide the images into cells, 8×8 pixels form a cell, and compute gradient histograms of each cell.
Step 3: 2×2 cells form a block, and normalize gradient histograms across blocks.
Step 4: The feature descriptors of all blocks are then flattened into a feature vector.
Output: HOG features.

LBP is a powerful feature for texture classification. Earlier studies determined that combining LBP with HOG improves the detection performance considerably on some datasets [19]. The ability in extracting the texture feature enhances the information going into the model. Algorithm 2 describes the LBP feature extraction process.

Algorithm 2: LBP feature extraction.

Input: Image dataset with RGB colors.
Step 1: Convert the RGB images to grayscale images.
Step 2: Set parameter number of circularly symmetric neighbour points to 8.
Step 3: Set parameter radius of circle to 1.
Step 4: Calculate the LBP feature.
Output: LBP features.

Both HOG and LBP feature extraction were performed using the Scikit-image (skimage) library [20] in Python. The final decision-level fusion model is composed of three CNN architectures with the original RGB images, HOG images, and LBP images, as respective inputs. All three image representations were trained individually in separate CNN architectures, resulting in a combination of color, edge, texture, and local structure feature collection. Moreover, they were classified individually based on the different features extracted and the classification probability distributions were then concatenated together. The parameters used and hyperparameters tested for the architecture described in Figure 3 were the same as for the traditional CNN architecture described earlier. Furthermore, conventional classifier random forest (RF) [21] were chosen to perform the final classification. The number of trees in the forest tested was 100 and 300.

The pretrained model ResNet50 was imported from Keras application library [18], and all layers except the last block were used directly without any modifications. The last block was kept trainable in order to fine-tune the model to learn from our dataset. A global average pooling layer was added to the end of the ResNet50 model to connect the dimensions of the previous layers with the new layers. One dense layer was added after the pooling layer with dropout 0.2 before the final classification.

Data augmentation was applied for all models to increase the diversity of the dataset without having to collect more images, helping to improve the model performance and prevent the model from over-fitting. The "ImageDataGenerator" from the Scikit-learn library [22] was used to perform real-time image data augmentation. For each of the input training images, rotation (20 degrees), zoom (ranging from 90% to 110%), horizontal and vertical flip were randomly applied.

The number of images in each of the classes are unequal and the control class contains more images than the other classes. To adjust for possible bias from the unbalanced dataset,

class weights were calculated and applied to all models to account for the skewed distribution of the classes. Weights were computed by $n_{samples}/(n_{classes} * n_{samples\ in\ a\ certain\ class})$. By including balanced class weight, the weights were increased for the minority classes and decreased for the majority classes.

2.7. Bayesian CNN Architecture

The library Tensorflow-probability [23] was used to implement the Bayesian CNN architecture. Compared to the standard CNN architecture described above, the following modifications were made to take both aleatoric uncertainty (statistical uncertainty) from the data and epistemic uncertainty (systematic uncertainty) of the model into account.

Instead of normal 2D convolution and dense layers, 2D convolution and dense layers with reparameterization were used, which creates an output that is drawn from a Gaussian distribution. The function that calculates the outputs uses a reparameterization estimator, which performs a Monte Carlo approximation of the distribution integrating over the kernel and bias [24]. For each replacement of the Conv2D layer with the 2D convolution reparameterization layer, there is a doubling of the number of parameters. The doubling is due to the replacement of the weight of parameters from a single value into a value that is drawn from a normal distribution with two parameters, namely, the mean and the standard deviation.

Negative log-likelihood was used as the loss function instead of categorical cross entropy, to maximize the likelihood estimate of the mean and standard deviation of the weights. We tried to maximize the probability of choosing a correct class by minimizing the negative log-likelihood, where we find lower loss with better model predictions.

To evaluate the model, several predictions were made on each of the test images instead of only once, as we did with the standard CNN architecture. A total of 300 predictions for each image were chosen for this model. From the predictions, a prediction probability distribution was created for each of the test images. One important aspect of Bayesian CNN is the output uncertainty of the model prediction. We studied the mean and the 95% confidence interval for the certainty of correct classification of the 18 classes.

2.8. Model Evaluation Metrics

Accuracy, precision, and recall were used to determine the performance of the model. Accuracy is the ratio of correctly predicted images to the total test images. For all models, the total image data were split into training, validation and test dataset by 60%, 20%, and 20%. Function "train_test_split" from Scikit-learn library [22] was used to randomly split the dataset. The total dataset was shuffled before splitting. Macro-averages were used in calculation of the precision and recall scores, where the metrics were calculated independently for each class before averages were calculated. The overall accuracy, precision and recall were determined as follows:

$$\text{Accuracy} = \frac{\text{TP} + \text{TN}}{\text{TP} + \text{FP} + \text{FN} + \text{TN}}$$

where the model performance depends on true positives (TP), true negatives (TN), false positives (FP), and false negatives (TN).

$$\text{Precision} = \frac{\text{TP}}{\text{TP} + \text{FP}} \qquad \text{Recall} = \frac{\text{TP}}{\text{TP} + \text{FN}}$$

where precision is the probability of a positive test given that the image belongs to a specific class (images that were correctly classified as positive out of all positives) and recall is the probability of a negative test given that the image does not belong to a specific class.

2.9. Explainable AI—Shapley Additive Explanations (SHAP) Method

SHAP assigns each pixel of the image an importance value (Shapley value) for a particular decision, explaining how to change from the base value that would be predicted

if no features were known, to the current output [9]. A pixel having a positive Shapley value indicates that the specific pixel contributes positively to the correct classification. From the distribution of Shapley values, we obtain an understanding of how different areas of the small intestine contributes to the classification.

3. Results

A total of 10 pigs were used in this study. As expected, there are considerably overlap between the different classes on both entropy and contrast. As shown in Figure 4a, the overall entropy is higher for all ischemia cases compared to the control and the reperfusion cases, where they appear to have a greater degree of disorder and thus appear to contain more "information". The entropy is then reversed by the onset of reperfusion, where all reperfusion cases after three hours of ischemia seems to have a better reversal than reperfusion after four hours. This observation associates with findings from an earlier study suggesting that three hours of full ischemia followed by reperfusion is the upper limit for viability in the porcine intestinal ischemia model [25]. Moreover, there appears to be a clear separation between classes 10–14 (three hours ischemia followed by five hours reperfusion) and classes 15–18 (four hours ischemia followed by four hours reperfusion).
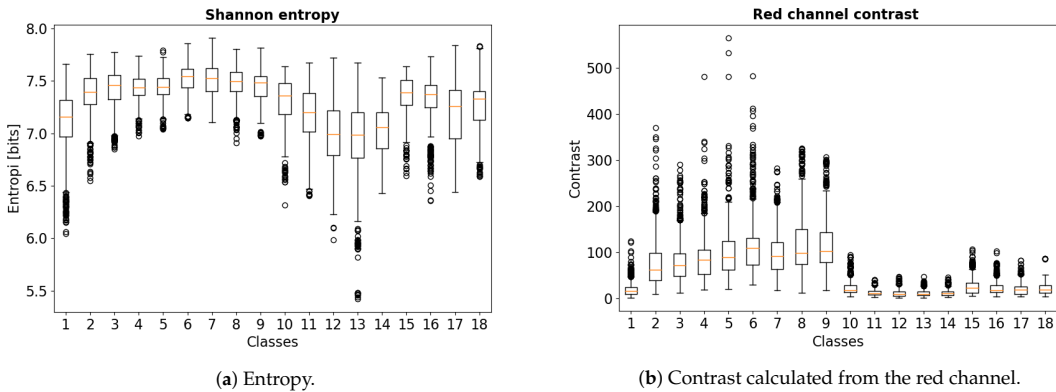

(**a**) Entropy. (**b**) Contrast calculated from the red channel.

Figure 4. Boxplot of calculated Shannon entropy and red channel contrast values.

As shown in Figure 4b, the contrast of the red channel had higher values in all the ischemia cases. The intestinal segments subjected to three hours of ischemia followed by five hours of reperfusion showed an overall lower contrast. The difference between classes 10–14 and classes 15–18 is also clear in the analysis of contrast.

As a baseline classification, a traditional CNN architecture was implemented. The architecture is shown in Figure 2, where the original RGB images alone were used as the model input. To evaluate whether a decision-level fusion approach could achieve better performance than the traditional CNN model, original RGB images combined with HOG and LBP images as the model input were evaluated. Single representations of the three image datasets were trained using separate CNN architectures, and the results of these three CNN classifiers were then concatenated and fed into a RF classifier, as shown in Figure 3. Figure 5 compares the performance from the test dataset of different models. ResNet50 outperformed all other models with an average accuracy of 98.12%, followed by the Bayesian CNN and CNN with decision-level fusion with an average accuracy of 97.76% and 97.57%, respectively. The traditional CNN model only achieved an accuracy of 90.20%.
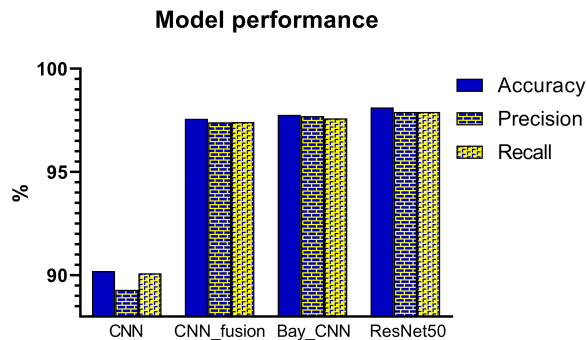
Model performance

Figure 5. Model performance of the test dataset for 18 classes classification of different ischemia-reperfusion injury degrees of the small intestine.

The implementation of Bayesian CNN gives us the possibility to quantify the uncertainty of the model. Consider one input image, which has been classified to class "10" with a probability of 99%, but the uncertainty could also be as high as 10%, therefore, we cannot fully trust the model performance without uncertainty measurements. To evaluate the model uncertainty, we show the mean and the average 95% confidence interval for model prediction certainty in Figure 6.
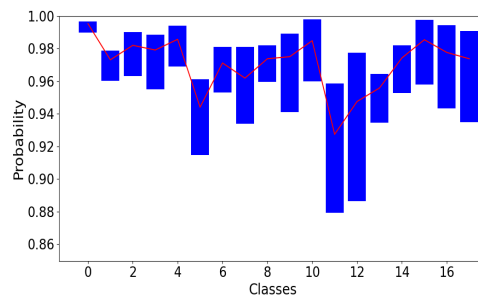

Figure 6. The 95% confidence interval for correctly predicted images together with the mean. The upper limit is the average value of 97.5th percentile, and the lower limit is the average value of the 2.5th percentile averaged over 300 predictions and all test images in the same class. Confidence interval for prediction probability for the 18 classes. Classes "0" to "17" corresponds to "0" to "I-4, R-4" in Figure 1.

The model predicts each of the test images 300 times instead of just once. Of the 300 predictions, in one run the model may predict an image as class 11 with almost 96% probability, in another run, it may predict the same image with only 89% probability. Those classes with wide 95% confidence intervals and lower values are those the model struggles with predicting correctly with high certainty.

Figure 7 shows the output from the SHAP method, where it attempts to explain the model decisions by highlighting different pixels on the image. Red pixels represent positive Shapley values, which contribute to increase the possibility of being classified to the correct corresponding class. Blue pixels represent negative Shapley values that reduce the probability of being classified to the correct class. The colored images on the left side of Figure 7 are the original images. The correct classes for the three example images are: class 18, 6, and 11. The grey images in each row represent the 18 classes. All three images were correctly classified, as we can see from the first row, the 18th grey image (corresponding to class 18—4 h ischemia followed by 4 h reperfusion) had the largest positive contribution,

the red color marked areas correspond to the same areas on the original image. From Figure 7, we are not only seeing which areas on the small intestine images contributed positively and negatively, we can also see which classes are similar to the target correct class, where some areas also contribute positively but not as much. Images with similar injuries look similar, SHAP outputs show where on the image does the model utilize as important features, providing a method in verifying that our model did not consider undesirable noise features as important basis for classification.
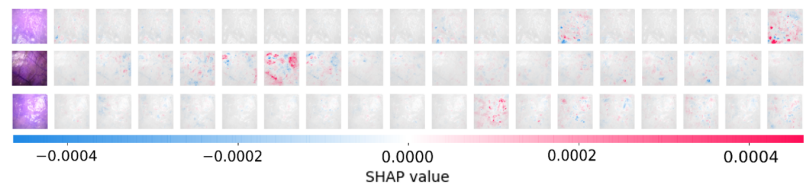
Figure 7. Visualization of positive and negative contributions to the classification by the SHAP method. The three images belong to classes 18, 6, and 11, respectively.

4. Discussions

By combining microscopic images from intestinal segments in a pig model of mesenteric ischemia-reperfusion with machine learning models, we were able to detect whether the segments were ischemic or reperfused, and could also assess how long the segments had been ischemic or reperfused, with a high accuracy.

This addresses the well known challenge of viability assessment and selection of resection margins following ischemia-reperfusion in the intestines. The standard clinical methods to decide which parts should be resected can require waiting for up to 48 h for a second look surgery, and uncertainty can be high. When fully perfused or fully necrotic, the intestine can be easy to identify by visual inspection, reperfused or partially reperfused intestine with return of color and movement can be harder to assess with respect to viability [25]. Accordingly, there is a high medical need for methods that can accurately predict intestinal viability after ischemia-reperfusion injury.

The method of using surface images together with machine learning is fast, easy-to-use, and can potentially be used as a tool to assist the surgeon with decision-making during surgery. As the intestinal wall is thin and some of the intestinal layers are semi-transparent, visual light contains information not only about the serosal surface, but of the subserosa and muscularis, as well as distribution and size of blood vessels in these layers. We chose to investigate both ischemia and reperfusion, as intestinal injury is caused not only by ischemia but that injury is aggravated following reperfusion [26–28].

Transfer learning using ResNet50 achieved an accuracy of 98.12%. This model architecture has the largest number of layers, and it was pre-trained on a dataset containing one million images [7]. ResNet50 showed a very good ability in both capturing the features and generalizing itself on our dataset. In addition, the skip connections allow alternate shortcut paths for gradient to flow through, which greatly reduce the risk for the vanishing gradient problem [29]. For clinical questions involving medical images, transfer learning is worth exploring, since it is both time saving and has less demand for training on a large dataset. This can be of a great advantage when working with medical images, as collecting data from patients can be challenging and time-consuming.

Deep learning models lack transparency and can sometimes be difficult to trust. Probability theory can be adopted to express uncertainty and noise associated with the model, and inverse probability allows us to infer unknown quantities. Bayes rule informs us how to perform inference about hypotheses from our dataset and help us to analyze the model prediction uncertainty [30]. The key difference between a standard CNN and a Bayesian CNN is that the weight and biases in the network has a probability distribution attached to them instead of a single deterministic value representing the weight and bias. For each of the images classified, we run through the prediction several times, which

gives us multiple output values. From the output values, we can find the uncertainty and confidence intervals. With low-quality, noisy images or images that are completely different from the rest, the output will have a more "uniform-like" distribution, which could be interpreted as high uncertainty as the model classifies the same image to a different class each time. High-quality images combined with a well-trained model would give us the same prediction of the true class, as the model tends to draw the same conclusion each time on the same image. This could be interpreted as the model being able to extract the real features which contributes positively to the correct classification. Ultimately, the Bayesian CNN achieved the second best performance while providing uncertainty measurements. These reveals how confident the model is when assigning a probability value to a certain class.

As shown in Figure 6, the overall prediction certainty agrees with what we see from the images, for example, those classes which represent ischemia followed by reperfusion are more difficult to distinguish from one another. As we can see from Figure 6, class 11 and 12 corresponding to 3 h ischemia followed by 3 and 4 h reperfusion, had the lowest mean certainty and widest confidence interval.

CNN with decision-level fusion using three different image representations fell to the third place in performance. Merging different image representations and training them in separate CNN models allow for more specific and accurate extraction of features, leading to a better result compared to the conventional CNN model.

It can be challenging to understand how the machine learning models arrive at the output classification decision. Machine learning algorithms are becoming more and more complex, with increasing numbers of layers in a single model [31]. The result can be black-box models where the interpretations of the relation between different variables can be challenging to explain [32]. This is known as the interpretability problem [33]. In order to address this problem, we explored several explainable AI methods, including SHAP [9], gradient-weighted class activation mapping (GradCam), local interpretable model-agnostic explanations (LIME), and explain it like I am 5 (Eli5). The SHAP method was found to be the most suitable and best-performing method for our dataset. Therefore, the SHAP method was applied in order to explain how the decisions were made by the model.

Accompanying the CNN performance, one of the most important findings was that the two image parameters entropy and contrast of the red channel clearly indicated a systematic image change in the ischemia and reperfusion phase. As these two parameters are quite independent, this indicates that there is important information at both structure level and color level in the images that can be used by the CNN models for classification. The link between the two image parameters and the highlighted areas on the SHAP output are of interest, where we might be able to connect statistical image parameters with deep learning. For instance, including the statistical image parameters as features in a hybrid machine learning model may improve the model performance.

Both the SHAP method and the statistical image parameter analysis method provide information about the intestinal images. From Figure 7, we can see that some of the blood vessels were highlighted, which are some of the patterns that CNN recognizes naturally. The larger blood vessels near the small intestine surface contribute both to higher values of entropy and contrast. In the future, we plan to study the characteristics behind the highlighted areas on a SHAP output plot, where possibly important features and changes during ischemia-reperfusion injury on the small intestine can be revealed, which are not yet known.

There are some limitations to this study. First, the small number of pig subjects that we used, which may lead to a limited generalization of the model, where both within group variance and between group variance may not be fully covered. We observed variations both between pigs and between different locations in the same small intestine segment. Another limitation is the segmental warm full ischemia and reperfusion model that we used, which does not cover all clinical conditions. Different clinical conditions, such as partial occlusion, may lead to different physiological behaviors, causing variations in

appearance of the small intestine. With respect to sources of measurement error, due to the semi-transparent nature of the small intestine, light from surrounding light sources may have entered the site causing variations in amount of light in the images. When downsizing the images, important information might have been lost, which is a limitation that was chosen based on the available computer memory size. Moreover, images from all individual pigs and intestinal segments were mixed first, before separating to training, validation, and test datasets. Evaluation of model performance and generalizability might be weakened as images from the same intestinal segment may be included in different batches during both training and testing, which might lead to over-fitting. The results might be biased as images from the same pig can fall into both the training and the test dataset. Our method needs to be validated on a larger dataset and preferably with human intestine, to assess the realistic potential in this method.

The overall results suggest that a combination of microscopic images taken from the small intestine surface can potentially be used as an objective, fast, and accurate method to assess ischemia-reperfusion injury on the small intestine. This proposed technique does not require clinical and technical experience, and due to the non-invasive nature of the method, it can be relatively easy to attain clinical approval with respect to sterile requirements and electrical safety.

5. Conclusions

In this study, we investigated whether microscopic images taken from the surface of the small intestine in vivo in a pig model, combined with deep learning, can be used to assess ischemia-reperfusion injuries. Different deep learning models were evaluated and compared, ResNet50 outperformed the Bayesian CNN, CNN with decision-level fusion and traditional CNN. The uncertainty estimation provided by the Bayesian CNN model can be important in clinical settings. In combination with the explainable AI-SHAP method, not only can we assess the viability state of the small intestine, at the same time, we can explain what regions of the intestine the model used as a basis for decision making. A clear indication of systematic changes on the images in the ischemia and reperfusion phases was found in the entropy and contrast properties of the images. This work lays the cornerstone for a planned future study where we aim to make use of a much larger dataset with images of the intestine surface captured either manually during open surgery or from laparoscopic video taken from patients who undergo laparoscopy surgery to evaluate our method.

Author Contributions: Conceptualization, J.H. and R.S.-A.; Methodology, J.H. and R.S.-A.; Formal Analysis, J.H.; Resources, T.I.T.; Data Curation, J.H.; Writing—Original Draft Preparation, J.H.; Writing—Review and Editing, J.H., R.S.-A., C.T., J.O.H., Ø.G.M., T.I.T.; Supervision, R.S.-A., C.T., J.O.H., Ø.G.M., T.I.T.; Project Administration, T.I.T.; Funding Acquisition, T.I.T. All authors have read and agreed to the published version of the manuscript.

Institutional Review Board Statement: The study was conducted according to the guidelines of the Declaration of Helsinki and national animal welfare guidelines of Norway, and was approved by the Norwegian Food Safety Authority (NFSA) with project identification code NFSA 12695 at date 25 August 2017.

Informed Consent Statement: Not applicable.

Data Availability Statement: Data are available from the authors upon reasonable request.

Conflicts of Interest: The authors declare that they have no competing interest.

References

1. Bryski, M.G.; Frenzel Sulyok, L.G.; Kaplan, L.; Singhal, S.; Keating, J.J. Techniques for intraoperative evaluation of bowel viability in mesenteric ischemia: A review. *Am. J. Surg.* **2020**, *220*, 309–315. [CrossRef]
2. Herbert, G.S.; Steele, S.R. Acute and Chronic Mesenteric Ischemia. *Surg. Clin. N. Am.* **2007**, *87*, 1115–1134. [CrossRef]
3. Reginelli, A.; Iacobellis, F.; Berritto, D.; Gagliardi, G.; Di Grezia, G.; Rossi, M.; Fonio, P.; Grassi, R. Mesenteric ischemia: The importance of differential diagnosis for the surgeon. *BMC Surg.* **2013**, *13*, S51. [CrossRef]
4. Orland, P.J.; Cazi, G.A.; Semmlow, J.L.; Reddell, M.T.; Brolin, R.E. Determination of Small Bowel Viability Using Quantitative Myoelectric and Color Analysis. *J. Surg. Res.* **1993**, *55*, 581–587. [CrossRef]
5. Bulkley, G.B.; Zuidema, G.D.; Hamilton, S.R.; O'Mara, C.S.; Klacsmann, P.G.; Horn, S.D. Intraoperative determination of small intestinal viability following ischemic injury: A prospective, controlled trial of two adjuvant methods (Doppler and fluorescein) compared with standard clinical judgment. *Ann. Surg.* **1981**, *193*, 628–637. [CrossRef]
6. Redaelli, C.A.; Schilling, M.K.; Büchler, M.W. Intraoperative Laser Doppler Flowmetry: A Predictor of Ischemic Injury in Acute Mesenteric Infarction. *Dig. Surg.* **1998**, *15*, 55–59. [CrossRef]
7. He, K.; Zhang, X.; Ren, S.; Sun, J. Deep Residual Learning for Image Recognition. *arXiv* **2015**, arXiv: 1512.03385.
8. Gal, Y.; Ghahramani, Z. Bayesian Convolutional Neural Networks with Bernoulli Approximate Variational Inference. *arXiv* **2016**, arXiv:1506.02158.
9. Lundberg, S.; Lee, S.I. A Unified Approach to Interpreting Model Predictions. *arXiv* **2017**, arXiv:1705.07874.
10. Borgli, H.; Thambawita, V.; Smedsrud, P.H.; Hicks, S.; Jha, D.; Eskeland, S.L.; Randel, K.R.; Pogorelov, K.; Lux, M.; Nguyen, D.T.D.; et al. HyperKvasir , a comprehensive multi-class image and video dataset for gastrointestinal endoscopy. *Sci. Data* **2020**, *7*, 283. [CrossRef] [PubMed]
11. Yan, T.; Wong, P.K.; Choi, I.C.; Vong, C.M.; Yu, H.H. Intelligent diagnosis of gastric intestinal metaplasia based on convolutional neural network and limited number of endoscopic images. *Comput. Biol. Med.* **2020**, *126*, 104026. [CrossRef]
12. Strand-Amundsen, R.J.; Tronstad, C.; Kalvøy, H.; Gundersen, Y.; Krohn, C.D.; Aasen, A.O.; Holhjem, L.; Reims, H.M.; Martinsen, Ø.G.; Høgetveit, J.O.; et al. In vivocharacterization of ischemic small intestine using bioimpedance measurements. *Physiol. Meas.* **2016**, *37*, 257–275. [CrossRef] [PubMed]
13. Umesh, P. Image Processing in Python. *Csi Commun.* **2012**, *23*, 2.
14. Shannon, C.E.; Weaver, W. *The Mathematical Theory of Communication*; The Mathematical Theory of Communication, University of Illinois Press: Champaign, IL, USA, 1949; p. 117.
15. Vajapeyam, S. Understanding Shannon's Entropy metric for Information. *arXiv* **2014**, arXiv:1405.2061.
16. Hall-Beyer, M. GLCM Texture: A Tutorial v. 3.0 March 2017. Attribution Non-Commercial 4.0 International. Available online: doi:10.11575/PRISM/33280 (accessed on 28 May 2021). [CrossRef]
17. Gu, J.; Wang, Z.; Kuen, J.; Ma, L.; Shahroudy, A.; Shuai, B.; Liu, T.; Wang, X.; Wang, G.; Cai, J.; et al. Recent advances in convolutional neural networks. *Pattern Recognit.* **2018**, *77*, 354–377. [CrossRef]
18. Chollet, F. Keras. 2015. Available online: https://keras.io (accessed on 19 May 2021).
19. Wang, X.; Han, T.X.; Yan, S. An HOG-LBP human detector with partial occlusion handling. In Proceedings of the 2009 IEEE 12th International Conference on Computer Vision, Kyoto, Japan, 27 September–4 October 2009; pp. 32–39, ISSN: 2380-7504. [CrossRef]
20. Walt, S.v.d.; Schönberger, J.L.; Nunez-Iglesias, J.; Boulogne, F.; Warner, J.D.; Yager, N.; Gouillart, E.; Yu, T. scikit-image: Image processing in Python. *PeerJ* **2014**, *2*, e453. [CrossRef]
21. Ho, T.K. Random decision forests. In Proceedings of the 3rd International Conference on Document Analysis and Recognition, Montreal, QC, Canada, 14–16 August 1995; Volume 1, pp. 278–282. [CrossRef]
22. Pedregosa, F.; Varoquaux, G.; Gramfort, A.; Michel, V.; Thirion, B.; Grisel, O.; Blondel, M.; Prettenhofer, P.; Weiss, R.; Dubourg, V.; et al. Scikit-learn: Machine Learning in Python. *J. Mach. Learn. Res.* **2011**, *12*, 2825–2830.
23. Abadi, M.; Agarwal, A.; Barham, P.; Brevdo, E.; Chen, Z.; Citro, C.; Corrado, G.S.; Davis, A.; Dean, J.; Devin, M.; et al. TensorFlow: Large-Scale Machine Learning on Heterogeneous Distributed Systems. *arXiv* **2016**, arXiv:1603.04467.
24. Kingma, D.P.; Welling, M. Auto-Encoding Variational Bayes. *arXiv* **2014**, arXiv:1312.6114.
25. Strand-Amundsen, R.J.; Reims, H.M.; Reinholt, F.P.; Ruud, T.E.; Yang, R.; Høgetveit, J.O.; Tønnessen, T.I. Ischemia/reperfusion injury in porcine intestine—Viability assessment. *World J. Gastroenterol.* **2018**, *24*, 2009–2023. [CrossRef]
26. Boros, M.; Takaichi, S.; Hatanaka, K. Ischemic time-dependent microvascular changes and reperfusion injury in the rat small intestine. *J. Surg. Res.* **1995**, *59*, 311–320. [CrossRef] [PubMed]
27. Yamada, T.; Taguchi, T.; Suita, S. Energy metabolism and tissue blood flow as parameters for the assessment of graft viability in rat small bowel transplantation. *J. Pediatr. Surg.* **1996**, *31*, 1475–1481. [CrossRef]
28. Taguchi, T.; Yamada, T.; Suita, S.; Ohta, M. The significance of cytological examination on reperfusion in rat small intestinal transplantation. *Virchows Arch. Int. J. Pathol.* **1995**, *427*, 71–76. [CrossRef]
29. Bengio, Y.; Frasconi, P.; Schmidhuber, J. Gradient Flow in Recurrent Nets: the Difficulty of Learning Long-Term Dependencies. In *A Field Guide to Dynamical Recurrent Neural Networks*; IEEE Press: Manhattan, NY, USA, 2001.
30. Ghahramani, Z. Probabilistic machine learning and artificial intelligence. *Nature* **2015**, *521*, 452–459. [CrossRef]
31. Mudgal, K.S.; Das, N. The ethical adoption of artificial intelligence in radiology. *BJR Open* **2019**, *2*, 20190020. [CrossRef]

32. Holzinger, A.; Langs, G.; Denk, H.; Zatloukal, K.; Müller, H. Causability and explainability of artificial intelligence in medicine. *Wires Data Min. Knowl. Discov.* **2019**, *9*, e1312. [CrossRef] [PubMed]
33. Voosen, P. How AI Detectives Are Cracking Open the Black Box of Deep Learning. Available online: https://doi.org/10.1126/SCIENCE.AAN7059 (accessed on 14 January 2021).

Paper III

Assessing ischemic injury in human intestine ex vivo with electrical impedance spectroscopy

Jie Hou, Runar Strand-Amundsen, Stina Hødnebø, Tor Inge Tønnessen, Jan Olav Høgetveit

III

Assessing ischemic injury in human intestine ex vivo with electrical impedance spectroscopy

Jie Hou[1, 2, *], Runar Strand-Amundsen[1], Stina Hødnebø[3], Tor Inge Tønnessen[3, 4], and Jan Olav Høgetveit[1, 2]

[1]Department of Clinical and Biomedical Engineering, Oslo University Hospital, 0424 Oslo, Norway.
[2]Department of Physics, University of Oslo, 0316 Oslo, Norway.
[3]Department of Emergencies and Critical Care, Oslo University Hospital, 0424 Oslo, Norway.
[4]Institute of Clinical Medicine, University of Oslo, 0318 Oslo, Norway.
[*]E-mail any correspondence to: jieho@fys.uio.no

Abstract

Electrical impedance spectroscopy is a well-established tool for monitoring changes in the electrical properties of tissue. Most tissue and organ types have been investigated in various studies. As for the small intestine, there are several published studies conducted on pig and rat models. This study investigates the changes in passive electrical properties of the complete wall of the human intestine non-invasively during ischemia. We aim to use the passive electrical properties to assess intestinal viability. The bioimpedance measurements were performed using a two-electrode set-up with a Solartron 1260 Impedance/gain-phase analyser. The small intestinal samples were resected from patients who underwent pancreaticoduodenectomy. Impedance measurements were conducted following resection by placing the electrodes on the surface of the intestine. A voltage was applied across the intestinal sample and the measured electrical impedance was obtained in the ZPlot software. Impedance data were further fitted into a Cole model to obtain the Cole parameters. The P_y value was calculated from the extracted Cole parameters and used to assess the cell membrane integrity, thus evaluate the intestinal viability. Eight small intestinal segments from different patients were used in this study and impedance measurements were performed once an hour for a ten-hour period. One hour after resection, the impedance decreased, then increased the next two hours, before decreasing until the end of the experiment. For all the intestinal segments, the P_y values first increased and reached a plateau which lasted for 1 - 2 hours, before it decreased irreversibly. The time interval where P_y value reached the maximum is consistent with reported viable/non-viable limits from histological analysis.

Keywords: Bioimpedance; Human small intestine; Cole model; P_y value

Introduction

Assessment of intestinal viability following acute intestinal ischemia is important. There is an associated high mortality rate (30 - 93 %) partly due to the difficulty in diagnosing and treating the disease before irreversible injury occurs [1, 2, 3]. Following intestinal ischemia, estimation of ischemia time and determination of resection region(s) play a decisive role. The main challenge in detecting intestinal ischemia is the diffuse symptoms. It is often hard to determine how long the intestine has been ischemic and if it is still viable or not. Visual inspection and palpation are still the standard clinical methods for evaluation of the intestinal viability. Estimation of color change, presence of visible peristalsis and bleeding from cut edges are often used to estimate the intestine condition [4, 5, 6, 7, 8]. Those methods are non-specific and often unreliable. Viable tissue might be removed, or more critically, irreversibly damaged tissue might be left in the patient. This may lead to a second surgery and slow down the patient recovery. Moreover, histological analysis has been used to assess intestinal viability [9] and a number of studies have been published. They report that the time before irreversible injury occurs varies between species, anatomical locations and between the ischemia models used [10, 11, 12]. There is no standard classification method for the histological assessment of intestinal ischemia injury [13]. Therefore, a non-invasive, easy to employ and reliable monitoring method of ischemic tissue injury is of great interest [14].

Electrical impedance spectroscopy (EIS) has been regarded as a promising method for early diagnosis and monitoring of tissue ischemia due to its non-invasive, non-destructive and easily applicable nature [14, 15].

Over the past decades, EIS has been utilized to investigate changes in electrical parameters during ischemia in various tissues [16, 17, 18, 19, 20]. The frequency dependent EIS measures how well materials impede electric current flow, when a voltage is being applied to the material under test. Biological materials contain cells with intra- and extra-cellular fluid. At low frequencies the current flow is mainly in the extracellular fluid, while with increasing frequency, the current passes through the cell membranes, resulting in different electrical properties [21]. The impedance response of biological tissue is strongly influenced by the cell composition [22]. During ischemia, physical changes in the tissue results in altered impedance values. As ischemia prolongs, there is a shift in the ratio between extracellular and intracellular water. The amount of extracellular water decreases, when the cells swell due to osmosis as the ionic pump function declines [21, 23]. Thereafter, a decrease of impedance is observed due to increased cell membrane permeability caused by reduced functionality [24]. As ischemia time prolongs, the β-dispersion disappears over time as the cell membranes collapse [21].

In this work, we investigated how electrical parameters of the human small intestine changed during ischemia and the data were fitted to a Cole model and analyzed. Using the Cole equation, the measured impedance data can both be visualized and analysed through the Cole parameters [25]. The P_y value obtained from the Cole parameters can be used to evaluate the cell membrane integrity [26] to assess the ischemic injury of the small intestine.

Materials and methods

A total of 8 experiments were conducted on segments of resected human small intestine. The segments came from volunteer participants undergoing standard pancreaticoduodenectomy (Whipple procedure). The study involved no extra surgical procedures for the patients. The surgeon removed the head of the pancreas and a part of the small intestine. We received the intestine segments (length range 10 - 15 cm) immediately after the resection.

Experimental set-up

Impedance measurements were performed with a Solartron 1260 Impedance/gain-phase analyser (Solartron Analytical, UK) with a 1294A interface. A pair of Ag/AgCl electrocardiography disc electrodes with 9 mm in diameter (Quickels System AB, Sweden) was connected to the gain-phase analyzer. During the measurements, the data were logged by the ZPlot software (Scribner Associates, USA). The two-electrode set-up was chosen based on the previous study conducted on porcine small intestine by Strand-Amundsen et al. [27]. The reason for not choosing a tetrapolar set-up is that the set-up is more vulnerable to errors compared to bipolar set-ups [21]. Using a tetrapolar set-up on the surface of the small intestine, the current can easily shunt across the surface of the pick-up electrodes. This brings the potential of the pick-up electrodes to a level that is closer to that of the current-carrying electrodes. This leads to an overestimation of the transfer impedance and can lead to measuring a positive phase. A 50 mV signal was applied during all the measurements, while the resulting current was measured and calculated into impedance values. The frequency range used was from 100 Hz to 1 MHz, with 41 log-spaced frequency points. The resected intestinal samples were kept inside a container with a Ringer-solution with 4 % Albumin. The container was placed in a temperature controlled water bath at a constant temperature of 37 °C (normal bowel temperature) between the measurements in order to maintain a stable temperature and reduce loss of humidity.

Figure 1: Experiment set-up. Human intestine sample under measurement.

Ethical approval

The research related to human use has been complied with all relevant national regulations, institutional policies and in accordance with the tenets of the Helsinki Declaration, and has been approved by the Norwegian regional ethical committee (2018/1630).

Data analysis

Electrical impedance is the ability of a material to oppose current flow. Complex electrical impedance (Z) is expressed as follows:

$$Z = R + jX \tag{1}$$

The real part of the impedance is the in-phase resistance (R) which in tissue is mainly due to free ions, whereas the imaginary part is the capacitive reactance (X), mainly resulting from capacitive effects of the cell membranes. The impedance modulus $|Z|$ can be expressed as:

$$|Z| = \sqrt{R^2 + X^2} \tag{2}$$

98

In 1940, Cole [28] introduced a mathematical model that can be used to fit the experimentally obtained electrical impedance data (Equation (3)). The model is based on four parameters R_0, R_∞, α and τ:

$$Z(\omega) = R_\infty + \frac{R_0 - R_\infty}{1 + (j\omega\tau)^\alpha} \qquad (3)$$

The Cole equation can be separated into its real (resistance (R)) and imaginary (reactance (X)) component as a function of the angular frequency ω.

$$R(\omega) = R_\infty + \frac{(R_0 - R_\infty)(1 + (\omega\tau)^\alpha \cos(\frac{\alpha\pi}{2}))}{1 + 2(\omega\tau)^\alpha \cos(\frac{\alpha\pi}{2}) + (\omega\tau)^{2\alpha}} \qquad (4)$$

$$X(\omega) = -j\frac{(R_0 - R_\infty)(\omega\tau)^\alpha \sin(\frac{\alpha\pi}{2})}{1 + 2(\omega\tau)^\alpha \cos(\frac{\alpha\pi}{2}) + (\omega\tau)^{2\alpha}} \qquad (5)$$

where R_0 and R_∞ are resistance at very low and very high frequencies, respectively. α is a dimensionless shape parameter which takes value between 0 and 1. τ is the time constant. ω is the angular frequency ($\omega = 2\pi f$).

Often, it is not necessary to use the entire frequency spectrum as there is a strong correlation between the impedance values at adjacent frequencies [21]. Therefore, to assess the viability of the small intestine tissue, the P_y value was chosen as it is a fast and direct measure of the β-dispersion (caused by cell membrane structures). It indicates the cell volume fraction in tissue and represents the cell membrane behavior [29]. As the cell membrane loses its integrity, the β-dispersion will gradually disappear resulting in a decreased P_y value [29]. According to Pliquett et al. [29], the P_y value can be calculated as the following:

$$P_y = \frac{R_0 - R_\infty}{R_0} \times 100 \qquad (6)$$

R_0 and R_∞ can be estimated by fitting the measured data to the Cole equation (3). The R_0 is related to the extracellular water since low frequency current is not able to pass through the cell membrane, whereas the R_∞ can be used to estimate the intracellular water as high frequency current passes through the cell membranes [30]. Physically, the P_y monotonically increase with the cell volume fraction surrounded by intact cell membranes [29]. When cells swell, the P_y will typically increase as the cell volume fraction increases, whereas when cell membrane disintegrate, due to for instance cell death, the P_y value will decrease as the volume fraction surrounded by insulating cell membranes decreases. The P_y value is zero when no cells are present, and approaches one (100 %) when cells are intensely packed with no extracellular space [29].

Results
Impedance data analysis
The impedance of the small intestine was measured once an hour for a ten-hour period. The frequency dependent

impedance showed different behavior for different degrees of ischemic injury. Figure 2 shows the mean measured
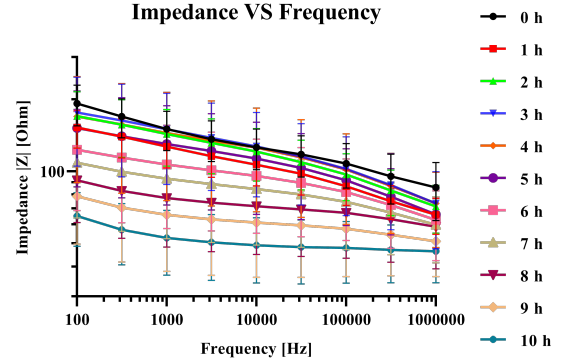

Figure 2: Plot of mean impedance values with 95 % confidence interval against frequency for 0 to 10 hours duration.

impedance with 95 % confidence interval of eight samples (length range 10 - 15 cm) from eight different patients. The impedance values over the whole frequency range first decreased after one hour following resection, then increased for the two following hours, before decreasing again for the rest of the experiment. Comparing the mean impedance value from freshly resected samples with the mean impedance value after ten hours of ischemia, the decrease in impedance are 66.15 % (at the highest frequency) and 44.84 % (at the lowest frequency). Figure
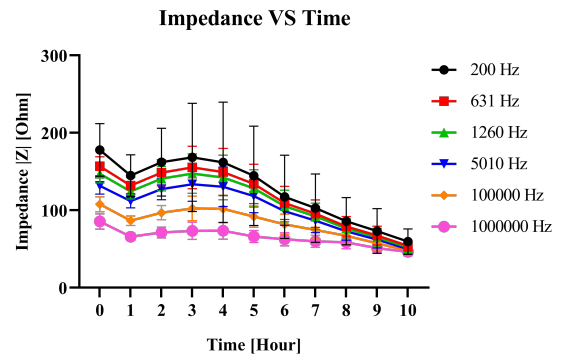

Figure 3: Plot of mean impedance values with 95 % confidence interval against time (0 to 10 hours) for selected frequencies.

3 shows the mean impedance values with 95 % confidence interval at selected frequencies. At all frequencies, the impedance value decreased after one hour. Then a plateau was observed at 3 hours before a continuous

decrease until the end of the experiment. After 10 hours of ischemia, the impedance value all decreased towards 55 Ω for all selected frequencies.

P_y value

The P_y values were calculated from the Cole fitting parameters. Each impedance measurement was fitted separately, and we obtained one P_y value for each sample and each time interval. Figure 4 shows the calculated
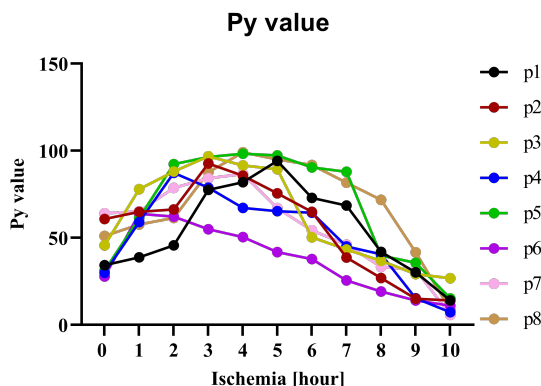
Py value

Figure 4: Plot of calculated P_y value for eight small intestine samples from different patients.

P_y values from the fitting procedure for eight intestine samples. The P_y value first increased then decreased with time. For almost all samples, the P_y value reached its maximum value between 2 - 4 hours.

Discussion

The determination of the viability of ischemic intestine is still performed by manual observation of non-specific parameters like color, peristalsis and bleeding. We investigated how the P_y value obtained from electrical impedance measurements associate with tissue vitality based on histological evaluation in a prior study [31]. As the P_y value is a direct measure of the contributions of the cell membranes, it can be used to directly assess the ischemic injury levels in tissue. Ischemic injury is well known to directly affect cell membranes through several mechanisms, influencing the passive electrical properties of the cells. Therefore, ischemic injury can be sensitively detected by passive electrical properties [26].

As figure 4 shows, the P_y value first increased. This associates with the cell swelling due to reduced function in the ionic pumps during the early phase of ischemia. During ischemia there is also an accumulation of metabolites, which also influence cell swelling. The cell swelling leads to a ratio change between intracelluar and extracelluar liquids [21, 32]. Thereafter, the P_y value decreased with time as cell membrane loses its integrity. The time maximum P_y value occurs corresponds

to the reported viable and non-viable state transition of the tissue. Pliquett et al. [26] proposed that P_y value increases by ischemic stress and plateaus for a period of time. Thereafter, it decreases continuously due to dissociation of the cell membranes and destruction of tissue. Strand-Amundsen et al. [31] reported, based on histological analysis, that irreversible injury on pig jejunum occurs around 3 - 4 hours of ischemia following reperfusion. However, histological assessment is difficult, due to the heterogeneous nature of the intestine sample [33, 34].

Interestingly, for almost all samples, the P_y value reached the maximum value between 2 - 4 hours, which is consistent with the reported histological analysis results. Pliquett et al. [26] suggested that the P_y value is good for assessment of tissue vitality, where the tissue is vital until the maximum is reached, followed by an irreversible decrease.

Another study published by Chen et al. [35] concluded that ileum segments can tolerate ischemia for less than 2 hours. Beltran et al. [36] reported that intestinal segments subjected to reperfusion after 2 hours of ischemia, did not fully recover after superior mesenteric artery occlusion in pig models. Regarding the ischemia tolerance time, based on the limited references, it appears that our P_y value corresponds well with the estimated small-intestinal viability limits reported in the above mentioned studies.

Our results show that the P_y value varies between individuals. This can be due to several factors including age, weight, body mass index (BMI) and medical history. Especially, a high BMI value may affect the impedance measurements as fat tissue has different electrical properties. In addition, some of the intestinal samples were from patients that previously had received chemotherapy. Chemotherapy can influence the measured impedance, for instance, due to fibrosis in parts of the tissue. As intestinal injury caused by ischemia appears to be heterogeneous [27], the measurement site where the electrodes are placed on the tissue may not represent the ischemic injury in the whole intestinal sample. Further on, there might be influences from the variation of mechanical pressure between the two electrodes during the measurements. When exposed to ischemia for more than approximately 3 hours, the intestinal wall gradually appears thinner, as the muscle cells are unable to function. Thus, the intestinal segment becomes softer, resulting in the surface of the intestine being more flexible to the mechanical pressure from the electrodes. This leads to a narrower distance between the electrodes, possibly changing the current path through the intestinal tissue. Another factor that can cause difference between the measurements is temperature variation. To prevent temperature to influence the measurements, the intestinal segment was kept in a container with constant temperature between

100

the measurements. The temperature changes from exposing the intestinal segment to the environment for one or two minutes during measurements can be considered negligible.

To the best of our knowledge, this is the first study to investigate ischemic injury in human small intestine non-invasively using EIS and P_y value. Strand-Amundsen et al. [37] performed bioimpedance measurements on pig small intestine ex vivo, where they found that there was an initial increase in impedance during the first hour, followed by a stable period of two hours, before the impedance started to decrease. The electrical behavior observed by [37] was different for the first two hours compared with our observations. We found that the impedance first decreased after one hour of ischemia, then increased for the following two hours. The reason behind these differences could be related to the temperature difference between the first and second measurements that we performed, where the temperature was lower during the first measurement. The intestinal sample was exposed to air for several minutes after the resection before we performed our first measurement. For the following measurements the temperature was kept constant in a water bath. Another possible cause of the observations could be due to potential variation in the development in passive electrical properties during ischemia between pig and human.

Evaluation of changes in the passive electrical properties of human intestine during ischemia in eight intestinal segment is a limitation. A small dataset may not reveal the true variation in the group. We plan to increase the number of intestine samples in the future. As for the measurement techniques, placing the electrodes against the intestine wall results in variations of pressure which can potentially affect the measured impedance. Efforts were made to control this variation, but it still cannot be completely excluded. There are also some uncertainties regarding the reproducibility of the impedance data. The reported reproducibility of passive electrical behavior within the same tissue in the same animal model is not better than 90–95 % [29].

Conclusion

From our limited dataset, it is apparent that electrical properties can be used to assess the degree of ischemic injury on the human intestine. Our results suggest that there is a difference in the early changes during ischemia in measured impedance between pig intestine and human intestine. The time development of the P_y parameter, which assesses the integrity of cell membranes, associated with the time development of ischemic injury reported in other studies. An increasing P_y value associated with reported cell swelling, while a decreasing P_y value associated with reported increase in leakage from- and dissociation of- the cell membranes in the later ischemia process. Conclusively, the P_y value can, comparably to histological analysis, be used to evaluate the viability of the intestine, where the tissue is vital until the maximum P_y value is reached.

Conflict of interest
Authors state no conflict of interest.

References
1. Bala M, Kashuk J, Moore EE, Kluger Y, Biffl W, Gomes CA, Ben-Ishay O, Rubinstein C, Balogh ZJ, Civil I, Coccolini F, Leppaniemi A, Peitzman A, Ansaloni L, Sugrue M, Sartelli M, Di Saverio S, Fraga GP, and Catena F. Acute mesenteric ischemia: guidelines of the World Society of Emergency Surgery. World Journal of Emergency Surgery 2017 Aug; 12:38. DOI: 10.1186/s13017-017-0150-5

2. Brandt LJ and Boley SJ. AGA technical review on intestinal ischemia. en. Gastroenterology 2000 May; 118:954–68. DOI: 10.1016/S0016-5085(00)70183-1

3. Tilsed JVT, Casamassima A, Kurihara H, Mariani D, Martinez I, Pereira J, Ponchietti L, Shamiyeh A, al-Ayoubi F, Barco LAB, Ceolin M, D'Almeida AJG, Hilario S, Olavarria AL, Ozmen MM, Pinheiro LF, Poeze M, Triantos G, Fuentes FT, Sierra SU, Soreide K, and Yanar H. ESTES guidelines: acute mesenteric ischaemia. en. European Journal of Trauma and Emergency Surgery 2016 Apr; 42:253–70. DOI: 10.1007/s00068-016-0634-0

4. Bryski MG, Frenzel Sulyok LG, Kaplan L, Singhal S, and Keating JJ. Techniques for intraoperative evaluation of bowel viability in mesenteric ischemia: A review. en. The American Journal of Surgery 2020 Aug; 220:309–15. DOI: 10.1016/j.amjsurg.2020.01.042

5. Reginelli A, Iacobellis F, Berritto D, Gagliardi G, Di Grezia G, Rossi M, Fonio P, and Grassi R. Mesenteric ischemia: the importance of differential diagnosis for the surgeon. BMC Surgery 2013 Oct; 13:S51. DOI: 10.1186/1471-2482-13-S2-S51

6. Herbert GS and Steele SR. Acute and Chronic Mesenteric Ischemia. en. Surgical Clinics of North America. Vascular Surgery: 2007 Oct; 87:1115–34. DOI: 10.1016/j.suc.2007.07.016

7. Orland PJ, Cazi GA, Semmlow JL, Reddell MT, and Brolin RE. Determination of Small Bowel Viability Using Quantitative Myoelectric and Color Analysis. en. Journal of Surgical Research 1993 Dec; 55:581–7. DOI: 10.1006/jsre.1993.1188

8. Bulkley GB, Zuidema GD, Hamilton SR, O'mara CS, Klacsmann PG, and Horn SD. Intraoperative Determination of Small Intestinal Viability following Ischemic Injury: A Prospective, Controlled Trial of Two Adjuvant Methods (Doppler and Fluorescein) Compared with Standard Clinical Judgment. en-US. Annals of Surgery 1981 May; 193:628–37. DOI: 10.1097/00000658-198105000-00014

9. Urbanavičius L, Pattyn P, Van de Putte D, and Venskutonis D. How to assess intestinal viability during surgery: A review of techniques. World Journal of Gastrointestinal Surgery 2011 May; 3:59–69. DOI: 10.4240/wjgs.v3.i5.59

10. Brolin RE, Bibbo C, Petschenik A, Reddell MT, and Semmlow JL. Comparison of ischemic and reperfusion injury in canine bowel viability assessment. en. Journal of Gastrointestinal Surgery 1997 Nov; 1:511–6. DOI: 10.1016/S1091-255X(97)80066-2

11. Haglund U, Bulkley GB, and Granger DN. On the pathophysiology of intestinal ischemic injury. Clinical review. eng. Acta Chirurgica Scandinavica 1987; 153:321–4

12. Gonzalez LM, Moeser AJ, and Blikslager AT. Animal models of ischemia-reperfusion-induced intestinal injury: progress and promise for translational research. American Journal of Physiology-Gastrointestinal and Liver Physiology 2015 Jan; 308. Publisher: American Physiological Society:G63–G75. DOI: 10.1152/ajpgi.00112.2013

13. Quaedackers JS, Beuk RJ, Bennet L, Charlton A, Egbrink MG oude, Gunn AJ, and Heineman E. An evaluation of methods for grading histologic injury following ischemia/reperfusion of the small bowel. eng. Transplantation Proceedings 2000 Sep; 32:1307–10. DOI: 10.1016/s0041-1345(00)01238-0

14. Mellert F, Winkler K, Schneider C, Dudykevych T, Welz A, Osypka M, Gersing E, and Preusse CJ. Detection of (Reversible) Myocardial Ischemic Injury by Means of Electrical Bioimpedance. IEEE Transactions on Biomedical Engineering 2011 Jun; 58. Conference Name: IEEE Transactions on Biomedical Engineering:1511–8. DOI: 10.1109/TBME.2010.2054090

15. Yang Y, Ni W, Sun Q, Wen H, and Teng Z. Improved Cole parameter extraction based on the least absolute deviation method. eng. Physiological Measurement 2013 Oct; 34:1239–52. DOI: 10.1088/0967-3334/34/10/1239

16. Martinsen Ø, Grimnes S, and Mirtaheri P. Non-invasive measurements of post-mortem changes in dielectric properties of haddock muscle – a pilot study. Journal of Food Engineering 2000 Feb; 43:189–92. DOI: 10.1016/S0260-8774(99)00151-X

17. Gheorghiu M and Eberhard G. Revealing alteration of membrane structures during ischema using impedance spectroscopy. Songklanakarin Journal of Science and Technology 2002 Nov; 24:777-84

18. Salazar Y, Cinca J, and Rosell-Ferrer J. Effect of electrode locations and respiration in the characterization of myocardial tissue using a transcatheter impedance method. eng. Physiological Measurement 2004 Oct; 25:1095–103. DOI: 10.1088/0967-3334/25/5/001

19. Ivorra Cano A. Contributions to the measurement of electrical impedance for living tissue ischemia injury monitoring. eng. Accepted: 2011-04-12T15:12:40Z ISBN: 9788468913544 Publication Title: TDX (Tesis Doctorals en Xarxa). Ph.D. Thesis. Universitat Politècnica de Catalunya, 2005 Feb

20. Asami K. Dielectric properties of biological tissues in which cells are connected by communicating junctions. English. Journal of Physics. D, Applied Physics 2007; 40:3718–27. DOI: 10.1088/0022-3727/40/12/027

21. Grimnes S and Martinsen ØG. Bioimpedance and Bioelectricity Basics. Academic Press 3rd Edition. ISBN 978-0-12-411533-0. en

22. Mouritsen OG and Bloom M. Models of lipid-protein interactions in membranes. eng. Annual Review of Biophysics and Biomolecular Structure 1993; 22:145–71. DOI: 10.1146/annurev.bb.22.060193.001045

23. Strand-Amundsen RJ, Tronstad C, Kalvøy H, Gundersen Y, Krohn CD, Aasen AO, Holhjem L, Reims HM, Martinsen ØG, Høgetveit JO, Ruud TE, and Tønnessen TI. In vivo characterization of ischemic small intestine using bioimpedance measurements. eng. Physiological Measurement 2016 Feb; 37:257–75. DOI: 10.1088/0967-3334/37/2/257

24. Schäfer M, Schlegel C, Kirlum HJ, Gersing E, and Gebhard MM. Monitoring of damage to skeletal muscle tissues caused by ischemia. en. Bioelectrochemistry and Bioenergetics 1998 May; 45:151–5. DOI: 10.1016/S0302-4598(98)00083-X

25. Ayllon D, Seoane F, and Gil-Pita R. Cole equation and parameter estimation from electrical bioimpedance spectroscopy measurements - A comparative study. eng. Conference proceedings: ... Annual International Conference of the IEEE Engineering in Medicine and Biology Society. IEEE Engineering in Medicine and Biology Society. Annual Conference 2009; 2009:3779–82. DOI: 10.1109/IEMBS.2009.5334494

26. Pliquett F and Pliquett U. Stress Action on Biological Tissue and Tissue Models Detected by the Py Value. en. Annals of the New York Academy of Sciences 1999; 873:227–38. DOI: 10.1111/j.1749-6632.1999.tb09471.x

27. Strand-Amundsen RJ, Tronstad C, Kalvøy H, Gundersen Y, Krohn CD, Aasen AO, Holhjem L, Reims HM, Martinsen ØG, Høgetveit JO, Ruud TE, and Tønnessen TI. In vivocharacterization of ischemic small intestine using bioimpedance measurements. en. Physiological Measurement 2016 Jan; 37:257–75. DOI: 10.1088/0967-3334/37/2/257

28. Cole KS and Cole RH. Dispersion and Absorption in Dielectrics I. Alternating Current Characteristics. The Journal of Chemical Physics 1941 Apr; 9. Publisher: American Institute of Physics:341–51. DOI: 10.1063/1.1750906

102

29. Pliquett U, Altmann M, Pliquett F, and Schöberlein L. Py—a parameter for meat quality. en. Meat Science 2003 Dec; 65:1429–37. DOI: 10.1016/S0309-1740 (03)00066-4

30. Alves J, Sousa F, and Correia MV. Calibration and Electrical Validation of a BIS Portable System. eng. Studies in Health Technology and Informatics 2018; 249:122-129

31. Strand-Amundsen RJ, Reims HM, Reinholt FP, Ruud TE, Yang R, Høgetveit JO, and Tønnessen TI. Ischemia/reperfusion injury in porcine intestine - Viability assessment. World Journal of Gastroenterology 2018 May; 24:2009–23. DOI: 10.3748/wjg.v24.i18.2009

32. Sun J, Zhang R, Zhang Y, Liang Q, Zhang F, Xu P, and Li G. Evaluation of fish freshness using impedance spectroscopy based on the characteristic parameter of orthogonal direction difference. en. Journal of the Science of Food and Agriculture 2020; 100:4124–31. DOI: 10.1002/jsfa.10435

33. Hillman H. Limitations of clinical and biological histology. en. Medical Hypotheses 2000 Apr; 54:553–64. DOI: 10.1054/mehy.1999.0894

34. Dabareiner RM, Sullins KE, White NA, and Snyder JR. Serosal Injury in the Equine Jejunum and Ascending Colon After Ischemia-Reperfusion or Intraluminal Distention and Decompression. en. Veterinary Surgery 2001; 30:114–25. DOI: 10.1053/jvet.2001.21393

35. Chen SH, Tang YB, and Chen HC. Survival of Transferred Ileum after Ischemia Time Longer than 1 Hour: A Clinical Result Different from Animal Studies. en. Journal of the American College of Surgeons 2013 Aug; 217:300–5. DOI: 10.1016/j.jamcollsurg.2013.03.018

36. Beltran NE and Sacristan E. Gastrointestinal ischemia monitoring through impedance spectroscopy as a tool for the management of the critically ill. en. Experimental Biology and Medicine 2015 Jul; 240. Publisher: SAGE Publications:835–45. DOI: 10.1177/1535370215571876

37. Strand-Amundsen RJ, Reims HM, Tronstad C, Kalvøy H, Martinsen ØG, Høgetveit JO, Ruud TE, and Tønnessen TI. Ischemic small intestine—in vivoversusex vivobioimpedance measurements. en. Physiological Measurement 2017 Apr; 38:715–28. DOI: 10.1088/1361-6579/aa67b7

Utilization of dielectric properties for assessment of liver ischemia-reperfusion injury in vivo and during machine perfusion

Jie Hou, Olav Magnus Ivar Liavåg, Ida Høy Færden, Ørjan Grøttem Martinsen, Tor Inge Tønnessen, Pål-Dag Line, Morten Hagness, Jan Olav Høgetveit, Søren Erik Pischke, Runar Strand-Amundsen

scientific reports

OPEN

Utilization of dielectric properties for assessment of liver ischemia-reperfusion injury in vivo and during machine perfusion

Jie Hou[1,2✉], Olav Magnus Ivar Liavåg[3,5], Ida Høy Færden[5,6], Ørjan Grøttem Martinsen[1,2], Tor Inge Tønnessen[4,5], Pål-Dag Line[3,5], Morten Hagness[3], Jan Olav Høgetveit[1,7], Søren Erik Pischke[4,5,6] & Runar Strand-Amundsen[2]

There is a shortage of donor livers and patients consequently die on waiting lists worldwide. Livers are discarded if they are clinically judged to have a high risk of non-function following transplantation. With the aim of extending the pool of available donor livers, we assessed the condition of porcine livers by monitoring the microwave dielectric properties. A total of 21 livers were divided into three groups: control with no injury (CON), biliary injury by hepatic artery occlusion (AHEP), and overall hepatic injury by static cold storage (SCS). All were monitored for four hours in vivo, followed by ex vivo plurithermic machine perfusion (PMP). Permittivity data was modeled with a two-pole Cole–Cole equation, and dielectric properties from one-hour intervals were analyzed during in vivo and normothermic machine perfusion (NMP). A clear increasing trend in the conductivity was observed in vivo in the AHEP livers compared to the control livers. After four hours of NMP, separations in the conductivity were observed between the three groups. Our results indicate that dielectric relaxation spectroscopy (DRS) can be used to detect and differentiate liver injuries, opening for a standardized and reliable point of evaluation for livers prior to transplantation.

The waiting lists for liver transplantation are increasing worldwide, accompanied by climbing waiting list mortality[1,2]. To change this negative trend and to expand the number of transplantable livers, the utilization of marginal donors with potentially inferior liver quality has increased[3,4]. The margins for what constitutes a "transplantable liver" are presently subject to research, where conditioning and evaluation of liver parameters are important inputs for decision-making. Human donor livers, especially those procured from marginal donors, can have various degrees of injuries that may either come from before the procurement (e.g fatty liver, cirrhosis) or during the procurement (warm ischemia injury). Moreover, donor livers will also experience a certain degree of injury after the procurement during the time of organ preservation outside the body[5]. This may lead to profound ischemia-reperfusion injury at the time of transplantation and consecutively to undesired outcomes like ischemic cholangiopathy, primary nonfunction (PNF) and death of the recipient[1,6]. Transplanting organs under these high-risk circumstances require development of new and more precise tools to assess the transplantability of donated organs, and to potentially mitigate the negative effects of the procurement process and of the organ preservation outside the body[7–10].

Currently, the common method of evaluation of a liver graft for transplantation, is based on visual inspection of the donor organ by the transplant surgeon, combined with knowledge about the donor history and serology taken before procurement. When in doubt a histological evaluation is carried out, but this technique is time consuming and outcome uncertain. When the surgeon is in a quandary about the condition of the organ, which is a recurrent challenge when assessing marginal liver grafts, these organs will typically be discarded[6]. Approaches using scores (VITTAL and Groningen) with lactate clearance, bile production and perfusate pH stabilization is

[1]Department of Physics, University of Oslo, Sem Sælands vei 24, 0316 Oslo, Norway. [2]Department of Clinical and Biomedical Engineering, Oslo University Hospital, 0424 Oslo, Norway. [3]Section for Transplantation Surgery, Department of Transplantation Medicine, Oslo University Hospital, 0424 Oslo, Norway. [4]Department of Emergencies and Critical Care, Oslo University Hospital, 0424 Oslo, Norway. [5]Institute of Clinical Medicine, University of Oslo, 0318 Oslo, Norway. [6]Department of Immunology, University of Oslo, 0372 Oslo, Norway. [7]Division of Technology and Innovation, Oslo University Hospital, 0424 Oslo, Norway. ✉email: jieho@fys.uio.no

a matter of ongoing research[11]. The precision of these scores in assessing liver viability and quality is yet to be established[11] due to the multi-factorial considerations for liver transplantability[6].

Over the past 20 years, ex vivo machine perfusion of liver grafts has emerged as a platform for organ preservation that hopefully will alleviate all the above-mentioned obstacles in liver transplantation. Contemporary machine perfusion practice in the clinical setting of organ transplantation often comprises a sequential perfusion of the liver graft with cold fluid at temperatures between 4–12 °C and oxygen (hypothermic machine perfusion (HMP)) for reconditioning of the liver tissue. Thereafter, followed by warm perfusion at 37 °C (normothermic machine perfusion (NMP)) with blood or blood-like perfusate to reactivate the organ metabolically. The liver is then evaluated to assess the level of graft function and quality[10,11]. This technique has demonstrated superior outcome compared to the gold standard of ex vivo organ preservation called static cold storage (SCS) where the organs are preserved ex vivo submerged in static and cooled (4 °C) fluid. However, validated guidelines for liver graft function and viability assessment during ex vivo machine perfusion are scarce[6,11,12]. Presently there is ongoing research to investigate if machine perfusion can be used to improve the state of marginal livers and provide accurate information about the condition of the organs[13,14].

Numerous studies investigating the electrical properties of organs and tissues have been conducted to assess organ condition and to differentiate normal from pathological tissue[15–18]. However, none of those have investigated different liver conditions both in vivo and on machine perfusion using dielectric properties in the GHz frequency range. While low frequency measurements (0.1 Hz–10 MHz) can be sensitive to structural changes in the tissue, high frequency measurements in the GHz region are sensitive to concentrations and distributions of polar molecules. Most of the studies of liver tissue have used instruments in the lower frequency ranges, while only a handful of the studies have used dielectric relaxation spectroscopy (DRS) in the higher frequency ranges[19]. In 2007, O'Rourke et al.[20] investigated the dielectric properties of human liver, comparing normal tissue, malignant cancer tissue and cirrhotic tissue. Measurements were performed both in vivo and ex vivo from 500 MHz to 20 GHz. They reported that there are no statistically significant differences between the dielectric properties of malignant liver cancer tissue and normal liver tissue in vivo. Furthermore, they stated that in vivo data cannot be represented in terms of a one-pole Cole–Cole model and that further work was needed to uncover the underlying mechanisms in the in vivo liver permittivity data. Farrugia et al.[21] reported characteristics of the dielectric properties of rat liver from 500 MHz to 40 GHz in vivo and used one Cole–Cole equation to model the measurement data. They suggested that the difference between in vivo and ex vivo (few minutes after excision) dielectric properties can be attributed to tissue hydration. Moreover, Peyman et al.[22] investigated variations in dielectric properties from 100 MHz to 5 GHz due to pathological changes in the human liver at 25 °C ex vivo, and they found that cirrhotic livers and liver tumors have higher permittivity and conductivity values compared to normal liver, whereas steatosis resulted in lower permittivity and conductivity. Most recently, Hou et al.[23] investigated the dielectric properties of pig small intestinal segments with different degrees of ischemia-reperfusion injuries. They reported that the DRS technique appears to be a promising method for assessing the perfusion/reperfusion state of the small intestine, and that machine learning methods can be used to more accurately differentiate viable and non-viable intestinal segments. Currently, there is still a lack of dielectric data at high frequencies from biological tissues, especially on organs undergoing ischemia-reperfusion injuries[19,24]. The present work is an exploratory study, aimed to demonstrate a proof of concept that the DRS technique has the potential to be used in the assessment of liver conditions, both in vivo and during machine perfusion.
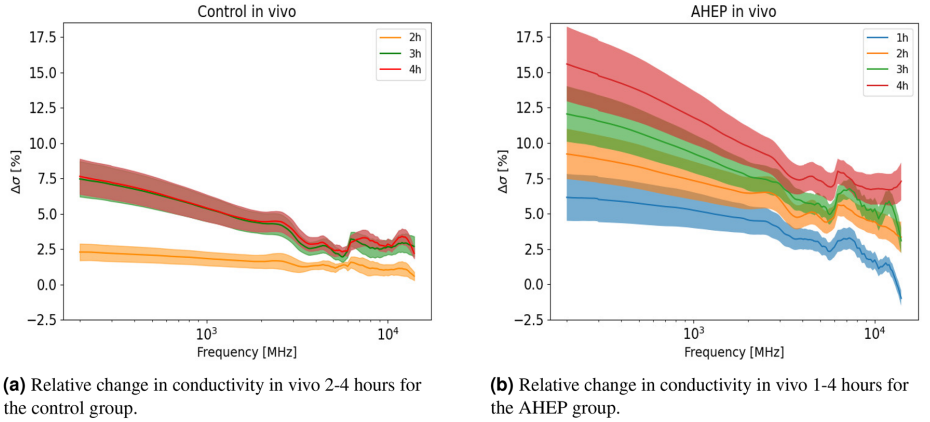
Porcine livers were used in this study, as they are close to the human liver with respect to functionality and anatomy[25]. We developed and characterized a dielectric profile over the frequency range 200 MHz–14 GHz over a four-hour duration, for both healthy liver and biliary injured livers in vivo. In addition, we characterized the dielectric properties during four hours of NMP on control (CON)-, biliary injured (AHEP)-, and overall hepatic injured (SCS) livers. In this study, our aim is to investigate the feasibility of measuring DRS on livers both in vivo and during machine perfusion, to study the association between dielectric properties on livers with different levels of injury.

Results

During the in vivo measurements, although not being a predefined end-point or subjected to systemically evaluation in this study, we did not observe any visual changes of the liver surface between the control and AHEP groups. To increase readability, Figs. 1 and 2 show the relative change in conductivity (related to dielectric loss). Plots of raw conductivity data can be found in the supplementary material. During the in vivo phase, we observed that there was an initial increase in the relative conductivity of 2.5% after two hours and a further increase of 7.5% after three and four hours for the livers in the control group (Fig. 1a) in the lower frequency region. The AHEP group showed a significant larger increase in the conductivity in vivo compared to the control livers where no intervention was performed. The conductivity increased in the AHEP group from around 5% to almost 17% in the lower frequency region. In the higher frequency region, the conductivity increased approximately 8% from the starting level during the four-hour in vivo phase (Fig. 1b).

For the in vivo data, we performed hourly comparisons (four hours) within each of the groups (control and AHEP). Significant differences were found ($p < 0.05$) in all paired comparisons for one to four hours of the in vivo phase for the control group, except for data from one hour compared to data from two hours (Table 1). For the AHEP group, statistical significant differences were found in all hourly paired comparisons, except for two hours compared to three hours (Table 1). The control group was significantly different compared to the AHEP group at all time points, except at the one hour time-point (Table 2).

After organ procurement, cold dual hypothermic oxygenated perfusion (DHOPE) and controlled oxygenated rewarming (COR) were performed, followed by the NMP procedures. Dielectric conductivity was measured for the three groups after one, two, three and four hours of NMP and compared to the in vivo control group (Fig. 2).

(a) Relative change in conductivity in vivo 2-4 hours for the control group.

(b) Relative change in conductivity in vivo 1-4 hours for the AHEP group.

Figure 1. Figure shows the relative change (mean and standard error) in conductivity monitored in vivo for both control and AHEP livers calculated with Eq. (2). One hour data is not shown in (**a**) as it is used as reference data (baseline at value zero on the y-axis). Frequency range used was 200 MHz–14 GHz (plotted in a logarithmic scale on the x-axis). N = 7 for each of the groups.

(a) After one hour of NMP.

(b) After two hours of NMP.

(c) After three hours of NMP.

(d) After four hours of NMP.
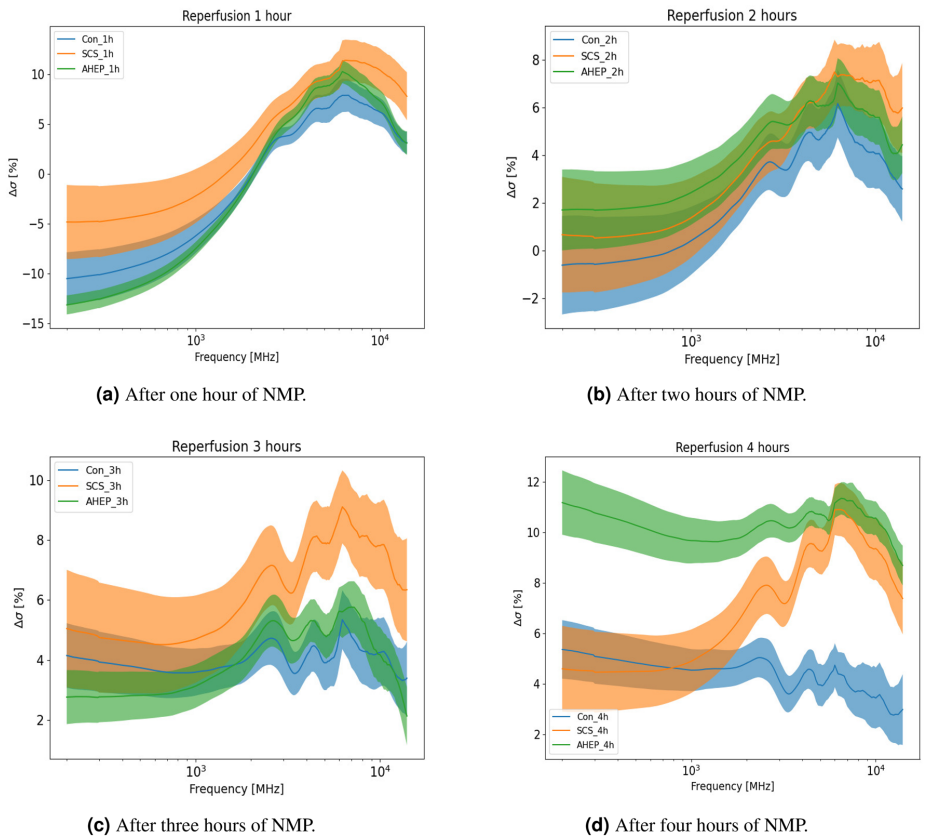
Figure 2. Relative change in the conductivity for three groups as function of frequency displayed with mean and standard error calculated with equation (2). Frequency range used was 200 MHz–14 GHz (plotted in a logarithmic scale on the x-axis). N = 7 for each of the groups.

109

Control	1 hour	2 hours	3 hours
2 hours	NS	N/A	10.75–14 GHz
3 hours	9.50–14 GHz	10.75–14 GHz	N/A
4 hours	8.25–14 GHz	10.0–14 GHz	NS
AHEP	1 hour	2 hours	3 hours
2 hours	12.25–14 GHz	N/A	NS
3 hours	10.0–14 GHz	NS	N/A
4 hours	8.50–14 GHz	12.0–14 GHz	13.25–14 GHz

Table 1. Hourly based pairwise comparison for livers in the control and the AHEP group in vivo. The table shows the frequency ranges where statistical significance were found in each hourly pairwise comparison, for livers in the control group and AHEP group (comparison within the same group). "*NS*" = "Not Significant", "*N/A*" = "Not Applicable".

AHEP / Control	1 hour	2 hours	3 hours	4 hours
1 hour	NS	7.50 - 14 GHz	6.50 - 14 GHz	6.0 - 14 GHz
2 hours	7.50 - 14 GHz	11.0 - 14 GHz	7.25 - 14 GHz	6.50 - 14 GHz
3 hours	6.50 - 14 GHz	7.25 - 14 GHz	11.50 - 14 GHz	8.50 - 14 GHz
4 hours	6.0 - 14 GHz	6.50 - 14 GHz	8.50 - 14 GHz	9.25 - 14 GHz

Table 2. Pairwise comparison for in vivo data at one-hour time interval. Table show the frequency ranges where statistical significance were found in each hourly pairwise comparison, between livers in the control group and the AHEP group (Comparison between two different groups). "*NS*" = "Not Significant", "*N/A*" = "Not Applicable".

Following one hour of NMP, the changes in conductivity appear similar in frequency dependence for the three groups, with some variations in amplitude. Compared to the in vivo control reference, the conductivity decreased around 5–14% in the low frequency region, while increasing about 5–13% in the high frequency region (Fig. 2a). Following two hours of NMP, the overlap between the three groups increased in the conductivity spectrum over the whole frequency range, while the curve shapes remained similar to the results after one hour (Fig. 2b). Following three hours of NMP, the SCS group differed from the other two groups, with higher conductivity in the high frequency region (1–14 GHz) (Fig. 2c). There was no statistical significant difference between the three groups following one, two and three hours of NMP. After four hours, there was a clear separation in the conductivity spectra between the three groups.

The differences between the NMP control group and the in vivo control reference appeared to be decreasing after four hours of NMP. The conductivity of the AHEP livers was significantly higher than the control livers following four hours of NMP (Fig. 2d). The SCS livers were similar to the control livers at low frequencies, and similar to the AHEP livers at the highest frequencies (7–14 GHz) (Fig. 2d). There were statistically significant differences between the control group and the AHEP group in the frequency ranges 4.75–5.3 GHz and 6.25–12.5 GHz, and between the control group and the SCS group in the frequency range 6.25–8.25 GHz after four hours of NMP (Fig. 2d).

An example of fitting the control liver in vivo data to a two-pole Cole–Cole equation (Eq. (3)) is shown in Fig. 3. The orange curve is the contribution from the larger molecules (compared to water molecules) and the green curve is the contribution from the water molecules, whereas the red curve indicates the dielectric loss for pure deionized water measured at 37.5 °C. The fitting results are similar for the other groups and are not shown.

The calculated water content was compared between the three groups with NMP and in vivo measurements from the control and the AHEP groups (Fig. 4). The water content was calculated based on the Cole–Cole parameters (A complete table of extracted Cole–Cole parameter values with 95% confidence interval (CI) is provided in the supplementary material). All α values obtained were lower than 0.2, all α_1 values were around 0.06 and most of the α_2 values were around 0.16. The coefficient of determination R^2 for the Cole–Cole parameters were all above 0.9998.

During the in vivo phase, the water content remained nearly constant for livers in the control group while an increasing trend was observed for livers in the AHEP group. During NMP, the water content was highest after the first hour. Following two hours of NMP, all three groups displayed a decreasing trend. After three and four hours of NMP, the water content in the control group continued to decrease, while the water content in the SCS group remained high. The water content in the AHEP livers decreased during the first hours of NMP, similar to the control group, but then started to increased towards the end of the NMP (Fig. 4).

We measured the weight of the livers two times during the experiment, once immediately after explantation and once after machine perfusion. For livers in the control group, the average weight was 1666.9 g before machine perfusion and 1755.3 g after machine perfusion, with an average increase of weight 88.4 g. For livers in the AHEP group, the average weight was 1648.9 g before machine perfusion and 1774.3 g after machine perfusion, with an average increase of weight 125.4 g. For livers in the SCS group, the average weight was 1625.7 g before machine perfusion and 1790.0 g after machine perfusion, with an average increase of weight 164.3 g. The weight increase after machine perfusion was highest for livers in the SCS group, followed by the AHEP group and the lowest
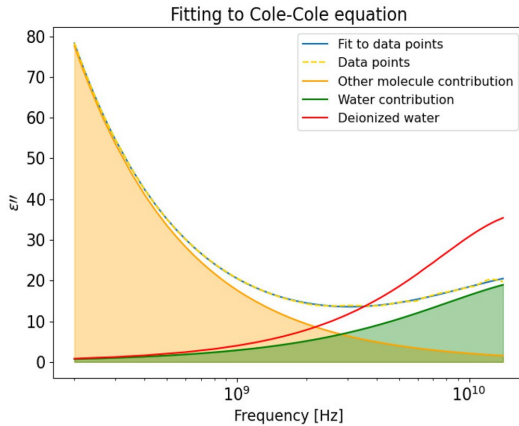
Figure 3. Cole–Cole model fit to data from 200 MHz to 14 GHz including 167 data points and separation of the two processes together with dielectric loss of deionized water.
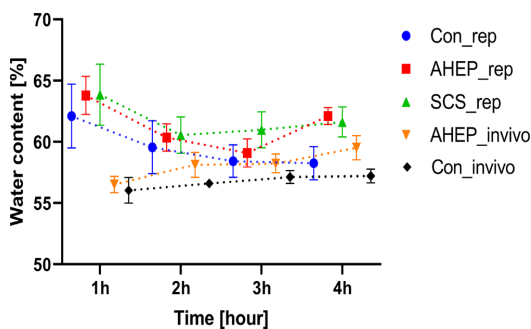
Figure 4. Comparison of calculated mean water content with standard error among the groups: Control, AHEP and SCS during both the NMP and the in vivo phase. "rep" = "reperfusion phase during NMP", "invivo" = "in vivo phase".

increase in weight was the livers in the control group. This result is consistent with the water content estimation showed in Fig. 4 after four hours of NMP.

Discussions

Dielectric measurements were performed in vivo and during NMP on livers from 21 pigs. We compared the dielectric properties from three groups of livers undergoing NMP (healthy liver with no injury, liver with biliary ischemic injury and liver with global hepatic ischemic injury), with the dielectric properties of the in vivo control liver data as reference. Significant differences in the time development of dielectric conductivity were found in vivo in AHEP livers, and after four hours of NMP between all three groups. Analysis of the dielectric data enabled differentiation between injury groups during NMP.

Occlusion of the hepatic artery for four hours leads to gradual injury of the bile ducts, while the parenchyma is preserved[26,27]. Bile duct injury occurs because the biliary tree is supplied mainly by the hepatic artery, whereas the liver parenchyma is supplied by both hepatic artery and through the partially oxygenated blood of the portal vein. Static cold storage causes diffuse liver injury over time because it is a cold ischemic condition. The increased conductivity observed in these livers (AHEP) compared to the control group (Fig. 1b) may be related to an ischemia induced rise in the concentration of larger molecules, like lactate[28] (which is a dipolar molecule). When the concentration of dipolar molecules increases, there will be a higher level of polarization in the tissue, as there are more polarizable molecules present. The dipolar molecules will rotate to follow the alternating electric field, where the rotational movement causes increased energy loss which is directly proportional to the dielectric conductivity. Therefore, we speculate that the increase in the conductivity shown in Fig. 1b is due to an increase in concentration of dipolar molecules.

During the machine perfusion, the largest changes compared to the in vivo control group, occurred after one hour of NMP (Fig. 2a). This was expected as the liver tissue is in an altered condition after static ischemia, cold perfusion and slow rewarming, most possibly leading to an initial reaction that strongly influences the dielectric properties of the liver. After the initial changes that were similar in all three groups, the differences in dielectric properties between the groups increased during the fourth hour of normothermic perfusion. This might be related to the gradually appearing consequences of ischemia-reperfusion injury and the advancing metabolic activity, which was returning in control livers, but was hampered in the intervention groups. As known from other studies on ischemia-reperfusion injury, this is not a binary event, but reperfusion injury is gradually developed based on several processes that occur following the return of oxygenation and sufficient blood flow[29–34]. Following three hours of NMP, the dielectric changes in the SCS group stands out compared to the other groups, which may be related to a higher level of ischemic injury in the SCS group. After four hours of NMP, the dielectric conductivity values of the NMP control group appears to approach the values of the in vivo control group (Fig. 2d).

Our results visualize significant measurement frequency and time dependent differences during NMP between all three groups (Fig. 2d). Based on these results we suggest that the phase with NMP plays an important role in order to be able to evaluate the liver condition, and that four hours of NMP is needed to be able to differentiate between different ischemia-reperfusion liver injuries using DRS. In the upcoming study (on human livers that have been discarded for transplantation), we will investigate if this technique can be applied with shorter machine perfusion time and also study the trends with longer perfusion time (eight hours).

During in vivo normal perfusion, water content is tightly regulated across the tissue, and a balance is upheld between intracellular, extracellular and vascular liquids. Exposure to ischemia and reperfusion injuries influence this balance and affects how liquid is distributed in the tissue[29,30]. This can be in the form of changing the balance between intra- and extra-cellular liquids, as well as congestion of extracellular liquids or formation of edema. Thus, water content and distribution are related to tissue state.

In this study, we propose a method for non-destructive water content quantification, where we use the dielectric properties of deionized water to indirectly calculate the water content in the liver. The reported water content of normal pig liver is 74.5 ± 1.3%[35], 71–75%[36], 64.17%[37] and 69 ± 1.5%[38]. Our DRS based method of water content quantification estimated an average value of 56.05% in the control livers. Underestimation of the liver water content using the DRS method could be due to the fact that water molecules in tissue are influenced/bound by forces from dissolved materials and fixed structures that are not present in deionized water (free and isolated water molecules).

The water molecules in tissue can be polarized by nearby biomolecules and ions, forming sheets around these molecules. Polarized water molecules can again cause polarization in their nearby neighboring molecules. The effect of the polarization on the water molecule is called "slow orientational dynamics"[39]. The slowing down of the orientational dynamics of water molecules associated with ions and biomolecules is mainly due to solvation mechanics (hydrogen bonding, electrostatics, and confinement effects)[39]. Thus, the time constant of the movement of polarized water molecules will be different than that of free water molecules. This influences the frequency dependent behavior of the measured dielectric properties, which may have led to an underestimation of the calculated water content. Most of the water inside living cells have picosecond orientational dynamics[39]. This is consistent with our calculated water relaxation time τ_2 which ranged from 5 to 9 picoseconds.

While acknowledging that our method underestimates the absolute water content, still a comparison of the relative changes of water in the different groups is of interest. We assume that the underestimation affects each group equally and that this method of estimation reveals the changes in water content in the liver tissue over time. The first decreasing trend in the estimated water content parameter for the three groups ex vivo appears from the beginning of NMP, where we believe the initial high water content could be related to the forgoing SCS and cold perfusion. For livers in the AHEP and SCS groups, the decreasing trend was followed by an increasing trend after three and two hours of NMP, respectively. This may be related to ongoing ischemia-reperfusion injury which leads to edema creation[29]. In comparison, the control livers showed a consistent decreasing trend during NMP towards the in vivo levels of the control livers. Likewise, in vivo hepatic artery occlusion leads to a consistent increasing trend of liver water content compared to the control livers and might be the result of the partial ischemia induced by the hepatic artery occlusion. The association between DRS based estimation of liver water content and the measured weight differences between pre- and post-NMP livers, shows that this exploratory method (DRS) for estimating tissue water content can potentially be used to assess the edematous condition of the liver. More experiments with longer machine perfusion time is needed to determine whether use of the estimated water content parameter can have significant clinical impact.

DRS is typically used to characterize solid materials or liquids, and have over the years also been used to characterize biological tissue. Despite the advantages of DRS with the OCP technique, the main challenge associated with this method is the repeatability of the data. One major issue is that there is a large variability in the published dielectric data between different studies and between different measurements on the same tissue[19,40], possibly due to different instrumentation and measurement techniques used. Among the more apparent causes for this variation is the observation that these measurements have been performed under varying conditions, both on ex vivo and in vivo tissue, and at different points in time with respect to tissue perfusion and temperature.

Most DRS studies have been carried out ex vivo, yet the dielectric properties of ex vivo tissue do not necessarily reflect properties of in vivo tissue. Thus, there is a need for comparing dielectric properties of both in vivo and ex vivo tissue from the same subject[24]. This study assessed dielectric parameters of the liver, measured over a wide frequency range, both in vivo and ex vivo, on livers with varying levels of ischemia and reperfusion injury. It may thus serve as reference for future studies aiming at diagnosing liver injury. Knowledge gained from this study enables us to choose optimal measurement frequency regions for future studies. Especially the high frequency region is of interest as we found statistical significant differences between the intervention groups in this region.

Results from this study also indicate that three to four hours of NMP is needed to reliably assess differences in dielectric liver parameters that are associated with pre-existing differences in injury levels and tissue state. In addition, our results can be used to differentiate between liver injury types during NMP and can be a relevant method for enabling an objective evaluation of livers prior transplantation.

In this study, we used the DHOPE-COR-NMP protocol[41] of machine perfusion with the aim to assess livers after an optimal conditioning and reperfusion of the liver graft. The Groningen group established this protocol to allow both restoration of mitochondrial activity during hypothermic preservation, minimize reperfusion injury by gradually rewarming and assessing function during normothermic perfusion, which has been described in clinical trials[11,42].

The intervention groups in this study were established with the aim to evaluate distinct model liver injuries. The intention of using the AHEP model is to create biliary injury, while leaving the liver parenchyma relatively unharmed, as it receives partly oxygenated blood through the portal vein. Due to biliary complications and late onset, non-anastomotic strictures is a major concern in a high proportion of marginal liver grafts, in particular grafts subjected to prolonged warm ischemia, it would be beneficial to have a model to address this complication. Furthermore, AHEP is of interest as it is relevant for the most serious complication following liver transplantation, where thrombosis occurs in the hepatic artery. This model may be comparable to hepatic artery thrombosis which is a well-established cause for bile duct injury in liver transplantation[43]. Thus, we utilized a model with a reproducible extent of biliary ischemic injury through the AHEP model. As for the SCS group, prolonged SCS preservation leads to liver graft injury. We aimed to use this approach to model a standardized, generally injured liver, which is difficult to obtain by other methods.

For livers in the control and AHEP group, a range (1–2 h) of SCS was conducted following explantation. The reason for the small variation of the SCS duration for the livers in both Control and AHEP groups was the different time needed by the surgeons and staff to properly cannulate the liver to the perfusion machine.

Regarding the measurements techniques, the probe was placed on the surface of the liver lobe edge, with a measurement depth sensitivity of a few millimeters, while changes that occur deeper in the tissue could not be detected. The rate and degree of discoloring of the liver surface during normothermic perfusion differed between and within liver lobes. This can be attributed to the pig liver anatomy with its thin and separate lobes rendering it especially vulnerable to inappropriate physical positioning ex vivo, leading to heterogeneous and reduced perfusion of different parts of the liver parenchyma[21,44]. This may have influenced our measured data, as we might not have captured all the variations across the liver, and could also not measure the changes that occurred in the deeper layers of the liver. Regarding the sterility, we believe that this technique has a great potential to be applied in a clinical setting, we are currently testing different sterilization methods, for instance using hydrogen peroxide on the probe itself and a sterile camera drape around most of the probe and the communication wire.

For all three groups, the same temperature was used and maintained. Still, there might have been a slight difference in the surface temperature between in vivo and ex vivo measurements. Small changes in the temperature alone do not explain the observed difference in the dielectric properties for the three groups. In addition, there might be some minor natural differences in the composition of the autologous blood used as perfusate during the machine perfusion. The positioning of the liver graft in the organ chamber of the perfusion machine is also of considerable importance in order not to compromise the circulation of the liver parenchyma, especially due to compression or blockage of the liver vein outflows. The size of the liver could furthermore influence its perfusion, for instance in case of bigger liver grafts leading to self compression of liver parenchyma and/or blood vessels due to heavier weight. The livers used in this study were all very similar and well fitting in size regarding the reservoir space, and the positioning of the liver was standardized with the liver laying on its ventral surface in the machine reservoir, with the liver veins pointing towards the back of the perfusion machine. We acknowledge that there might be small variations in the liver size and physical positioning. Every effort was given to make these as similar as possible, and given that the same protocol was used for all livers during machine perfusion, the above mentioned variations cannot explain the differences in the dielectric properties we observed in this study.

Our measurements were performed on porcine models. Peyman et al.[22] concluded that variation between dielectric properties of liver tissue from human and other species are not greater than variations due to inhomogeneity in each tissue at a range of temperatures. It is challenging to interpret the relationship between the changes in measured conductivity and the specific physiological changes in the liver, since both warm and cold ischemia impose somewhat unpredictable injury on the liver[45]. Categorizing liver ischemia-reperfusion injury is not as straightforward as cirrhosis and steatosis, which present significant visible changes on the liver tissue. Nevertheless, the observed differences between the three groups indicate that DRS has the potential to detect physiological changes in the liver that are not visible to the human eye.

The evaluation of marginal liver grafts is reliant on a comprehensive assessment of liver function. The biliary tree represents the "Achilles heel" of liver transplantation, and although biliary excretory function may be intact, ischemic injury to the biliary tree may manifest late, months after the transplantation. This study is first and foremost a pilot study of how dielectric conductivity assessed by dielectric relaxation spectroscopy is altered in an experimental setting of prolonged static cold storage and biliary ischemic injury in an animal model. Due to the exploratory nature of the study, one of the limitations is that we are not yet able to predict possible clinical benefits compared to the "standard viability assessment" as published in the literature.

This present study serves as a proof of concept, where our goal is to investigate if there are differences in the dielectric properties of livers that can be associated with the injury level of the livers. To the best of our knowledge, this technique has not previously been used on livers in vivo and during machine perfusion, related to liver transplantation. Based on our results, we estimate that this technique has a potential for use in the assessment of ischemia-reperfusion injury in livers. In the next study, we plan to use the DRS technique on human livers that have been discarded for transplantation, where the measurements will be performed in a sterile fashion. We will also use longer perfusion time (eight hours) to study how the dielectric properties change beyond four hours of

NMP. As we collect more data in the future, a machine learning model will be built to automatically process the measured data and give predictions on the liver injury condition. Moreover, we will also compare the present results with measurements performed on human livers and other methods of liver state assessment, including metabolomics, proteomics, emerging machine perfusion quality scores and histology.

Conclusion

This explorative study is the first to investigate and compare the use of the DRS technique on livers in vivo and during machine perfusion. Various degrees of ischemia-reperfusion injury in porcine livers associate with differences in the dielectric properties both in vivo and on NMP. Significant differences in the dielectric properties between healthy control livers, livers with biliary injury induced by hepatic artery occlusion and livers with global hepatic injury were observed after four hours of NMP, indicating that DRS has the potential to be used to assess different levels of liver ischemia-reperfusion injury. We observed a clear increasing trend in the conductivity spectra in the AHEP group during the four-hour in vivo phase while no visual changes could be observed on the liver tissue. The proposed water content estimation approach could be used as a non-invasive method to evaluate levels of liver edema. As this study serves as a proof of concept using a pig model, future studies need to be conducted to further investigate the clinical applicability of this method during liver transplantation, and the translational possibilities on human livers.

Methods

Animals and experimental design.

This study was conducted using 21 Norwegian Landrace pigs (Sus scrofa domesticus), weight range 54–66 kg. Food was withheld 12 hours prior to surgery but the animals had free access to water. The pigs were pre-medicated with ketamine (40 mg/kg), atropine (0.05 mg/kg), and droperidol (0.65 mg/kg) intramuscularly at the animal housing facilities before transporting to the operating room. Pigs were ventilated and sedated with sevoflurane (1–1.5%) and pain relief was achieved with continuous infusion of morphine (0.5–1 mg/kg/h). No muscle relaxants were used and the pigs were continuously assessed for reaction to nose and hoof-pinching pain. A median laparotomy was performed, the liver hilus identified. If applicable, 5000 units of heparin was injected prior to the hepatic artery occlusion. At the end of the four-hour in vivo phase, 32,500 units of heparin were administered, 2–2.5 liters of blood were drained to be used for machine perfusion, and the liver excised followed by flushing of the liver with two liters of IGL-1 (Institut Georges Lopez-1) and consecutively cold storing of the liver graft in the same fluid. After liver explantation, 500 mg of pentobarbital sodium and 40 mmol of potassium chloride were injected intravenously for euthanasia. The study was approved by the Norwegian Food Safety Authority (FOTS 24454) and conducted in accordance with national animal welfare guidelines. All methods are reported in accordance with ARRIVE guidelines (https://arriveguidelines.org).

Three groups were established:

- Control (CON) (N = 7): Four hours in vivo monitoring followed by a short period (one–two hours) of static cold storage before machine perfusion after procurement.
- Biliary injury (AHEP) (N = 7): Four hours of partial warm ischemia with hepatic artery occlusion (where the hepatic artery was fully occluded, while the portal venous flow was intact) prior to liver procurement followed by a short period (one–two hours) of static cold storage before machine perfusion.
- Global hepatic injury (SCS) (N = 7): Four hours in vivo monitoring followed by static cold storage for 18–20 hours prior to machine perfusion.
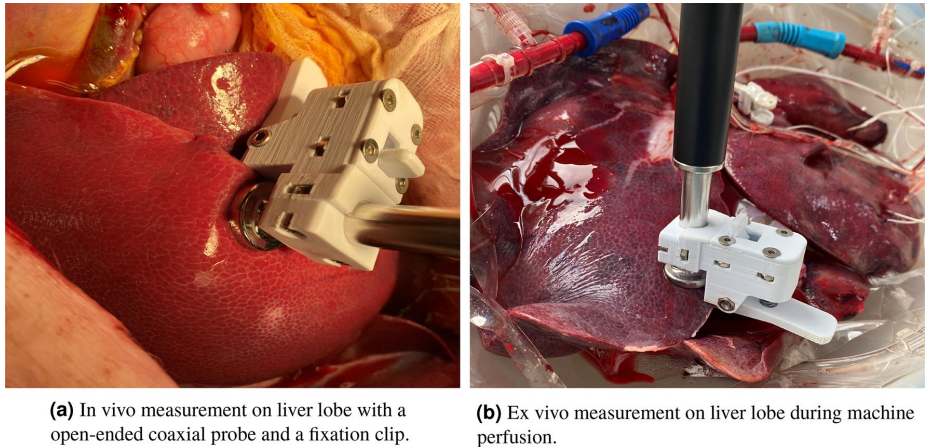
For all groups, the Liver Assist perfusion machine (XVIVO-Abdominal, Groningen, The Netherlands) was used. This perfusion machine consists of a hepatic artery pump and a portal vein pump, both equipped with pressure-controlled centrifugal pumps and connected to hollow fiber oxygenators for dual oxygen reperfusion[46]. The machine is also primed with two liters of pre-cooled Belzer MPS UW Machine Perfusion Solution (Bridge To Life).

All livers underwent machine perfusion as follows:

- One hour of dual hypothermic machine perfusion (DHOPE) for preservation of the liver.
- One hour with controlled oxygenated rewarming (COR) to facilitate a smooth transition from hypothermia to normothermia. The livers was slowly warmed up to 37.5 °C over a period of one hour. This rewarming phase links DHOPE and NMP phases, to help avoiding sudden temperature changes that might cause additional injury to the liver[41].
- Four hours with normothermic machine perfusion (NMP).

The following perfusate solutions were applied in the various phases:

- DHOPE: Pre-cooled Bridge To Life Belzer MPS UW Machine Perfusion Solution.
- COR and NMP: The perfusate solution used during COR and NMP were based on the perfusion fluid of the Groningen DHOPE-COR-NMP protocol[10,41]. A mix of albumin, modified parenteral nutrition, multivitamins for infusion, concentrated trace elements, fast-acting insulin, calcium, sodium bicarbonate and heparin was added to a base of Leukocyte Depleted Whole Blood (LDWB) (composition of the perfusion solution is designed to provide a fluid with physiological colloid osmotic pressure and osmolality). The Groningen protocol has for some time used a hemoglobin-based oxygen carrier (Hemopure) and plasma. We used the

(a) In vivo measurement on liver lobe with a open-ended coaxial probe and a fixation clip.

(b) Ex vivo measurement on liver lobe during machine perfusion.

Figure 5. Experimental setup for both in vivo and ex vivo measurements.

pig's LDWB as oxygen carrier. The component of perfusion solution used during COR and NMP is listed in details in the supplementary file.

During COR, the hepatic artery pressure started with 25 mmHg and was then increased with 10 mmHg every 15 minutes until we reached the upper arterial pressure limit set in our protocol of 55 mmHg by the end of the COR phase (i.e. start of the NMP). The portal vein pressure started at 3 mmHg in the COR phase, was increased to 5 mmHg after 30 min, to 6 mmHg at 45 min and to 7 mmHg at the start of the NMP. Both the hepatic artery pressure and the portal vein pressure were left unchanged throughout the NMP.

During DHOPE, FiO_2 flow was fixed at 100% and gas flow was fixed to a total of 1L/min. During both COR and NMP, FiO_2 and gas flow were adjusted according to the arterial partial pressure of oxygen (pO_2) and venous saturation at the level of the hepatic vena cava, where arterial pO_2 aiming range was 10.0-13.3 kPa and venous saturation 55%-75%.

Permittivity measurements were started when the liver temperature reached 37.5 °C (one hour into NMP) for all groups. Measurements were performed once every hour, during the four-hour in vivo phase and the four-hour NMP phase.

Permittivity measurements.   DRS was performed with a vector network analyzer (VNA) and an open-ended coaxial probe (OCP)[47]. We used the DAK 3.5 (200 MHz–20 GHz) probe (Schmid & Partner Engineering AG, Switzerland) and the R140 (85 MHz–14 GHz) VNA (Copper Mountain Technologies). Combining the frequency limitations of the OCP and the VNA, the frequency range for our experimental setup was 200 MHz–14 GHz. A three point calibration was performed prior to each measurement session ("Open", "Short", and "Load" using deionized water)[48,49]. A 0.1 mol/L saline solution was used as verification liquid[19]. Calibration precision was validated by comparing the measured dielectric properties of saline to the reference published data. The maximum difference between our measured data and the reference data with respect to saline was ±2%. A new reference liquid was used for each experiment to ensure the accuracy of the calibration. Calibration was re-performed prior to each hourly measurement to maintain the accuracy of the VNA and minimize the drift error. Another systematic error associated with the performance of the system is the cable tolerance. This error is assumed to be negligible since the VNA and the probe are mechanically well fixed (without any movable cables between the VNA and the probe) during the whole experiment.

To provide an accurate characterization of the dielectric parameters, 20 measurements were made, on two different random locations of the liver (10 measurements on each location), to obtain high measurement accuracy. The measured data (10×2) were averaged over the measured frequency range for each of the livers. To ensure that the same pressure was applied to all liver samples, a metal stand that holds both the VNA and the probe and a 3D printed clip that fits the tip of the coaxial probe were used. The liver lobe was slightly clamped between the clip and the probe surface to ensure good contact (avoid partial contact and air bobbles) and constant pressure. Erroneous measurements resulting from probe movements were efficiently minimized with the rigid support of the stand. Prior to each measurement, the measurement site was gently wiped with a sterile cloth to avoid body fluid oozing under the probe contact area and any possible contamination. After placing the probe on the liver tissue, we waited 30 seconds before starting the measurement. This was to ensure an equilibrium between the temperature of the probe tip and the liver tissue. Figure 5 shows the experimental setup for both in vivo and ex vivo measurements.

Permittivity data analysis. Two processes (energy storage and energy dissipation) take place when the material interacts with the microwave. Dipoles in the biological sample polarize in response to the alternating electric field causing energy storage. Complex permittivity is used to express the dielectric properties of a material as Eq. (1) shows[50].

$$\varepsilon^* = \varepsilon' - j\varepsilon'' = \varepsilon' - j\frac{\sigma}{\varepsilon_0 2\pi f} \tag{1}$$

where the real part ε' is the dielectric constant which represents the energy storage and the imaginary part ε'' is the dielectric loss which represents the energy dissipation (dissipated in the form of heat). σ is the dielectric conductivity which represents the energy loss associated with the dispersion of ε'', whenever "conductivity" is mentioned in this paper, it refers to "dielectric conductivity" which is proportional to the energy loss (Eq. (1)). ε_0 is the vacuum permittivity.

Relative change in the conductivity was calculated as follows:

$$\Delta\sigma = \frac{\sigma - \sigma_{\text{control}}}{\sigma_{\text{control}}} \times 100\%. \tag{2}$$

The reference data (σ_{control}) used was measured in vivo, One hour after the liver was made accessible through midline laparotomy in the abdominal cavity. The reference data represents the dielectric properties of the liver in the in vivo phase, where the liver is perfused and have a stable temperature and humidity. For the rest of the data analysis, the following procedures were performed; we first averaged all measurements that had been performed at different locations on the same liver into one average representing that individual liver. We then averaged these individually representative averages from all livers within the same group, to calculate the standard error (N = 7 for each group). For statistical analysis, two-way ANOVA with multiple comparisons and Sidak correction were used.

To simplify the expression of measured permittivity data, a two-pole Cole–Cole equation[51] (Eq. (3)) was used to model the experimental data, and thus estimate the dielectric parameter values. When water molecules are mixed with other biological substances, there is a broadening of the spectrum which corresponds to a distribution of relaxation times. Therefore, the Cole–Cole model was chosen as it takes account of the distribution of relaxation times when used to describe the dielectric relaxation of biological materials. In the liver tissue, there are protein-bound water, proteins and organic acids like lactate, which will contribute to the measured dielectric properties in addition to the contribution from water molecules[52–54]. Considering that the dielectric properties in the measurement frequency range (200 MHz–14 GHz) include both the β- and γ-dispersion, and the dispersion regions overlap[55], we choose to use a two-pole Cole–Cole model. The chosen model takes account of both the contribution from water molecules that dominate in the higher frequency region and other molecules which are larger than water molecules that dominate in the lower frequency region. The Levenberg-Marquardt algorithm based on the non-linear least-square method was used during fitting. The two-pole Cole–Cole model can be written as:

$$\varepsilon^*(\omega) = \varepsilon_\infty + \frac{\Delta\varepsilon_1}{1 + (j\omega\tau_1)^{1-\alpha_1}} + \frac{\Delta\varepsilon_2}{1 + (j\omega\tau_2)^{1-\alpha_2}} \tag{3}$$

where $\Delta\varepsilon_1 = \varepsilon_s - \varepsilon_1$ and $\Delta\varepsilon_2 = \varepsilon_1 - \varepsilon_\infty$ are the relaxation strength. The relaxation strength is proportional to the area under the dielectric loss peak. τ_1 and τ_2 are the relaxation times. τ provides information of molecular motions and their relations to the molecule sizes, shapes and the internal friction between molecules caused by the intramolecular forces. The parameters $\varepsilon_\infty, \tau_1, \tau_2, \Delta\varepsilon_1, \Delta\varepsilon_2, \alpha_1, \alpha_2$ can be obtained by fitting the experimental permittivity data to Eq. (3). The averaged permittivity data from each individual liver was used to fit to the Cole–Cole model (Eq. (3)). Seven curve fittings were performed for data from each of the injury groups and the extracted Cole–Cole parameters together with the uncertainty estimates are reported in the supplementary material.

Quantification of water content in percent was performed based on the measured dielectric loss of the deionized water, and the measured dielectric loss data of the liver. The ratio of water contribution in the liver and water contribution of the deionized water was used to estimate the water content as Eq. (4) shows:

$$\text{water content}[\%] = \frac{\sum[\varepsilon''(\text{water contribution in liver})]}{\sum[\varepsilon''(\text{deionized water})]} \times 100\% \tag{4}$$

By summing over the dielectric loss curve for the measured deionized water ($\sum[\varepsilon''(\text{deionized water})]$) and the separated water contribution in the liver ($\sum[\varepsilon''(\text{water contribution in the liver})]$) from the separated high frequency dispersion using the two-pole Cole–Cole model, we were able to estimate the water content.

Data availability

The datasets used and analysed during the current study available from the corresponding author on reasonable request.

References

1. Williams, W. W. & Markmann, J. F. Warming up to cold perfusion. *N. Engl. J. Med.* **384**, 1458–1459. https://doi.org/10.1056/NEJMe2102056 (2021).
2. Zamperetti, N., Bellomo, R., Piccinni, P. & Ronco, C. Reflections on transplantation waiting lists. *Lancet* **378**, 632–635. https://doi.org/10.1016/S0140-6736(10)62343-4 (2011).
3. Monbaliu, D., Pirenne, J. & Talbot, D. Liver transplantation using donation after cardiac death donors. *J. Hepatol.* **56**, 474–485. https://doi.org/10.1016/j.jhep.2011.07.004 (2012).
4. Mihaylov, P. *et al.* Expanding the donor pool with the use of extended criteria donation after circulatory death livers. *Liver Transpl.* **25**, 1198–1208. https://doi.org/10.1002/lt.25462 (2019).
5. Minor, T. & von Horn, C. Rewarming injury after cold preservation. *Int. J. Mol. Sci.* **20**, 2059. https://doi.org/10.3390/ijms20092059 (2019).
6. Mergental, H. *et al.* Transplantation of discarded livers following viability testing with normothermic machine perfusion. *Nature Communications* **11**, 2939, https://doi.org/10.1038/s41467-020-16251-3 . Bandiera_abtest: a Cc_license_type: cc_by Cg_type: Nature Research Journals Number: 1 Primary_atype: Research Publisher: Nature Publishing Group Subject_term: Diagnostic markers;Liver Subject_term_id: diagnostic-markers;liver. (2020)
7. Sutton, M. E. *et al.* Criteria for viability assessment of discarded human donor livers during ex vivo normothermic machine perfusion. *PLoS ONE* **9**, e110642. https://doi.org/10.1371/journal.pone.0110642 (2014).
8. op den Dries, S. *et al.* Ex vivo normothermic machine perfusion and viability testing of discarded human donor livers. *Am. J. Transpl.* **13**, 1327–1335. https://doi.org/10.1111/ajt.12187 (2013).
9. Watson, C. J. E. & Jochmans, I. From, gut feeling to objectivity: Machine preservation of the liver as a tool to assess organ viability. *Curr. Transpl. Rep.* **5**, 72–81. https://doi.org/10.1007/s40472-018-0178-9 (2018).
10. van Leeuwen, O. B. *et al.* Transplantation of high-risk donor livers after ex situ resuscitation and assessment using combined hypo- and normothermic machine perfusion: A prospective clinical trial. *Ann. Surg.* **270**, 906–914. https://doi.org/10.1097/SLA.0000000000003540 (2019).
11. van Leeuwen, O. B., de Vries, Y., de Meijer, V. E. & Porte, R. J. Hypothermic machine perfusion before viability testing of previously discarded human livers. *Nat. Commun.* **12**, 1008. https://doi.org/10.1038/s41467-021-21182-8 (2021).
12. Watson, C. J. E. *et al.* Observations on the ex situ perfusion of livers for transplantation. *Am. J. Transplant. Off. J. Am. Soc. Transplant. Am. Soc. Transplant Surg.* **18**, 2005–2020. https://doi.org/10.1111/ajt.14687 (2018).
13. Graham, J. A. & Guarrera, J. V. Resuscitation of marginal liver allografts for transplantation with machine perfusion technology. *J. Hepatol.* **61**, 418–431. https://doi.org/10.1016/j.jhep.2014.04.019 (2014).
14. Schlegel, A., Muller, X. & Dutkowski, P. Machine perfusion strategies in liver transplantation. *Hepatob. Surg. Nutr.* **8**, 490–501. https://doi.org/10.21037/hbsn.2019.04.04 (2019).
15. Xin, L., Xiuzhen, D. & Feng, F. Study on changes of characteristic parameters of biological tissues impedance spectroscopy in vitro within 5 to 360 min after excision at the frequency range from 1Hz to 1MHz. In *2005 IEEE Engineering in Medicine and Biology 27th Annual Conference*, 1123–1126, https://doi.org/10.1109/IEMBS.2005.1616618 ISSN: 1558-4615. (2005)
16. Ahn, H., Shin, H., Yun, S., Kim, J. & Choi, J. Measurement of bioimpedance and cell viability during ischemia-reperfusion in the rat liver. In *2005 IEEE Engineering in Medicine and Biology 27th Annual Conference*, 1945–1947, https://doi.org/10.1109/IEMBS.2005.1616833 . ISSN: 1558-4615. (2005)
17. Gersing, E. Impedance spectroscopy on living tissue for determination of the state of organs. *Bioelectrochem. Bioenerg.* **45**, 145–149. https://doi.org/10.1016/S0302-4598(98)00079-8 (1998).
18. Gabriel, S., Lau, R. W. & Gabriel, C. The dielectric properties of biological tissues: II. Measurements in the frequency range 10 Hz to 20 GHz. *Phys. Med. Biol.* **41**, 2251–2269. https://doi.org/10.1088/0031-9155/41/11/002 (1996).
19. Abdilla, L., Sammut, C. & Mangion, L. Z. Dielectric properties of muscle and liver from 500 MHz–40 GHz. *Electromagn. Biol. Med.* **32**, 244–252. https://doi.org/10.3109/15368378.2013.776436 (2003).
20. O'Rourke, A. P. *et al.* Dielectric properties of human normal, malignant and cirrhotic liver tissue: in vivo and ex vivo measurements from 0.5 to 20 GHz using a precision open-ended coaxial probe. *Phys. Med. Biol.* **52**, 4707–4719. https://doi.org/10.1088/0031-9155/52/15/022 (2007).
21. Farrugia, L., Wismayer, P. S., Mangion, L. Z. & Sammut, C. V. Accurate in vivo dielectric properties of liver from 500 MHz to 40 GHz and their correlation to ex vivo measurements. *Electromagn. Biol. Med.* **35**, 365–373. https://doi.org/10.3109/15368378.2015.1120221 (2016).
22. Peyman, A. *et al.* Variation in dielectric properties due to pathological changes in human liver. *Bioelectromagnetics* **36**, 603–612. https://doi.org/10.1002/bem.21939 (2015).
23. Hou, J. *et al.* Small intestinal viability assessment using dielectric relaxation spectroscopy and deep learning. *Sci. Rep.* **12**, 3279. https://doi.org/10.1038/s41598-022-07140-4 (2022).
24. Egot-Lemaire, S., Pijanka, J., Sulé-Suso, J. & Semenov, S. Dielectric spectroscopy of normal and malignant human lung cells at ultra-high frequencies. *Phys. Med. Biol.* **54**, 2341–2357. https://doi.org/10.1088/0031-9155/54/8/006 (2009).
25. Nykonenko, A., Vávra, P. & Zonča, P. Anatomic peculiarities of pig and human liver. *Exp. Clin. Transpl.* **15**, 21–26 (2017).
26. Low, G. *et al.* Imaging of vascular complications and their consequences following transplantation in the abdomen. *Radiographics* **33**, 633–652 (2013).
27. Cursio, R. & Gugenheim, J. Ischemia-reperfusion injury and ischemic-type biliary lesions following liver transplantation. *J. Transpl.* **2012**, 2 (2012).
28. Pischke, S. E. *et al.* Hepatic and abdominal carbon dioxide measurements detect and distinguish hepatic artery occlusion and portal vein occlusion in pigs. *Liver Transpl.* **18**, 1485–1494. https://doi.org/10.1002/lt.23544 (2012).
29. Kalogeris, T., Baines, C. P., Krenz, M. & Korthuis, R. J. Cell biology of ischemia/reperfusion injury. *Int. Rev. Cell Mol. Biol.* **298**, 229–317. https://doi.org/10.1016/B978-0-12-394309-5.00006-7 (2012).
30. Carden, D. L. & Granger, D. N. Pathophysiology of ischaemia-reperfusion injury. *J. Pathol.* **190**, 255–266 (2000).
31. Cowled, P. & Fitridge, R. Pathophysiology of Reperfusion Injury. In Fitridge, R. & Thompson, M. (eds.) *Mechanisms of Vascular Disease: A Reference Book for Vascular Specialists* (University of Adelaide Press, Adelaide (AU)), (2011).
32. Olivas, T. P., Saylor, T. F., Wong, H. P., Stephenson, L. L. & Zamboni, W. A. Timing of microcirculatory injury from ischemia reperfusion. *Plast. Reconstr. Surg.* **107**, 785–788. https://doi.org/10.1097/00006534-200103000-00020 (2001).
33. Jaeschke, H. Molecular mechanisms of hepatic ischemia-reperfusion injury and preconditioning. *Am. J. Physiol. Gastrointest. Liver Physiol.* **284**, 15–26. https://doi.org/10.1152/ajpgi.00342.2002 (2003).
34. González-Flecha, B., Cutrin, J. C. & Boveris, A. Time course and mechanism of oxidative stress and tissue damage in rat liver subjected to in vivo ischemia-reperfusion. *J. Clin. Investig.* **91**, 456–464. https://doi.org/10.1172/JCI116223 (1993).
35. Galmarini, D., Fassati, L. R., Paoletti, R. & Sherlock, S. *Drugs and the Liver: High Risk Patients and Transplantation* (Springer Science & Business Media, 2012).
36. Clemmer, J. *et al.* Experimental observation of high strain rate responses of porcine brain, liver, and tendon. *J. Mech. Med. Biol.* **16**, 1650032. https://doi.org/10.1142/S0219519416500329 (2016).

37. Su, G. *et al.* Thermal characterization and ice crystal analysis in pressure shift freezing of different muscle (shrimp and porcine liver) versus conventional freezing method. *Innov. Food Sci. Emerg. Technol.* **26**, 40–50. https://doi.org/10.1016/j.ifset.2014.05.006 (2014).

38. Zhu, D., Luo, Q. & Cen, J. Effects of dehydration on the optical properties of in vitro porcine liver. *Lasers Surg. Med.* **33**, 226–231. https://doi.org/10.1002/lsm.10215 (2003).

39. Tros, M. *et al.* Picosecond orientational dynamics of water in living cells. *Nature Communications* **8**, 904, https://doi.org/10.1038/s41467-017-00858-0 . Bandiera_abtest: a Cc_license_type: cc_by Cg_type: Nature Research Journals Number: 1 Primary_atype: Research Publisher: Nature Publishing Group Subject_term: Biophysical chemistry;Chemical physics;Kinetics Subject_term_id: biophysical-chemistry;chemical-physics;kinetics. (2017)

40. Yilmaz, T. *et al.* Machine learning aided diagnosis of hepatic malignancies through in vivo dielectric measurements with micro-waves. *Phys. Med. Biol.* **61**, 5089–5102. https://doi.org/10.1088/0031-9155/61/13/5089 (2016).

41. de Vries, Y. *et al.* Transplantation of high-risk donor livers after resuscitation and viability assessment using a combined protocol of oxygenated hypothermic, rewarming and normothermic machine perfusion: study protocol for a prospective, single-arm study (DHOPE-COR-NMP trial). *BMJ Open* **9**, e028596. https://doi.org/10.1136/bmjopen-2018-028596 (2019).

42. de Vries, Y. *et al.* Pretransplant sequential hypo- and normothermic machine perfusion of suboptimal livers donated after circula-tory death using a hemoglobin-based oxygen carrier perfusion solution. *Am. J. Transplant. Off. J. Am. Soc. Transplant. Am. Soc. Transplant Surg.* **19**, 1202–1211. https://doi.org/10.1111/ajt.15228 (2019).

43. de Jong, I. E. M. *et al.* Persistent biliary hypoxia and lack of regeneration are key mechanisms in the pathogenesis of posttransplant nonanastomotic strictures. *Hepatology* **75**, 814–830. https://doi.org/10.1002/hep.32166 (2022).

44. Raicu, V., Saibara, T. & Irimajiri, A. Dielectric properties of rat liver in vivo: a noninvasive approach using an open-ended coaxial probe at audio/radio frequencies. *Bioelectrochem. Bioenerg.* **47**, 325–332. https://doi.org/10.1016/S0302-4598(98)00171-8 (1998).

45. Watson, C. J. E. *et al.* Normothermic Perfusion in the Assessment and Preservation of Declined Livers Before Transplantation: Hyperoxia and Vasoplegia-Important Lessons From the First 12 Cases. *Transplantation* **101**, 1084–1098. https://doi.org/10.1097/TP.0000000000001661 (2017).

46. van Rijn, R. *et al.* Dual hypothermic oxygenated machine perfusion in liver transplants donated after circulatory death. *Br. J. Surg.* **104**, 907–917. https://doi.org/10.1002/bjs.10515 (2017).

47. Gregory, A. P. & Clarke, R. N. Dielectric metrology with coaxial sensors. *Meas. Sci. Technol.* **18**, 1372–1386. https://doi.org/10.1088/0957-0233/18/5/026 (2007).

48. Kaatze, U. Complex permittivity of water as a function of frequency and temperature. *J. Chem. Eng. Data* **34**, 371–374. https://doi.org/10.1021/je00058a001 (1989).

49. Ellison, W. J. Permittivity of pure water, at standard atmospheric pressure, over the frequency range 0–25thz and the temperature range 0–100°C. *J. Phys. Chem. Reference Data* **36**, 1–18. https://doi.org/10.1063/1.2360986 (2007).

50. Grimnes, S. & Martinsen, O. G. *Bioimpedance and Bioelectricity Basics. Academic Press 3rd Edition. ISBN 978-0-12-411533-0.*

51. Cole, K. S. & Cole, R. H. Dispersion and absorption in dielectrics. I. Alternating current characteristics. *J. Chem. Phys.* **9**, 341–351. https://doi.org/10.1063/1.1750906 (1941).

52. Pethig, R. Dielectric properties of body tissues. *Clin. Phys. Physiol. Meas.* **8**, 5–12. https://doi.org/10.1088/0143-0815/8/4A/002 (1987).

53. Schwan, H. P. Electrical properties of tissues and cell suspensions: mechanisms and models. In *Proceedings of 16th Annual Interna-tional Conference of the IEEE Engineering in Medicine and Biology Society*, vol. 1, A70–A71 vol.1, https://doi.org/10.1109/IEMBS.1994.412155 (1994).

54. Liewei Sha, Ward, E. R. & Stroy, B. A review of dielectric properties of normal and malignant breast tissue. In *Proceedings IEEE SoutheastCon 2002 (Cat. No.02CH37283)*, 457–462, https://doi.org/10.1109/SECON.2002.995639 (2002).

55. Polk, C. *CRC Handbook of Biological Effects of Electromagnetic Fields* (CRC Press). Google-Books-ID: 3TSoDwAAQBAJ. (2019).

Acknowledgements

Author contributions

Study design and data collection J.H., O.M.I.L, I.H.F, S.E.P, P.D.L, M.H, and R.S.A.; data analysis and program-ming J.H.; conceptualization, J.H., R.S.A, O.M.I.L, I.H.F and S.E.P; methodology, J.H. and R.S.A.; writing the original draft, J.H.; writing-review, J.H., R.S.A, O.M.I.L, I.H.F, S.E.P, T.I.T, Ø.G.M., P.D.L, M.H, and J.O.H.; fund-ing acquisition, S.E.P. All authors have read and agreed to the published version of the manuscript.

Funding

Competing interests

The authors declare no competing interests.

Additional information

Supplementary Information The online version contains supplementary material available at https://doi.org/10.1038/s41598-022-14817-3.

Correspondence and requests for materials should be addressed to J.H.

Reprints and permissions information is available at www.nature.com/reprints.

Paper V

Assessment of intestinal ischemia-reperfusion injury using diffuse VIS-NIR spectroscopy and histology

Jie Hou, Siri Schøne Ness, Jon Tschudi, Marion O'Farrell, Rune Veddegjerde, Ørjan Grøttem Martinsen, Tor Inge Tønnessen, Runar Strand-Amundsen

V

Assessment of Intestinal Ischemia–Reperfusion Injury Using Diffuse Reflectance VIS-NIR Spectroscopy and Histology

Jie Hou [1,2,*], Siri Schøne Ness [3], Jon Tschudi [4], Marion O'Farrell [4], Rune Veddegjerde [5], Ørjan Grøttem Martinsen [1,2], Tor Inge Tønnessen [6,7] and Runar Strand-Amundsen [2,5]

[1] Department of Physics, University of Oslo, Sem Sælands vei 24, 0371 Oslo, Norway
[2] Department of Clinical and Biomedical Engineering, Oslo University Hospital, 0424 Oslo, Norway
[3] Department of Pathology, The Norwegian Radium Hospital, Oslo University Hospital, Ullernchausseen 70, 0379 Oslo, Norway
[4] SINTEF AS, Smart Sensors and Microsystems, Forskningsveien 1, 0373 Oslo, Norway
[5] Sensocure AS, Langmyra 11, 3185 Skoppum, Norway
[6] Department of Emergencies and Critical Care, Oslo University Hospital, 0424 Oslo, Norway
[7] Institute of Clinical Medicine, University of Oslo, 0318 Oslo, Norway
* Correspondence: jieho@fys.uio.no

Abstract: A porcine model was used to investigate the feasibility of using VIS-NIR spectroscopy to differentiate between degrees of ischemia–reperfusion injury in the small intestine. Ten pigs were used in this study and four segments were created in the small intestine of each pig: (1) control, (2) full arterial and venous mesenteric occlusion for 8 h, (3) arterial and venous mesenteric occlusion for 2 h followed by reperfusion for 6 h, and (4) arterial and venous mesenteric occlusion for 4 h followed by reperfusion for 4 h. Two models were built using partial least square discriminant analysis. The first model was able to differentiate between the control, ischemic, and reperfused intestinal segments with an average accuracy of 99.2% with 10-fold cross-validation, and the second model was able to discriminate between the viable versus non-viable intestinal segments with an average accuracy of 96.0% using 10-fold cross-validation. Moreover, histopathology was used to investigate the borderline between viable and non-viable intestinal segments. The VIS-NIR spectroscopy method together with a PLS-DA model showed promising results and appears to be well-suited as a potentially real-time intraoperative method for assessing intestinal ischemia–reperfusion injury, due to its easy-to-use and non-invasive nature.

Keywords: small intestine; VIS-NIR spectroscopy; ischemia–reperfusion injury; histopathology

1. Introduction

Insufficient blood supply (ischemia) to the small intestine often requires invasive surgery to restore the supply. Early detection and correction of the ischemic intestinal segment is the most important factor for patient survival [1]. The standard clinical method for assessing small intestinal ischemia is based on a subjective visual and tactile evaluation of the tissue, such as observing changes in color, the occurrence of peristalsis or a change in the thickness of the intestinal wall [1–3]. This method has low initial accuracy, which can often lead to a second-look surgery, where the questionable segments are re-examined within 24–72 h after the original surgery. It would be a significant improvement to patient treatment if a more reliable method to detect irreversible ischemia could be established. This study is part of the work that explores more reliable, objective methods for gastrointestinal surgeons.

Over the years, various experimental approaches have been investigated to help increase the accuracy when assessing intestinal viability, including fluorescein and laser Doppler flowmetry [4–6]. The fluorescein technique has a low detection threshold and is affected by tissue autofluorescence, which will generate background noise and false

123

signal [7]. The laser Doppler flowmetry is sensitive to motion artifacts and blood pressure changes [8], and large standard deviations in the flow parameter make continuous measurement necessary [8–10]. Moreover, intraoperative Doppler ultrasound has been applied to determine the adequacy of blood supply in the small intestine [11]. High false-negative and false-positive rates were observed using Doppler ultrasonography [12]. Microdialysis as a minimally invasive approach has been investigated by Deeba et al. [13], where they monitored the glucose and lactate concentrations. Implanting the microdialysis catheter near the bowel segment for postoperative monitoring was suggested by the authors. More recently, Strand-Amundsen et al. [14] further investigated the feasibility of microdialysis by monitoring the concentration change in the intraluminal lactate and glycerol. They were unable to find a sufficient level of association between intestinal viability and the metabolic markers, to conclude the clinical relevance of microdialysis with respect to the assessment of tissue viability. Most of the above-mentioned experimental approaches focus on blood flow. There are only a few studies that focus on the viability outcome of the ischemia–reperfusion injured intestine. Recently, Strand-Amundsen et al. [15] used bioimpedance measurements together with machine learning algorithms (LSTM-RNN) to more accurately assess intestinal viability in a pig model. Some years later, Hou et al. [16] used bioimpedance measurements on human intestine ex vivo, reporting an association between the P_y value from the bioimpedance data and the viability of the small intestine. Moreover, Hou et al. [3] investigated the use of dielectric relaxation spectroscopy together with machine learning methods (LSTM and CNN) to assess small intestinal viability.

Visible and Near-Infrared (VIS-NIR) spectroscopy can potentially be used to assess intestinal ischemia–reperfusion injury objectively, without the need for a contrast agent [5,17,18]. As the blood flow is blocked during ischemia, the oxygenated haemoglobin levels will decrease, whereas deoxygenated haemoglobin levels increase, and this will be reversed during the reperfusion phase. Oxygenated haemoglobin and deoxygenated haemoglobin have spectral features in the wavelength range from 500–1000 nm. Therefore, information related to ischemia–reperfusion injury should be present in the VIS-NIR reflectance spectrum of the intestinal tissue. Pulse oximetry is a non-invasive method that compares the signals at 660 nm and 940 nm to monitor blood oxygenation (SpO_2). Traditional pulse oximetry is dependent on the inherent alternating component of the signal, which is present when there is an active and strong arterial pulse in the tissue, to correctly calculate SpO_2. VIS-NIR diffuse reflectance spectroscopy, on the other hand, is not dependent on the pulsative signal and can also work in conditions with little or no pulse, such as ischemia or reperfusion.

VIS-NIR spectroscopy has been investigated in several earlier studies. Sowa et al. [1] used near-infrared spectroscopy to detect intestinal ischemia in a porcine model in the wavelength range 500–1000 nm. They compared the reflectance spectra from control (no vascular manipulation), ischemic (arterial/venous occlusion up to 90 min) and reperfused (up to 60 min) intestinal segments. Furthermore, a classification model built using PLS-DA was used to differentiate between the control and ischemic segments, where the overall classification accuracy was 89%. Karakas et al. [5] investigated the viability of the intestine in a rat model using diffuse reflectance spectroscopy in the wavelength range 450–750 nm, where they focused on the ratio of the absorption between wavelengths at 560 nm and at 577 nm. Furthermore, they correlated this ratio to the histopathological grading with an 8-point Park/Chiu score.

This study investigates the feasibility of VIS-NIR diffuse reflectance spectroscopy in assessing the small intestinal ischemia–reperfusion injury. Compared to the above-mentioned studies, the contribution of this study includes: (1) The method is non-invasive and does not require applying any active signal or agent to the patient (can simplify the approval process of a medical device). (2) With the DR-probe, the measurement field of view is large and the measurement site is isolated from ambient room light, which gives high reproducibility of the experiment/data compared to "single point" measurements. It is much simpler and faster to scan/measure a large part of the small intestine with this

probe, compared to the previously reported "point" measurements. (3) Reflectance data over a wide wavelength range together with the PLS-DA model provide high prediction accuracy in viability assessment, which is highly clinically relevant. Different models were built for different datasets. By comparing them, a better understanding of the spectral wavelength response during ischemia–reperfusion was gained. An accurate and objective method of detecting viable versus non-viable intestinal tissue would provide surgeons with a decision support tool for resection margins. This could potentially reduce the need for a second-look surgery, contributing to a better prognosis for the patient.

2. Methods

2.1. Animals and Experimental Design

Ten Norwegian Landrace pigs were included in this study, with a weight range of 48–54 kg, and three were female. The pigs were normal, healthy pigs and were screened by a professional pig breeder, to avoid disease. Food was withheld 12 h prior to surgery. The same experimental protocol was used as described by Strand-Amundsen et al. and Hou et al. [2,3,19]. For each pig, four random segments of jejunum were selected for the four cases of the protocol:

- **Case 1**: Control (Reference)—8 h of normal perfusion;
- **Case 2**: Ischemia—8 h of warm full ischemia;
- **Case 3**: 2 h of ischemia followed by 6 h of reperfusion;
- **Case 4**: 4 h of ischemia followed by 4 h of reperfusion.

Ischemia was induced by clamping the arteries and veins of the jejunal mesentery of the selected segments, resulting in a 30 cm central zone of warm ischemia and two surrounding edge zones of marginal tissue hypoxia [2,19]. The time durations for segment Case 3 and segment Case 4 were chosen based on histological analysis, which predicts that irreversible injury is estimated to occur after around 2 h of ischemia. In-vivo spectroscopic measurements were conducted hourly over an 8-hour period. All samples received the same treatment, while ischemic exposure varied dependent on the protocol. Prior to implementing the protocol, a couple of pigs were selected for histological analysis, where biopsy samples were taken from all the aforementioned cases, in addition to a case with 3 h of ischemia and 5 h of reperfusion. This was accomplished in order to follow the time sequence of the ischemia changes more closely. After the experiment, the animals were euthanized by a lethal dose of potassium chloride (100 mmol). The experiment was approved by the Norwegian Food Safety Authority (NFSA) and conducted in accordance with national animal welfare guidelines.

### 2.2. Visible and Near-Infrared Diffuse Reflectance Spectroscopy Setup

Visible and near-infrared diffuse reflectance spectroscopy uses light and matter interaction to detect and determine the composition of organic substances. Light interacts with various molecules (e.g., water, fat, hemoglobin, lactate, glucose) in the tissue and the molecules behave and absorb visible and near-infrared light differently. The amount of light absorbed is linearly proportional to the concentration of that particular molecule, revealing both qualitative and quantitative information about the pathological process under investigation. Histopathological correlation with diffuse reflectance spectroscopy of tissue can be used to build a prediction model to detect and distinguish different tissue conditions [20].

The VIS-NIR measurements were performed using a handheld USB 2000+VIS-NIR (USB2+H00178) spectrometer (Ocean Insight, Orlando, FL, USA). It was operated in reflectance mode in the wavelength range 475–1100 nm with a 25 μm slit for optical resolution of 1.5 nm (full width at half maximum). The spectrometer was connected to the QP600-2-VIS-NIR fiber (Ocean Insight, Orlando, FL, USA) with wavelength range 400–2100 nm and the TC-DR probe (Ocean Insight, Orlando, FL, USA) which is a 45° diffuse reflectance probe with integrated tungsten halogen light source (6 watts). The TC-DR probe has a 40 mm stand-off block ensuring consistent focal length and the field of view is 24 mm × 47 mm. Be-

fore acquiring the time series of in vivo diffuse reflectance data, two spectra were collected for the system calibration. The first one was the reference spectrum ($R(\lambda)$) measured using a spectralon reflectance standard with high reflectivity while the light source was turned on. The second spectrum acquired was the background spectrum ($D(\lambda)$) taken while the light source was turned off. The percentage reflectance as a function of wavelength ($T(\lambda)$) was calculated as follows:

$$\%T(\lambda) = \frac{S(\lambda) - D(\lambda)}{R(\lambda) - D(\lambda)} \times 100\% \tag{1}$$

where $S(\lambda)$ is the sample intensity as a function of wavelength λ. All of the spectra were acquired with the OceanView software. Boxcar smoothing was set to 5, averaging was set to 50 scans, and each scan was taken with 3740 μs integration time. The system was re-calibrated prior to each hourly measurement to maintain the accuracy of the system and minimize the drift error. Prior to each measurement, the small intestinal segment was gently wiped with a sterile cloth to avoid body fluid oozing under the area covered by the TC-DR probe and any possible contamination. After each hourly measurement, the abdomen was closed using several Backhaus towel clamps to minimize fluid and heat losses. Every hour, each intestinal segment was measured three times, at three different locations. Figure 1 shows the experimental setup for in vivo measurements.
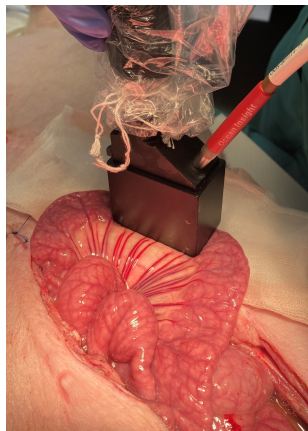
Figure 1. Experimental setup for in vivo measurements of a control small intestinal segment with the TC-DR probe.

2.3. Data Analysis and Classification

To minimize variations in the diffuse reflectance spectra induced by light scattering (due to, for instance, textural differences) and the different positions of each measurement, the spectra were normalized by standard normal variate (SNV). For each reflectance spectrum, the mean value was subtracted and then divided by the standard deviation of the spectrum, to transform the data to have mean $\mu = 0$ and standard deviation $\sigma = 1$ using Equation (2):

$$Z = \frac{X - \mu}{\sigma} \tag{2}$$

A first-order derivative was applied to the standardized data to remove the baselines. Savitzky–Golay (SG) polynomial derivative filters were applied during derivation (the length of the filter window was set to 25). It applies a smoothing function to the spectra before calculating the derivative, to decrease the detrimental effect on the signal-to-noise ratio that conventional finite-difference derivatives would have [21].

Partial least squares-discriminant analysis (PLS-DA) was used to classify the measured diffuse reflectance spectra in the wavelength range 500–1000 nm. Data from different tissue conditions were labelled and two models were built; one performed classification of three classes (control, ischemic, and reperfused intestinal tissue); the other performed classification of two classes (viable and non-viable intestinal tissue). The viable and non-viable classes were determined based on the histopathological analysis. The viable class included data from the control case, ischemia ≤ 2 h, and reperfusion data from those which had previously been ischemic for ≤ 2 h. The rest of the data (ischemia > 2 h and reperfusion data from those which had previously been ischemic for >2 h) were classified as non-viable as Table 1 shows.

Table 1. Overview of cases and viability. The white background indicates control with normal perfusion, the blue background indicates ischemia, and the red background indicates reperfusion.

Hours	Case 1	Case 2	Case 3	Case 4
1–2	Viable	Viable	Viable	Viable
3–4	Viable	Non-viable	Viable	Non-viable
5–6	Viable	Non-viable	Viable	Non-viable
7–8	Viable	Non-viable	Viable	Non-viable

Furthermore, two datasets were tested for each of the models. One dataset was the SNV transformed and the other dataset was first SNV transformed and then first order differentiated. In addition, 10-fold cross-validation was used to validate the models, and the average scores (accuracy, sensitivity and specificity) with standard deviation are reported. The accuracy, sensitivity and specificity scores are defined as:

$$\text{Accuracy} = \frac{\text{TP} + \text{TN}}{\text{TP} + \text{FP} + \text{FN} + \text{TN}}$$

$$\text{Sensitivity} = \frac{\text{TP}}{\text{TP} + \text{FN}} \qquad \text{Specificity} = \frac{\text{TN}}{\text{TN} + \text{FP}}$$

where the model performance depends on True Positives (TP), True Negatives (TN), False Positives (FP) and False Negatives (FN).

During 10-fold cross-validation, for each iteration, data from 9 pigs (9 separate experiments) were used as training data, and data from one pig were used as test data. In this way, we obtained well-validated models where the training data and the test data were fully independent of each other.

PLS-DA is generally well suited for spectroscopic data, where the number of wavelengths is higher than the number of samples and collinearity exists among the variables. During modelling, PLS attempts to find orthogonal linear combinations of latent variables that explain the variability in the spectroscopic data, while being correlated to the response variable. By analyzing the coefficients, we can study the correlations between wavelength and the outcome variable. This allows us to investigate the most important wavelengths to distinguish intestinal tissue with respect to viability. Each input spectrum is given a class number. For the classification of two classes, spectra from viable intestinal tissue were assigned to class "0" and non-viable to class "1". For the classification of three classes, spectra from the control intestinal segment were assigned to class "0", ischemic intestinal segments to class "1" and reperfused segments to class "2". The PLS-DA models were built in Python using the Scikit-learn library.

To find the optimal number of latent variables in the PLS-DA model, a grid search was performed for a range of 2–12 latent variables. For each loop, PLS-DA was run for a certain number of latent variables and obtained an average accuracy score. The optimal number of variables in the model was determined after cross-validation, by evaluating the accuracy score between the true class and the predicted class using the accuracy score from the 10-fold cross-validation. The optimal number of variables was found to be 9, the overall accuracy score started to decrease when a higher number of variables was used.

2.4. Histopathological Examination

To assess the histopathological changes in the tissue, full-thickness biopsies (20 mm × 5 mm) were taken from control, ischemic and reperfused intestinal segments. Specimens from the intestines were fixed overnight in buffered 10% formalin, dehydrated in a graded series of ethanol, and embedded in paraffin. 4-μm-thick sections were cut and then stained with haematoxylin and eosin (H&E). Stained sections were examined by two pathologists simultaneously, and by consensus, each section was classified. The criteria of Swerdlow [22] were used since they are generally accepted and have also been used in previous work by our group [14].

Modified Swerdlow classification of ischemic changes in the small intestinal wall:

- **Grade 0**: No pathological changes;
- **Grade 1**: Focal loss of surface epithelium in the mucosa;
- **Grade 2**: Mucosal infarction, with extensive loss of surface epithelium and areas with substance loss in the mucosal lamina propria. Sparing of basal parts of glands, and of the lamina muscularis mucoae;
- **Grade 3**: Complete mucosal necrosis, variable necrosis of the submucosa, but intact muscularis mucosae;
- **Grade 4**: Complete necrosis of both the mucosa and the submucosa, and loss of the muscularis mucosae;
- **Grade 5**: In addition to the changes of grade 4 there are also circulatory disturbances of the inner part of the external muscular layer (lamina muscularis externa);
- **Grade 6**: Complete necrosis of all layers of the intestinal wall.

When classifying the microscopical findings, it was noted that ischemic changes were not always consistent in each section. Sometimes, the nature and the magnitude of the changes varied from one part of the section to another. In these cases, the section was classified according to the Swerdlow degree that dominated quantitatively in the section. This semi-quantitative approach naturally involved some subjectivity. There were, however, no problems in achieving consensus between the two pathologists.

3. Results

Figure 2 shows the averaged SNV corrected diffuse reflectance spectra for each of the four cases with different intestinal tissue conditions. Clear differences between ischemic and reperfused tissue were observed on the reflectance spectra. The reflectance peak of oxyhemoglobin has a double absorption feature around 546 nm and 578 nm (Figure 2a,c,d), whereas deoxyhemoglobin for the ischemic cases has a single absorption feature around 563 nm (Figure 2b–d). The average reflectance intensity was higher for reperfused intestinal segments compared to ischemic segments in the wavelength range of 600–800 nm; this behaviour was reversed in the wavelength range 800–1000 nm as shown in Figure 2c,d. This observation is consistent with the reported absorption spectra of oxyhemoglobin and deoxyhemoglobin [23,24].

A zoomed-in plot of the diffuse reflectance spectra in the range of 500–600 nm (Figure 3a) makes it easier to observe where the changes related to oxyhemoglobin and deoxyhemoglobin levels occur. To visualize the spectral differences between data from viable and non-viable segments, Figure 3b shows the SNV transformed spectra from all measurement data (10 pigs) divided into two classes; red curves indicate segments histopathologically classified as viable and blue curves indicate segments classified as non-viable.

Figure 4 shows the relative change (relative to the reference Control Case 1) in the first derivative data for Cases 2, 3 and 4. From Figure 4b,c, an inversion of the curves was observed between data from ischemic segments and reperfused segments at several wavelengths. The largest difference between data from ischemia and reperfusion phase occurred in the wavelength range of 500–600 nm, where the difference between oxyhemoglobin and deoxyhemoglobin is most profound. The PLS coefficient (Figure 4d) reveals that the main contributions come from regions in the range of 500–600 nm and 750–800 nm. The PLS
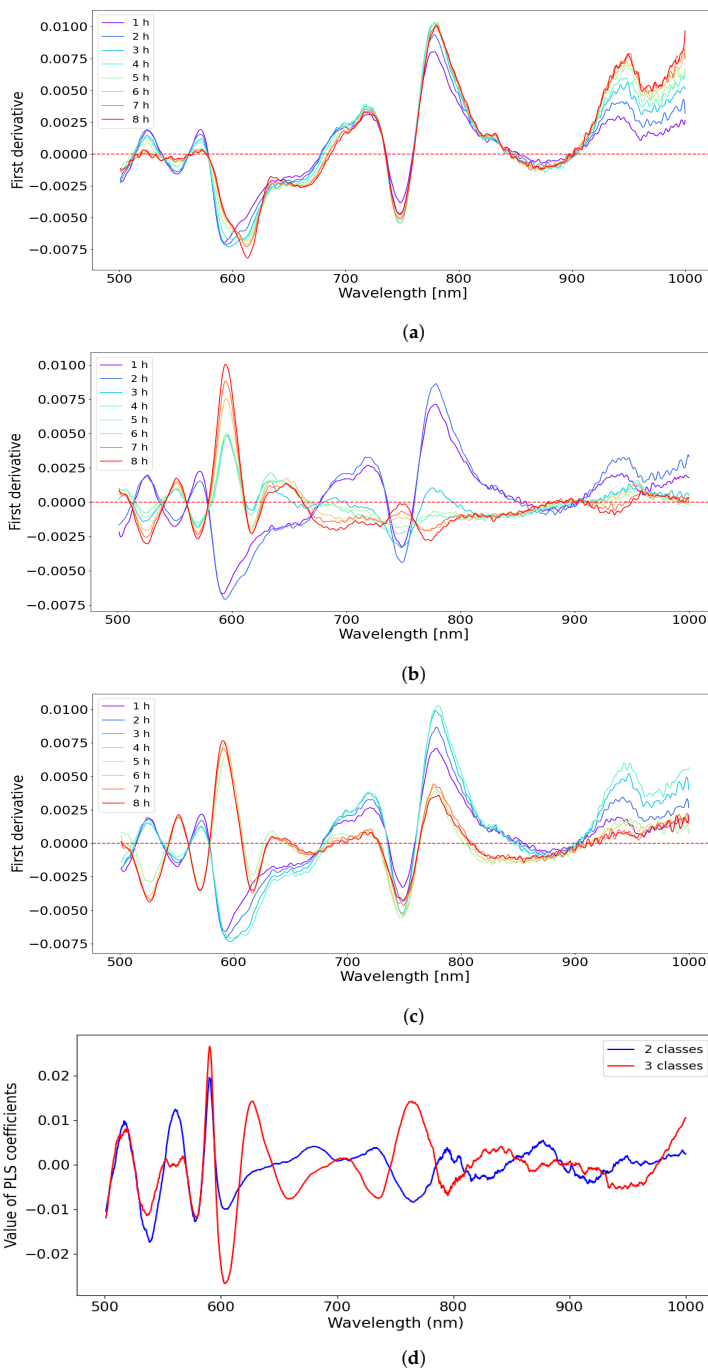
coefficients for the two- and three-class models were similar in the 500–600 nm region, but were less similar for the longer wavelengths.
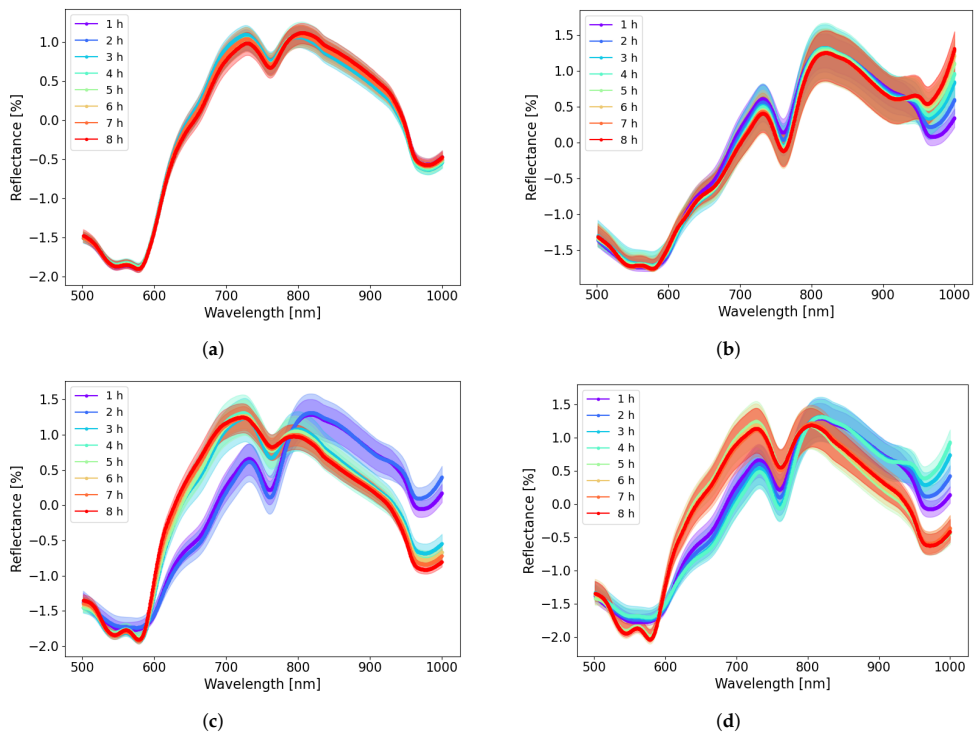
Figure 2. Standard normal variate corrected reflectance spectra for four cases as a function of wavelength using Equation (2). Mean and 95 % confidence intervals are shown in the figures. $N = 10$ for each of the groups. (**a**) Reflectance for Case 1 (Control—8 h of normal perfusion). (**b**) Reflectance for Case 2 (Ischemia—8 h of warm full ischemia). (**c**) Reflectance for Case 3 (2 h of ischemia followed by 6 h of reperfusion). (**d**) Reflectance for Case 4 (4 h of ischemia followed by 4 h of reperfusion).
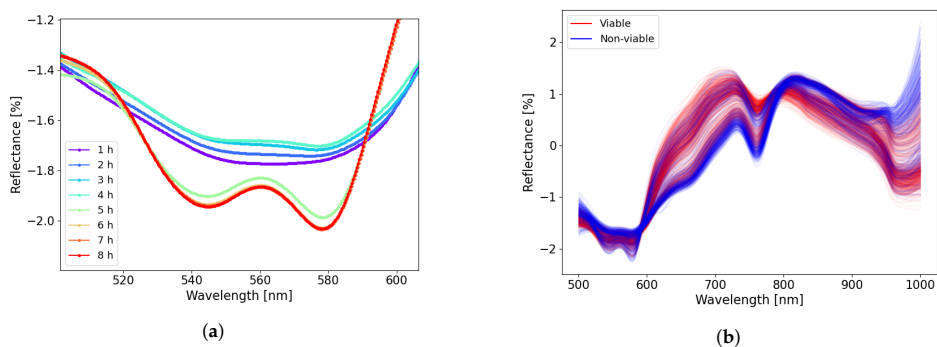
Figure 3. (**a**) A zoomed-in plot in region 500–600 nm of the SNV transformed reflectance data for Case 4 (4 h of ischemia followed by 4 h of reperfusion). (**b**) All acquired spectra separated into viable and non-viable classes.

Figure 4. (**a**–**c**) The difference in the first derivative of reflectance data between Cases 2, 3, 4 and the control Case 1. (**d**) The value of PLS coefficients as a function of wavelength for both two- and three-class models.

Table 2a,b show the results from three- and two-class classification with PLS-DA models, respectively. Average scores (accuracy, sensitivity and specificity) with standard deviation from 10-fold cross-validation are reported.

Table 2. Classification results of 10-fold cross-validation using PLS-DA with mean and standard deviation. Two different datasets were used, one dataset was SNV transformed, and the other dataset was SNV transformed and first-order differentiated. (**a**) Three-class classification between control, ischemic and reperfused intestinal segments. (**b**) Two-class classification between viable and non-viable intestinal segments.

a. Three-class model classification results			
Control VS ischemia VS Reperfusion			
Data	Accuracy [%]	Sensitivity [%]	Specificity [%]
SNV	97.8 ± 1.3	99.1 ± 1.3	97.8 ± 3.1
SNV Deri	99.2 ± 0.9	99.5 ± 0.8	98.9 ± 1.9
b. Two-class model classification results			
Viable VS Non-viable			
Data	Accuracy [%]	Sensitivity [%]	Specificity [%]
SNV	92.5 ± 2.9	87.8 ± 11.3	95.3 ± 4.4
SNV Deri	96.0 ± 2.8	94.2 ± 6.5	97.2 ± 2.6

The PLS-DA model was more accurate when classifying control, ischemic and reperfused intestinal segments, than when classifying viable and non-viable segments. Average accuracies of 97.8% and 92.5% respectively were achieved when using the SNV transformed data for three- and two-class classification models, respectively. The accuracies were higher when the first derivative data was used, for both two- and three-class classification.

To further test how accurately the PLS-DA model performs when there is extensive overlap of the spectra, two additional models were created to classify viable versus non-viable for data from the ischemia and reperfusion phases, respectively. The challenge is that spectra within the ischemia phase can be similar to each other and that the same is true for spectra within the reperfusion phase. Average accuracies of 82.5% and 82.8% were achieved when classifying viable versus non-viable, using the SNV transformed dataset and the first-order differentiated dataset from the ischemia phase. Average accuracies of 97.0% and 99.3% were achieved in the classification of viable versus non-viable, using the SNV transformed dataset and the first order differentiated dataset from the reperfusion phase.

Histopathology

The microscopical investigations revealed that, with an increasing duration of ischemia, the damage to the wall of the small intestine was progressively higher. The morphological changes started in the mucosa, first with damage and loss of the surface epithelium and thereafter with increasing loss of both epithelium and connective tissue stroma. After 2 h of ischemia, many basal parts of mucosal glands were still intact, and the intestine wall was judged to be still viable at this stage (Figure 5b). After 3 h or more of ischemia, the damage to the mucosa was extensive, and at these stages the intestine was considered to be non-viable (Figure 6a,b). After 4 h of ischemia, there were large areas with complete mucosal and submucosal necrosis (Figure 6b).

(**a**)　　　　　　　　　　　　　　　　　　　(**b**)
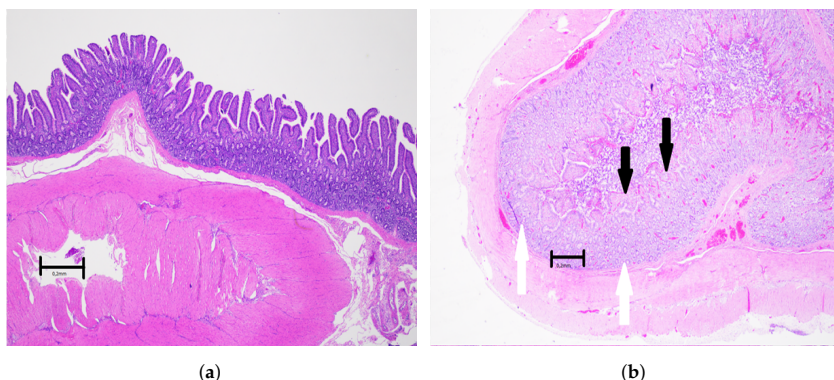
Figure 5. Light microscopical pictures of selected structures of the viable small intestine. Objective magnification ×2. Scale bar indicates 0.2 mm. (**a**) Light microscopical picture of the wall of the healthy control small intestine, with no injury, photographed before the start of ischemia. All layers of the intestinal wall are intact and without pathological changes, i.e., modified Swerdlow grade 0. (**b**) Light microscopical picture of the wall of the small intestine after 2 h of ischemia followed by 2 h of reperfusion. There is extensive damage to the surface epithelium of the mucosa (black arrows) and areas of substance loss in the mucosal lamina propria. The lamina muscularis mucosae is preserved, and some basal parts of glands are intact (white arrows), classified as modified Swerdlow grade 2.

(**a**)　　　　　　　　　　　　　　　　　　　(**b**)
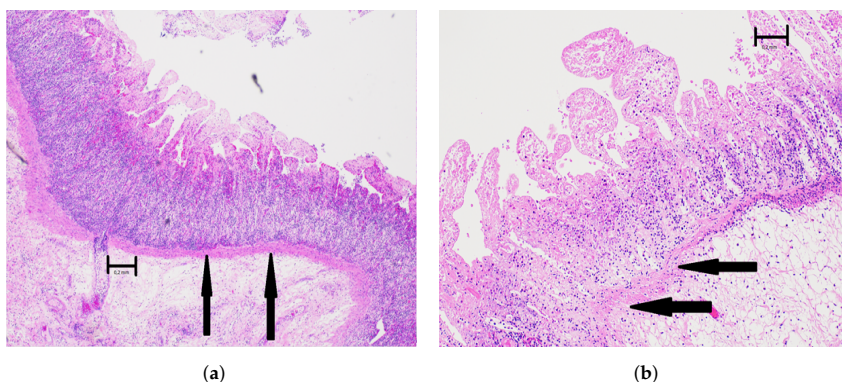
Figure 6. Light microscopical picture of selected structures of the non-viable small intestine. Objective magnification ×2. Scale bar indicates 0.2 mm. (**a**) A light microscopical picture of the small intestine after 3 h of ischemia and 5 h of reperfusion. There is complete mucosal necrosis with loss of villus epithelium, and basal parts of the glands are not preserved. There is also edema and other circulatory disturbances of the submucosa. The lamina muscularis mucosa is intact (black arrows), classified as modified Swerdlow grade 3. (**b**) The light microscopical picture of the small intestinal wall after 4 h of ischemia followed by 4 h of reperfusion. There is complete necrosis of the mucosa with no remaining viable epithelium. The submucosa shows complete necrosis with edema and dilated vessels. The lamina muscularis mucosae is fragmented and destroyed to about one-third of its length in this picture (black arrows), classified as modified Swerdlow grade 4.

4. Discussion

Diffusely reflected light contains information about the chemical composition of the sample (absorption) and the microstructure (scattering). For biological samples, the scattering properties are excessively complex [21], making it challenging to interpret the simultaneously occurring variations in the acquired spectra. In this study, important

differences were observed in the spectra in the wavelength regions where oxyhemoglobin and deoxyhemoglobin influence absorption. The full spectral wavelength range was used to classify whether small intestinal segments were viable or non-viable, to investigate the accuracy and estimate clinical relevance.

VIS-NIR spectrometry can be compared to the bioimpedance method, where, instead of illuminating with and detecting light across a range of wavelengths, an electrical signal is applied across a range of frequencies, and the passive electrical properties of the tissue are measured. Low-frequency electrical bioimpedance (Hz and kHz range) mainly reflects the cellular structure [25], while bioimpedance in the MHz and GHz range depends more on the dipolar nature of biomolecules [3,26]. However, optical spectroscopy has an advantage over bioimpedance, in that measurements can be non-contact (for instance interactance measurements [27]). Non-contact bioimpedance measurements based on the induction of Eddy currents have been reported [28]. However, in most practical bioimpedance setups, a direct application of two or four electrodes is required [29].

A typical pulse oximeter uses two small light-emitting diodes, red (660 nm) and infrared (940 nm), to measure a photoplethysmography signal. This signal contains AC and DC components and is based on changes in reflectance due to pulses of arterial blood in the tissue. These components are used to calculate the oxygen saturation of the tissue. This method gives relative measurements as it uses the ratio between AC_{660nm}/DC_{660nm} and AC_{940nm}/DC_{940nm}. However, ischemic intestine or recently reperfused intestinal tissue often has no pulse or a very weak pulse. This is a condition where a typical pulse oximeter will not measure any AC component and thus cannot give any estimation of oxygen saturation in the tissue. Diffuse reflectance spectrometry does not depend on a detectable pulse but provides a distinct reflectance curve over the measured wavelengths. This enables us to study the condition of the small intestine even when the arterial pulse is absent during ischemia. The VIS-NIR spectrum includes specific wavelengths that contain information about oxygen saturation and wavelengths that contain complex information about other chemical compositions and tissue microstructure.

In VIS-NIR spectroscopy, it is often hard to predict in advance which wavelength bands contain the most information relative to the analyte to be measured. Measuring the full wavelength range during a study enables the selection of the most relevant bands associated with ischemia–reperfusion injury.

There is a clear distinction between the control, ischemia, and reperfusion cases in Figure 2. For the control case (Figure 2a), variations during the 8-hour experiment are minor, indicating that there are minor changes in reflectance in the control segment, which is expected. For the ischemic and the reperfusion cases (Figure 2b–d), the differences compared to the control segments increase with ischemic time. Changes in the reflectance spectra during the ischemia and reperfusion period are not as obvious from one hour to another. There is a larger variation at 6, 7, and 8 h for Cases 2 and 4 (Figure 2b,d).

When ischemia is followed by reperfusion, the concentrations of oxyhemoglobin and deoxyhemoglobin change drastically. Figure 3a shows how the reflectance spectra in the wavelength range 500–600 nm switch from the ischemic to the reperfused state in Case 4 (4 h of ischemia followed by 4 h of reperfusion). The 500–600 nm region is dominated by differences between oxyhemoglobin and deoxyhemoglobin, which is a prominent feature related to ischemia–reperfusion injury. During ischemia, the level of deoxyhemoglobin increases as the tissue does not receive enough oxygenated blood, until the oxygen is entirely depleted. During reperfusion, there is an increase in oxyhemoglobin, as the tissue is perfused with oxygenated blood. This reflectance curve shape is consistent with the results reported by Karakas et al. [5], where similar spectral changes were observed for ischemic and perfused/reperfused intestinal segments (They plotted absorption instead of reflection in their figures).

Karakas et al. [5] conducted an experiment that was similar to ours, but focused on the ratio of the absorption between wavelengths at 560 nm and at 577 nm. We were not able to reproduce the associations between the ratio value to the histopathological grading as they

133

pointed out in their study. The reason may be that we have used a different animal model and that the field of view of the optical fiber probe used in their study was considerably smaller than the probe used in this study. Sowa et al. [1] built a PLS-DA model on the spectroscopic data from the control and the ischemic segment and tested the model on data from reperfused segments. An average accuracy of 89% and sensitivity and specificity of over 80% were achieved in detecting ischemic tissue, but they did not classify viability.

The immunological responses during ischemia–reperfusion can increase the luminal epithelial permeability. After revascularization, increased vascular permeability will typically result in the formation of edema in the intestinal layers, especially the submucosa [30–32]. This can result in both chemical and microstructural changes that might explain some of the differences observed across the wavelength range.

When comparing the relative change between the first derivative of the intervention cases and the first derivative of the reference control case (Figure 4a–c), a partial inversion of the trace curve is observed. The trace curve crosses the zero line several times at different wavelengths, dependent on whether the case is ischemia or reperfusion. This reveals clear distinctions in the reflectance of VIS-NIR between the different cases. At local minima or maxima in the reflectance spectra, the first derivative curve crosses the zero line (on the y-axis). Whenever the spectra of the first derivative of the intervention groups (Cases 2, 3 and 4) overlap with the spectra of the first derivative of the reference case, the spectra in Figure 4a–c would cross the zero-line (on y-axis). As the control is the zero line in the plots, the magnitude of the deviation from the zero-line shows the wavelength dependent differences between the cases clearer than when plotting the raw data.

The PLS coefficients (Figure 4d) were quite similar for the two- and three-class models, with some differences around 760 nm, one of the oxyhemoglobin's absorption maxima. This can indicate that the wavelength region 500–600 nm is equally important for both classification tasks. The regression coefficients in the region 750–800 nm were positively correlated with the shorter wavelength weights for the 3-class model and negatively correlated with the shorter wavelength weights for the 2-class model. This seems to follow the general shape of the oxyhemoglobin and deoxyhemoglobin absorption curve. In general, the regression vector places emphasis on the regions where the absorption maxima for both oxyhemoglobin and deoxyhemoglobin are present.

From the PLS coefficients (Figure 4d), we obtain an indication of the critical wavelengths for classifying viable and non-viable intestinal segments, and between the segments in the control, ischemia and reperfusion phases. This can help us to understand the potential for making a specialised instrument for this application. The wavelength region of 500–600 nm appears to be the most important for the models, and it may be sufficient to focus on these when designing a specialised instrument. Two models were built using only data from 500–600 nm; for two-class classification, mean accuracies of 94.0% and 92.0% were achieved with SNV transformed data and first-order differentiated data, respectively. For three-class classification, mean accuracies of 96.6% and 96.5% were achieved with SNV transformed data and first-order differentiated data. However, it is not conclusive whether including or excluding the region above 700 nm could make the model more or less robust; this would require a larger dataset.

It can be challenging to assess the blood flow condition in intestinal tissue based on visual inspection alone, as small differences in color can be difficult for the human eye to perceive. With reflectance spectroscopy and PLS-DA, it was possible to distinguish intestinal tissues with different injury conditions more accurately than the standard clinical method, where the success rate for identifying the non-viable segments during the first laparotomy is reportedly around 50% [30,33].

Regarding the generalizability of the classification models, 10-fold cross-validation was used, where each fold contained spectral data from one pig. During cross-validation, data from 9 pigs were used for training, and data from one pig were used for testing, ensuring that data from the same pig did not appear in both the training and test datasets. In this way, more generalized models were obtained, and data leakage was avoided, resulting

in a more reliable model. It is unknown how transferable these results obtained from pig intestine are with respect to the human intestine, as diffuse reflectance spectroscopy on the human intestine has yet to be investigated in a similar setting. However, the pig intestine has important physiological and anatomical similarities to humans [34], and the mechanisms of ischemia–reperfusion injury are similar to the mechanisms observed in the human intestine [35]. Therefore, utilizing pig models to investigate ischemia–reperfusion injury can provide important insights and knowledge which may be transferable to the assessment of intestinal viability in humans.

The borderline between viable and non-viable intestine tissue was investigated by histopathological analysis. Earlier studies indicated that the possible upper limit for viability in the porcine mesenteric occlusion model is ≤3 h ischemic time [14]. In this study, the upper limit for viability seems to be ≤2 h of ischemic time.

The limited size of the biopsy sample and the heterogeneous composition of the lesions makes it challenging to evaluate the small intestine viability based on histological assessment [36,37]. Different injury degrees can be found within the same intestinal sample, and it is difficult to know whether changes seen in small samples are representative of the entire intestine. It is also difficult to speculate about how much remaining epithelium and muscle tissue is necessary for the intestine to be viable and functional.

The 'point of no return' is hard to define and the time window for successful intervention is much harder to assess for small intestines when compared to the brain, heart, or kidney [30]. Current clinical preoperative assessment of intestinal viability after reperfusion can be challenging and, in many cases, a second look surgery after 24–72 h is required. During this period, the patient is at a high risk of acquiring intra-abdominal infections and sepsis. In severe cases, multi-organ failure and death occur. This further highlights the need for the development of decision support technologies that can assist the surgeon to resect only intestines that will not survive after reperfusion. Objective and accurate decision tools can help prevent short bowel syndrome, reduce the need for second-look surgery and ensure that locations selected for anastomosis are viable. This will improve the prognosis of the patients significantly.

The model used in this study only investigates diffuse reflectance spectroscopy during warm segmental full ischemia and does not investigate how intestinal tissue reflectance will change during other pathological developments. Mechanisms such as arterial/venous thrombosis and superior mesenteric artery occlusion may result in different spectral variations and signatures.

An ideal method to predict bowel viability after intestinal ischemia–reperfusion injury would offer the following features: high safety and easy handling, high accuracy, objectivity, reproducibility, and cost efficiency [38]. Spectroscopy measurements have the advantage of quick acquisition time, acquiring a spectrum from intestinal tissue takes <2 s. The DR probe used covers 24 mm × 47 mm of the small intestinal surface and allows the surgeon to scan areas of interest in a short time. As this method measures reflected light from the measurement site, it is not very dependent on the thickness of the tissue, unless the tissue becomes transparent. As the technique only applies light to the object being measured without applying any active signal that might pose a risk to the patient, and it does not require direct contact with the tissue (there is a requirement for isolation from ambient room light, which might require tissue contact), the measurement can easily be performed in a sterile environment. This allows for simplification of the clinical approval process for medical devices. The sum of these advantages makes this method potentially very user-friendly and efficient for real-time intraoperative assessment of the injury level of ischemic intestinal tissues. In the future, we are planning to test the interactance measurement, which allows for better optical sampling in the depth direction. A probe could be mounted over the tissue, non-contact, and monitor the relative change throughout the surgery.

This study used ten pigs, with four cases of ischemia–reperfusion models in each pig, with hourly measurements on each case over a period of 8 h. To further investigate this method, it would be necessary to assess other common intestinal ischemia–reperfusion

135

pathological scenarios and to test on human intestines. To be able to assess this approach on human patients, different sterilization methods are currently being evaluated, for instance using hydrogen peroxide on the DR probe itself and using a sterile camera drape around the communication wire.

5. Conclusions

Using diffuse reflectance spectroscopy together with supervised partial least squares-discriminant analysis, it was possible to distinguish between normal, ischemic, and reperfused segments with an average accuracy of 99.2%. Furthermore, viable and non-viable segments were successfully classified with an average accuracy of 96.0%, which suggests that this approach has the potential to detect and assess the degree of ischemia–reperfusion injury non-invasively. Given that the measurement time required is around one to two seconds, this method can potentially be used to make real-time predictions and aid the decision-making process when estimating suitable margins for bowel resection during surgery. Histological analysis showed that the porcine intestinal segments are probably not viable after three hours of full ischemic occlusion. The initial results are very promising. Going forward, the method needs further refinement and validation in a larger study population and clinical validation on human patients with intestinal ischemia.

References

1. Sowa, M.G.; Kohlenberg, E.; Payette, J.R.; Leonardi, L.; Levasseur, M.A.; Riley, C.B. Detecting Intestinal Ischemia Using near Infrared Spectroscopy. *J. Near Infrared Spectrosc.* **2006**, *14*, 1–7. [CrossRef]
2. Strand-Amundsen, R.J.; Reims, H.M.; Tronstad, C.; Kalvøy, H.; Martinsen, Ø.G.; Høgetveit, J.O.; Ruud, T.E.; Tønnessen, T.I. Ischemic small intestine—in vivoversusex vivobioimpedance measurements. *Physiol. Meas.* **2017**, *38*, 715–728. [CrossRef]
3. Hou, J.; Strand-Amundsen, R.; Tronstad, C.; Tønnessen, T.I.; Høgetveit, J.O.; Martinsen, Ø.G. Small intestinal viability assessment using dielectric relaxation spectroscopy and deep learning. *Sci. Rep.* **2022**, *12*, 3279. [CrossRef]
4. Watanabe, T.; Shimizu, T.; Mori, M.; Yamamoto, Y.; Tei, E.; Hirakawa, H. Predicting viability of ischemic small bowel using intraoperative indocyanine green fluorescence angiography. *J. Pediatr. Surg. Case Rep.* **2022**, *79*, 102218. [CrossRef]
5. Karakaş, B.R.; Sırcan-Küçüksayan, A.; Elpek, O.E.; Canpolat, M. Investigating viability of intestine using spectroscopy: A pilot study. *J. Surg. Res.* **2014**, *191*, 91–98. [CrossRef] [PubMed]
6. Bulkley, G.B.; Zuidema, G.D.; Hamilton, S.R.; O'Mara, C.S.; Klacsmann, P.G.; Horn, S.D. Intraoperative determination of small intestinal viability following ischemic injury: A prospective, controlled trial of two adjuvant methods (Doppler and fluorescein) compared with standard clinical judgment. *Ann. Surg.* **1981**, *193*, 628–637. [CrossRef] [PubMed]

7. Bryski, M.G.; Sulyok, L.G.F.; Kaplan, L.; Singhal, S.; Keating, J.J. Techniques for intraoperative evaluation of bowel viability in mesenteric ischemia: A review. *Am. J. Surg.* **2020**, *220*, 309–315. [CrossRef]

8. Seike, K.; Koda, K.; Saito, N.; Oda, K.; Kosugi, C.; Shimizu, K.; Miyazaki, M. Laser Doppler assessment of the influence of division at the root of the inferior mesenteric artery on anastomotic blood flow in rectosigmoid cancer surgery. *Int. J. Color. Dis.* **2007**, *22*, 689–697. [CrossRef]

9. Singh, D.B.; Stansby, G.; Harrison, D.K. Assessment of oxygenation and perfusion in the tongue and oral mucosa by visible spectrophotometry and laser Doppler flowmetry in healthy subjects. *Adv. Exp. Med. Biol.* **2008**, *614*, 227–233. [CrossRef]

10. Singh, D.B.; Stansby, G.; Bain, I.; Harrison, D.K. Intraoperative measurement of colonic oxygenation during bowel resection. *Adv. Exp. Med. Biol.* **2009**, *645*, 261–266. [CrossRef]

11. Urbanavičius, L.; Pattyn, P.; Van de Putte, D.; Venskutonis, D. How to assess intestinal viability during surgery: A review of techniques. *World J. Gastrointest. Surg.* **2011**, *3*, 59–69. [CrossRef] [PubMed]

12. Dyess, D.L.; Bruner, B.W.; Donnell, C.A.; Ferrara, J.J.; Powell, R.W. Intraoperative evaluation of intestinal ischemia: A comparison of methods. *South. Med. J.* **1991**, *84*, 966–969. 974. [CrossRef]

13. Deeba, S.; Corcoles, E.P.; Hanna, G.B.; Hanna, B.G.; Pareskevas, P.; Aziz, O.; Boutelle, M.G.; Darzi, A. Use of rapid sampling microdialysis for intraoperative monitoring of bowel ischemia. *Dis. Colon Rectum* **2008**, *51*, 1408–1413. [CrossRef] [PubMed]

14. Strand-Amundsen, R.J.; Reims, H.M.; Reinholt, F.P.; Ruud, T.E.; Yang, R.; Høgetveit, J.O.; Tønnessen, T.I. Ischemia/reperfusion injury in porcine intestine—Viability assessment. *World J. Gastroenterol.* **2018**, *24*, 2009–2023. [CrossRef]

15. Strand-Amundsen, R.J.; Tronstad, C.; Reims, H.M.; Reinholt, F.P.; Høgetveit, J.O.; Tønnessen, T.I. Machine learning for intraoperative prediction of viability in ischemic small intestine. *Physiol. Meas.* **2018**, *39*, 105011. [CrossRef] [PubMed]

16. Hou, J.; Strand-Amundsen, R.; Hødnebø, S.; Tønnessen, T.I.; Høgetveit, J.O. Assessing ischemic injury in human intestine ex vivo with electrical impedance spectroscopy. *J. Electr. Bioimpedance* **2021**, *12*, 82–88. [CrossRef]

17. Kohlenberg, E.; Payette, J.R.; Sowa, M.G.; Levasseur, M.A.; Riley, C.B.; Leonardi, L. Determining intestinal viability by near infrared spectroscopy: A veterinary application. *Vib. Spectrosc.* **2005**, *38*, 223–228. [CrossRef]

18. Gay, A.N.; Lazar, D.A.; Stoll, B.; Naik-Mathuria, B.; Mushin, O.P.; Rodriguez, M.A.; Burrin, D.; Olutoye, O. Near-Infrared Spectroscopy Measurement of Abdominal Tissue Oxygenation is a Useful Indicator of Intestinal Blood Flow and Necrotizing Enterocolitis in Premature Piglets. *J. Pediatr. Surg.* **2011**, *46*, 1034–1040. [CrossRef]

19. Strand-Amundsen, R.J.; Tronstad, C.; Kalvøy, H.; Gundersen, Y.; Krohn, C.D.; Aasen, A.O.; Holhjem, L.; Reims, H.M.; Martinsen, Ø.G.; Høgetveit, J.O.; et al. In vivocharacterization of ischemic small intestine using bioimpedance measurements. *Physiol. Meas.* **2016**, *37*, 257–275. [CrossRef]

20. Weingarten, M.S.; Papazoglou, E.S.; Zubkov, L.; Zhu, L.; Neidrauer, M.; Savir, G.; Peace, K.; Newby, J.G.; Pourrezaei, K. Correlation of near infrared absorption and diffuse reflectance spectroscopy scattering with tissue neovascularization and collagen concentration in a diabetic rat wound healing model. *Wound Repair Regen.* **2008**, *16*, 234–242. [CrossRef]

21. Rinnan, Å.; Berg, F.v.d.; Engelsen, S.B. Review of the most common pre-processing techniques for near-infrared spectra. *TrAC Trends Anal. Chem.* **2009**, *28*, 1201–1222. [CrossRef]

22. Swerdlow, S.H.; Antonioli, D.A.; Goldman, H. Intestinal infarction: A new classification. *Arch. Pathol. Lab. Med.* **1981**, *105*, 218. [PubMed]

23. Lingqin, K.; Zhao, Y.; Dong, L.; Jian, Y.; Jin, X.; Li, B.; Feng, Y.; Liu, M.; Liu, X.; Wu, H. Non-contact detection of oxygen saturation based on visible light imaging device using ambient light. *Opt. Express* **2013**, *21*, 17464–17471. [CrossRef]

24. Mordant, D.J.; Al-Abboud, I.; Muyo, G.; Gorman, A.; Sallam, A.; Ritchie, P.; Harvey, A.R.; McNaught, A.I. Spectral imaging of the retina. *Eye* **2011**, *25*, 309–320. [CrossRef]

25. Martinsen, Ø.G.; Grimnes, S.; Mirtaheri, P. Non-invasive measurements of post-mortem changes in dielectric properties of haddock muscle—A pilot study. *J. Food Eng.* **2000**, *43*, 189–192. [CrossRef]

26. Hou, J.; Liavåg, O.M.I.; Færden, I.H.; Martinsen, Ø.G.; Tønnessen, T.I.; Line, P.D.; Hagness, M.; Høgetveit, J.O.; Pischke, S.E.; Strand-Amundsen, R. Utilization of dielectric properties for assessment of liver ischemia–reperfusion injury in vivo and during machine perfusion. *Sci. Rep.* **2022**, *12*, 11183. [CrossRef]

27. O'Farrell, M.; Tschudi, J.; Schulerud, H.; Wold, J.P.; Ottestad, S.; Høy, M. Online NIR Multispectral Imaging using Non-Contact Interactance for Fish and Meat Quality Measurements. In Proceedings of the Imaging and Applied Optics Congress (2010), Tucson, AZ, USA, 7–8 June 2010; Optica Publishing Group: Washington, DC, USA, 2010; p. ATuA3. [CrossRef]

28. Gürsoy, D.; Scharfetter, H. Magnetic induction pneumography: A planar coil system for continuous monitoring of lung function via contactless measurements. *J. Electr. Bioimpedance* **2010**, *1*, 56–62. [CrossRef]

29. Grimnes, S.; Martinsen, Ø.G. Sources of error in tetrapolar impedance measurements on biomaterials and other ionic conductors. *J. Phys. Appl. Phys.* **2006**, *40*, 9. [CrossRef]

30. Kalogeris, T.; Baines, C.P.; Krenz, M.; Korthuis, R.J. Cell Biology of Ischemia/Reperfusion Injury. *Int. Rev. Cell Mol. Biol.* **2012**, *298*, 229–317. [CrossRef]

31. Carden, D.L.; Granger, D.N. Pathophysiology of ischaemia-reperfusion injury. *J. Pathol.* **2000**, *190*, 255–266. [CrossRef]

32. Cowled, P.; Fitridge, R. Pathophysiology of Reperfusion Injury. In *Mechanisms of Vascular Disease: A Reference Book for Vascular Specialists*; Fitridge, R., Thompson, M., Eds.; University of Adelaide Press: Adelaide, Australia, 2011.

33. Redaelli, C.A.; Schilling, M.K.; Büchler, M.W. Intraoperative Laser Doppler Flowmetry: A Predictor of Ischemic Injury in Acute Mesenteric Infarction. *Dig. Surg.* **1998**, *15*, 55–59. [CrossRef] [PubMed]

34. Douglas, W.R. Of pigs and men and research. *Space Life Sci.* **1972**, *3*, 226–234. [CrossRef] [PubMed]
35. Yandza, T.; Tauc, M.; Saint-Paul, M.C.; Ouaissi, M.; Gugenheim, J.; Hébuterne, X. The pig as a preclinical model for intestinal ischemia–reperfusion and transplantation studies. *J. Surg. Res.* **2012**, *178*, 807–819. [CrossRef] [PubMed]
36. Hillman, H. Limitations of clinical and biological histology. *Med. Hypotheses* **2000**, *54*, 553–564. [CrossRef]
37. Dabareiner, R.M.; Sullins, K.E.; White, N.A.; Snyder, J.R. Serosal injury in the equine jejunum and ascending colon after ischemia–reperfusion or intraluminal distention and decompression. *Vet. Surg. VS* **2001**, *30*, 114–125. [CrossRef]
38. Horgan, P.G.; Gorey, T.F. Operative Assessment of Intestinal Viability. *Surg. Clin. N. Am.* **1992**, *72*, 143–155. [CrossRef]

138